REPORT DOCUMENTATION PAGE

Form Approved
OMB No. 0704-0188

1. REPORT DATE (DD-MM-YYYY)	2. REPORT TYPE	3. DATES COVERED (From – To)
	Final Technical Report	1 August 2003 – 31 May 2007

4. TITLE AND SUBTITLE
Combinatorial Production and Processing of Oxide Nanopowders for Transparent, Ceramic Lasers

5a. CONTRACT NUMBER

5b. GRANT NUMBER
F49620-03-1-0389

5c. PROGRAM ELEMENT NUMBER

6. AUTHOR(S)
Dr. Richard M. Laine
Dr. Stephen C. Rand

5d. PROJECT NUMBER

5e. TASK NUMBER

5f. WORK UNIT NUMBER

7. PERFORMING ORGANIZATION NAME(S) AND ADDRESS(ES)
Department of Materials Science and Engineering
University of Michigan

8. PERFORMING ORGANIZATION REPORT NUMBER

9. SPONSORING/MONITORING AGENCY NAME(S) AND ADDRESS(ES)
USAF/AFRL
AFOSR
875 North Randolph Street
Arlington VA 22203
Dr Joan Fuller/NA

10. SPONSOR/MONITOR'S ACRONYM(S)
AFOSR

11. SPONSORING/MONITORING AGENCY REPORT NUMBER
N/A

12. DISTRIBUTION AVAILABILITY STATEMENT

Distribution Statement A: Approved for public release.

AFRL-SR-AR-TR-08-0006

13. SUPPLEMENTARY NOTES

14. ABSTRACT

Since the discovery of transparent polycrystalline alumina by Coble in 1962,[1] transparent and translucent alumina and yttria based ceramics have achieved a significant presence in our everyday lives because of their utility in sodium (and metal halide) vapor lamp envelopes used for example in street lights (automotive lighting).[2-6] More recently, transparent ceramic scintillators have replaced photographic film in most medical X-ray imaging equipment.[7] Although known for 30 years,[8,9] transparent ceramic lasers have only recently been shown to offer power outputs superior to single crystal lasers.[10-16]

15. SUBJECT TERMS

16. SECURITY CLASSIFICATION OF:			17. LIMITATION OF ABSTRACT	18. NUMBER OF PAGES	19a. NAME OF RESPONSIBLE PERSON
a. REPORT	b. ABSTRACT	c. THIS PAGE			19b. TELEPONE NUMBER (*Include area code*)
Unclassified	Unclassified	Unclassified	Unclassified		(703)

Combinatorial Production and Processing of Oxide Nanopowders for Transparent, Ceramic Lasers

AFOSR GRANT NUMBER F49620-03-1-0389

Richard M. Laine
Department of Materials Science and Engineering
University of Michigan
Stephen C. Rand
Division of Applied Physics, Randall Laboratory
University of Michigan

Final Report for the period June, 2003 to June 2007

Prepared for:

Dr. Joan Fuller

]Ceramic and Non-Metallic Materials Program Manager
Air Force Office of Scientific Research
801 N. Randolph Street, Room 732
Arlington, VA 22203-1977
phone: (703) 696-7236
fax: (703) 696-8451

Introduction

Since the discovery of transparent polycrystalline alumina by Coble in 1962,[1] transparent and translucent alumina and yttria based ceramics have achieved a significant presence in our everyday lives because of their utility in sodium (and metal halide) vapor lamp envelopes used for example in street lights (automotive lighting).[2-6] More recently, transparent ceramic scintillators have replaced photographic film in most medical X-ray imaging equipment.[7] Although known for 30 years,[8,9] transparent ceramic lasers have only recently been shown to offer power outputs superior to single crystal lasers.[10-16] Transparent ceramic lasers offer exceptional potential for applications ranging from industrial cutting/welding, to fusion drivers because they offer: (1) higher energy production than single crystal lasers; (2) access to very large sizes and arbitrarily shaped gain media; (3) access to new phases of conventional laser media with phases and compositions normally inaccessible via melt grown, single crystal technology, (4) novel ion-host dopant combinations achievable through fast-quenching pyrolysis, and (5) lower manufacturing costs than melt grown crystals.[10-16] Unfortunately, all of this promise comes from Japanese studies.[10-16] Limited work is currently being done in the U.S., despite the original discovery of transparent ceramic lasers by GE researchers.[8,9]

Translucent alumina used in envelopes has a 40-year history and represents a relatively mature technology from a ceramics science and engineering perspective. Much of what is known about transparency in ceramics has been developed through study of envelope materials, driven by the need for better lighting, and by sales of tens of thousands of sodium vapor lamps. In contrast, transparent ceramics for laser applications represent a completely new technology, with most of the progress occurring only in the last 10^+ years.[10-16]

Given that transparent, polycrystalline ceramics offer much higher strengths, better thermal stability and corrosion resistance than glasses; one might expect more widespread application of these materials. However extensive materials and processing costs, except for envelopes ($1/ea),[2d] still limit their utility. Efforts to optimize envelope performance have identified purity, porosity, densification and grain size[17] issues that must be surmounted to realize superior products, as discussed below.[2-6]

In general, most processing costs come from the need to sinter at high temperatures, frequently under pressure and in special atmospheres or under vacuum. The need for high purity materials and numerous processing steps requiring excellent control of phase purity has limited general investigation into processing transparent ceramics. Even now, after years of refinement, Ueda et al. and Ikesue et al use multiple steps to produce YAG composition powders that can be sintered to acceptable laser materials, Figure **1**.[13,14,16]

Clearly, the utility of transparent ceramics would be greatly expanded if the above processing issues could be minimized. Likewise, if the number of materials that could be sintered to transparency were expanded, more applications would result. Several general applications areas, including those of considerable interest to DoD and the Air Force in particular are listed in the research objectives section.

The key to minimizing processing difficulties lies in developing low-cost methods of producing high quality, mixed-metal oxide nanopowders. This is because oxide nanopowders can be sintered to full density at much lower processing temperatures than micron sized powders,[18] thus reducing the time and expense of processing transparent ceramics. Nanopowders also offer potential access to fully dense, transparent materials with < 500 nm grain sizes thereby realizing both high strength but with transparency identical to large grain size materials.[17] Furthermore, under some conditions, they can even be pressed to transparency with little or no heating.[18-20]

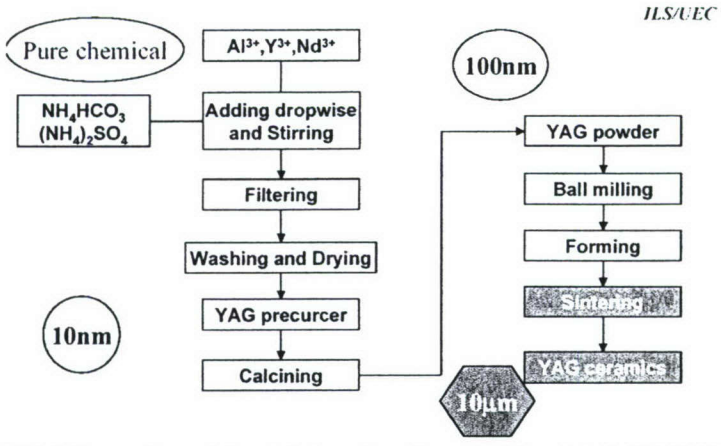

Figure 1. K-I. Ueda, "High Power Laser Materials based on Ceramic Materials," CLEO 2002, Long Beach, CA

Thus, the true obstacle is in developing a general method of making high quality, mixed-metal oxide nanopowders.

Liquid-feed flame spray pyrolysis (LF-FSP) is a process developed at the University of Michigan (UM) that provides high purity, mixed-metal oxide nanopowders in only two steps. The process combusts oxygen-generated aerosol mists of alcohol solutions of high purity metal-loorganic precursors. Rapid quenching follows combustion to produce ceramic oxide "soot" or nanopowders at 100-300 g/h with the exact inorganic composition of the original solution.[21-26] The resulting particles are (in general) easily dispersed, unnecked, unaggregated single crystals with average particle sizes < 30 nm. As we demonstrate below, these materials press well and sinter easily to full density without few processing aids. They also provide access to fine grained transparent photonic materials. Thus, they offer excellent potential for producing the highest quality transparent ceramics, especially high power laser materials, more readily than any other method.

What is most important about LF-FSP is that because the compositions of the solutions can be changed at will, potentially even during mixing just before aerosolization, it becomes possible to combinatorially produce mixed-metal oxide materials. Hence it becomes possible to rapidly optimize materials for given properties or for ease of processing. Furthermore, it is possible to create "cocktail" compositions that access completely new materials that exhibit unexpected laser physics.[24-26]

Given the potential that transparent ceramic materials offer generally, and that ceramic lasers offer more specifically, to the Air Force, DoD as a whole and U.S. industry, it is vital to establish a U.S.-based program using LF-FSP to synthesize high purity, compositionally-controlled mixed-metal oxide nanopowders. Of equal importance is to develop general principles for processing mixed-metal oxide nanopowders first into green compacts with green densities in excess of 60% and thereafter into ultrafine- and even nano-grained transparent ceramics to optimize their laser properties. These represent general objectives addressed in the work undertaken in the performance of this project.

LF-FSP produced mixed-metal oxide nanopowders offer the potential to significantly impact the processing of optimal quality ceramic materials especially for optical, photonic and structural applications:

- Optical--Transparency with high strength
  - viewports for high pressure or harsh environment test/process chambers

- transparent, bullet-proof face shields for soldiers, police forces, e.g. bomb squad
- transparent, corrosion and, abrasion resistant radomes for IR[35] seeking missiles
- active electro-optic guard windows and spectral filters (utilizing poled ceramics)

• Photonics[10-16]
- low-cost lasers for applications ranging from cutting to surgical tools, surveying, etc.
- Low cost, high performance lasers for aerospace communications
- High performance lasers for antimissile/antisatellite programs
- High power lasers for fusion devices.
- High power, large aperture isolators for inertial fusion research.

• Structural applications
- Multifunctional, transparent YAG fibers for use as high temperature, low-creep fiber reinforced composites and as high temperature optical fibers for data transmission, sensing, e.g. in situ monitoring of aircraft turbine engine real-time behavior

• Power transmission in space
- High power lasers offer the potential to transmit terawatts of collected sunlight to space based installations and earth.

General processing issues

As noted above, the development of transparent envelopes for sodium vapor lamps has helped to identify basic guidelines for producing transparent ceramics based primarily on large grained materials. The basic issues that were addressed in efforts in this program are those listed below. Specific problems arise depending on the target materials and applications. For example, transparency for α-alumina is limited both by normal reflection and also because it is a hexagonal phase with different refractive indices along the a and c axes that create birefringence leading to an upper limit of ≈ 85% for transparency.

• Purity
- Residual transition metals, even at ppm levels, can strongly color materials.
- Impurity migration to grain boundaries during sintering scatters light leading at best to translucency.
- Mandates materials purity levels > 99.9%[2-6]

• Porosity
- Traps impurities including gases and water.[10-16]
- Both trapped impurities and pores cause severe light scattering.
- Requires sintering under vacuum, oxygen or hydrogen rich atmospheres

• Densification
- Controlled grain growth without impurities and porosity required to minimize scatter. Larger grains aid in minimizing scatter but reduce mechanical properties.
- Requires final grain sizes to be either < 0.5 μm[17]

These major concerns have driven our efforts todate.

Research Objectives

As noted above, Japanese researchers have developed polycrystalline Nd-doped YAG laser materials (Figure **2a**) by standard ceramic processing methods that outperform single crystal YAG lasers (Figure **2b**).[10-16] Final average grain sizes are 20-30 μm. These materials are produced via the 10 step process of Figure **1**. Thus, our initial objectives were to develop optimal routes to high quality, high purity nanopowders. Thereafter our efforts focused on developing routes to high quality powder compacts and finally processing routes to transparent polycrystal-

line photonic materials with submicron grain sizes. The first step in these efforts was upgrading our facilities. Fortunately, we were co-funded by Maxit Inc of Oslo, Norway to scale our efforts, which began with improving our production facilities.

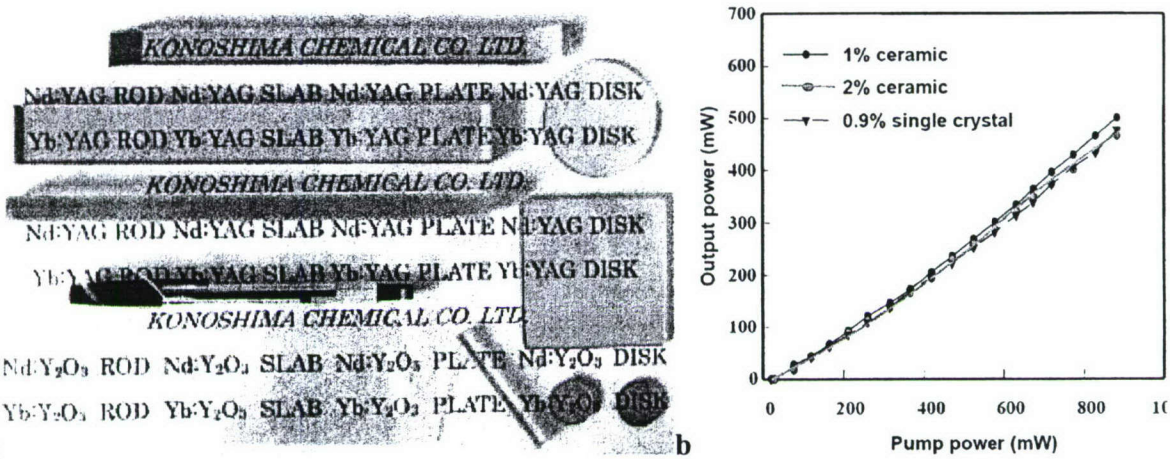

Figure 2. a. Konoshimas polycrystalline Nd-YAG, b. Laser output of ceramic Nd-YAG.

Processing superior nanopowders

Facilities

In the second year of our program, we improved all aspects of our production facilities per Figure **3**. Production or "shooting" rates went from 50 g/h to as much as 300 g/h for test runs

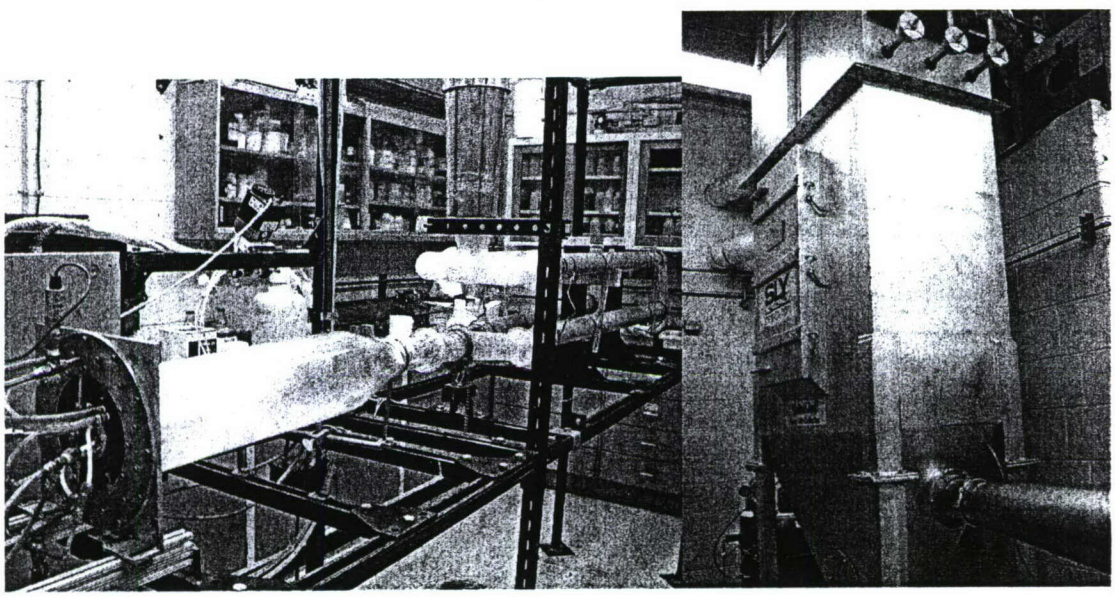

Figure 3. LF-FSP apparatus. Left format produces 100-300 g/h and 1- 2 kg/h in the right format.

and for large scale production the bag-house on the right side of Figure **3** allows shooting at 1-2 kg/h. The refinement of the facilities also led to improvements in our ability to combinatorial produce samples. We currently operate under the 5x5x25 scheme. We are in principle able to

produce five 30 g samples a day for a period of five days. Unfortunately, it takes some 25 weeks to characterize all the materials because we tend to make nanopowders with rare or hitherto unknown properties that require careful characterization to ensure that we have made the correct materials. Some examples of this are discussed in the next section.

Novel phases of nanopowders for transparent ceramics

YAG systems. As noted above LF-FSP[22] aerosolizes alcohol solutions of mixed-metal metalloorganic precursors such as the carboxylate mixture: $3Y(O_2CEt)_2OH/5Al(OCH_2CH_2)_3N$ containing 1-10 wt. % ceramic with O_2 into a quartz combustion chamber where the aerosol is ignited. Combustion temperatures reach 1600-2000°C followed by quenching at >1000°C/msec to produce nanopowders that are collected downstream in electrostatic precipitators.

Efforts to produce YAG nanopowders from this system led to the discovery of a completely new phase in the $Y_3Al_5O_{12}$ system, a novel perovskite like material. This new material was characterized in detail and its sintering behavior detailed for our transparent ceramics studies, as described in Appendix A, which is an electronic version of the published advanced materials paper.

1. R.M. Laine, J. Marchal, H.J. Sun, X.Q. Pan, "A new $Y_3Al_5O_{12}$ phase produced by liquid-feed flame spray pyrolysis (LF-FSP)," Adv. Mater. **17**, 830-33 (2005).

Note that these results already prove that we can skip 7 of the process steps shown in Figure **1** and prove the basis of our original arguments.

α-Al_2O_3. As note above, there is considerable interest in producing high quality transparent aluminas both for sodium vapor lamp envelopes, for transparent armor and for reasons discussed below, for new types of lasers. Work by Krell and Klimka, Figure **4**, demonstrates that it is possible to make transparent polycrystalline α-Al_2O_3.[27] However, the processing conditions shown

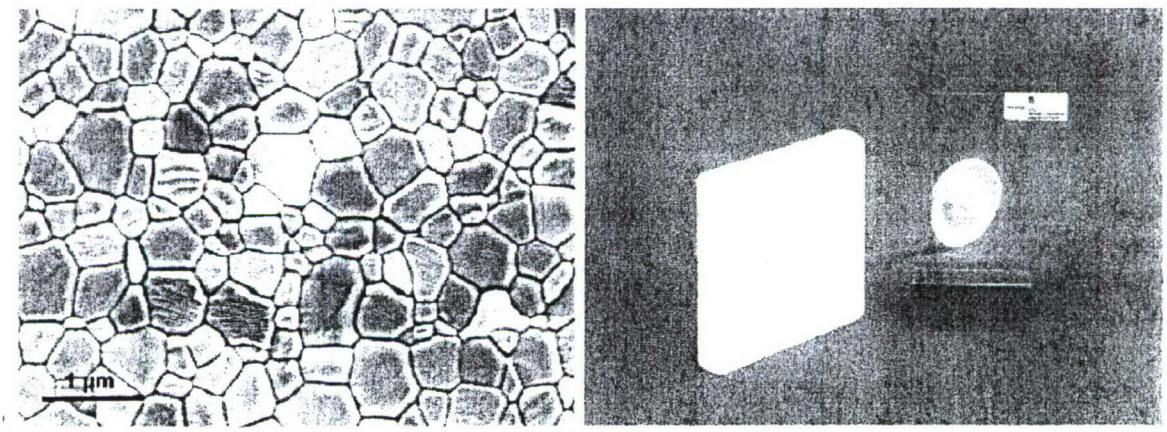

Figure **4**. a. Compact of 200 nm α-Al_2O_3 with 0.3 wt % MgO HIPped at 1250°C/12 h showing average grain sizes of 500 nm. b. With 0.3 % porosity, opaque material but with 0.03% porosity the material is transparent.

require exceptionally long times because the initial α-Al_2O_3 particles used in these studies were approximately $\geq$ 150 nm and as such, very low temperatures were required to avoid grain growth to obtain transparencies. These researchers have pointed out that if they had access to α-Al_2O_3 powders with grain sizes $\leq$ 100 nm, they would be able to produce much better products at

shorter processing times and temperatures such that these materials would be of use for sodium vapor lamp envelopes.

As part of our interest in making transparent materials and the potential to produce polycrystalline transparent α-Al_2O_3, with sufficiently high transparency that we could eventually make Cr^{3+} and/or Ti^{3+} doped ruby or Ti Sapphire lasers sought to make nano-α-Al_2O_3. Despite literature arguments that suggest that nano-α-Al_2O_3 may not exist, we were able to successfully make dispersible materials with average grain sizes of 30 nm. We were able to demonstrate a general route to nano-α-Al_2O_3 from multiple nano-sized transition alumina sources simply by dispersing these nano-alumina sources and passing them back through the LF-FSP apparatus.

This work, attached as Appendix B, was published in Nature Materials as:

2. R.M. Laine, J.C. Marchal, H.P. Sun, X.Q. Pan, "Nano-α-Al_2O_3 by liquid-feed flame spray pyrolysis (LF-FSP) of nano-transition aluminas," Nature Materials **5**, 710-2 (2006).

These powders can be pressureless sintered to 99$^+$% density with grain sizes of 400 nm, smaller than the average grain sizes seen in Figure **4** but still with some residual porosity. Given that the introduction of MgO at 0.3 wt % levels in the Figure **4** efforts helped reduce the final average grain sizes, we sought to dope our transition nano-δ-Al_2O_3 with Mg as a prelude to repassing these materials through the LF-FSP apparatus to make Mg doped nano-α-Al_2O_3.

Using combinatorial processing, we made a series of Mg doped powders. On characterization by XRD we discovered novel behavior. Figure **5** provides a stack of XRDs exemplifying combinatorial processing at the Al_2O_3 rich end of the MgO-Al_2O_3 tieline. We see for the first time a

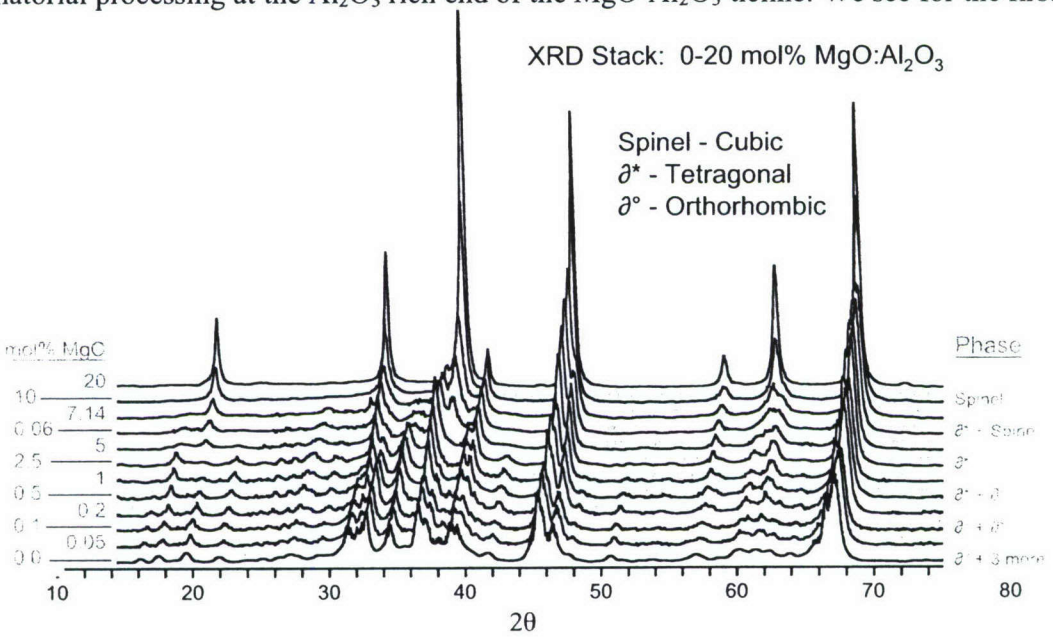

Figure 5. Combinatorial processing of at the alumina rich end of the MgO-Al_2O_3 tieline.

heretofore unknown phase pure spinel at 10 mol % MgO. This work is attached as Appendix C and will be published in Chemistry of Materials.

3. T. Hinklin, R. M. Laine, "Combinatorial synthesis of metastable phases in the magnesium spinel-alumina system," Chemistry of Materials in press.

Based on the observation of this very novel set of spinels, we decided that we should determine if LF-FSP offers the potential as a general route to wholly new phase pure spinels at compositions not see before. Figure **6**, provides XRDs of sets of spinel nanopowders that were made by LF-FSP for which there are no known examples in the literature.

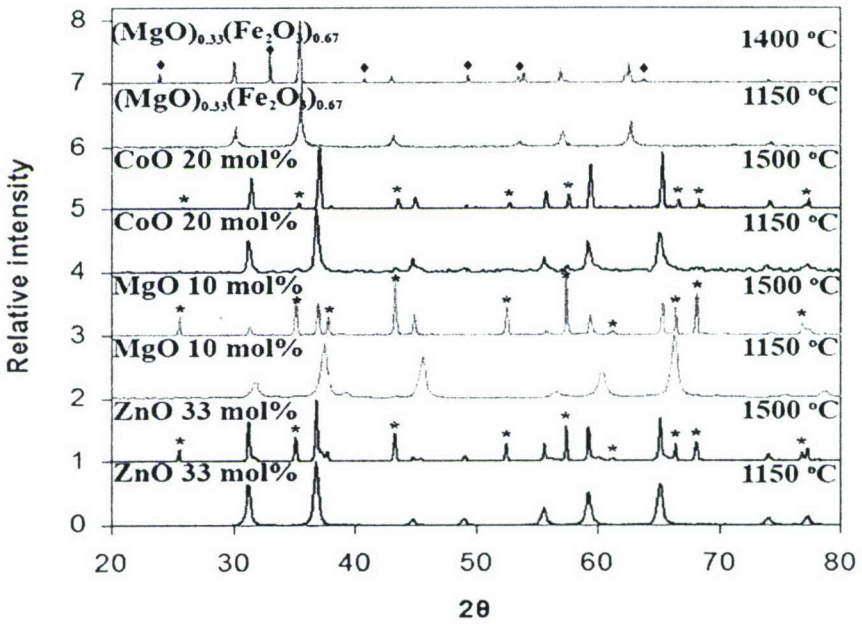

Figure 6. XRD powder patterns for $(MO)_x(Al_2O_3)_{1-x}$ for x as shown and $(MgO)_{0.33}(Fe_2O_3)_{0.67}$ for powders heated to 1150°C (10°C/min/air) or 1500°C/12 h. * = α-Al_2O_3, ◊ = α–Fe_2O_3 (1400°).

This work is detailed in Appendix D and was accepted in Advanced Materials with no revisions:

4. R. M. Laine, T.R. Hinklin, J. Azurdia, M. Kim, J.C. Marchal, S. Kumar, "Finding Spinel in All the Wrong Places," Adv. Mater. in press.

Still other papers on nanopowder syntheses were published as presented in Appendices E-G but are less related to the primary efforts and are not discussed here.

5. M. Kim, R.M. Laine, "Combinatorial processing of mixed-metal oxide nanopowders along the ZrO_2-Al_2O_3 tie line using liquid-feed flame spray pyrolysis (LF-FSP)," J. Ceramic Processing Research **8** 129-36 (2007).
6. J.A. Azurdia, J.C. Marchal, R.M. Laine, "Combinatorial processing of mixed-metal oxide nanopowders along the Co_3O_4-Al_2O_3 tie line using liquid-feed flame spray pyrolysis (LF-FSP)," J. Am. Ceram. Soc. **89**, 2749-56 (2006).
7. M. Kim, R.M. Laine, "Combinatorial processing of mixed-metal oxide nanopowders along the ZrO_2-Al_2O_3 tie line using liquid-feed flame spray pyrolysis (LF-FSP)," J. Ceramic Processing Research **8** 129-36 (2007).

Sintering and Upconversion Studies

Once we had developed routes to high quality nanopowders, we began collecting data on their processing and sintering behavior. Some of these efforts are described in the first three Appendices. Our most notable work is that on rare earth doped yttria nanopowders.

Recently, we have been successful in processing transparent rare earth doped yttria as exemplified by the materials shown in Figures **7** and **8**.

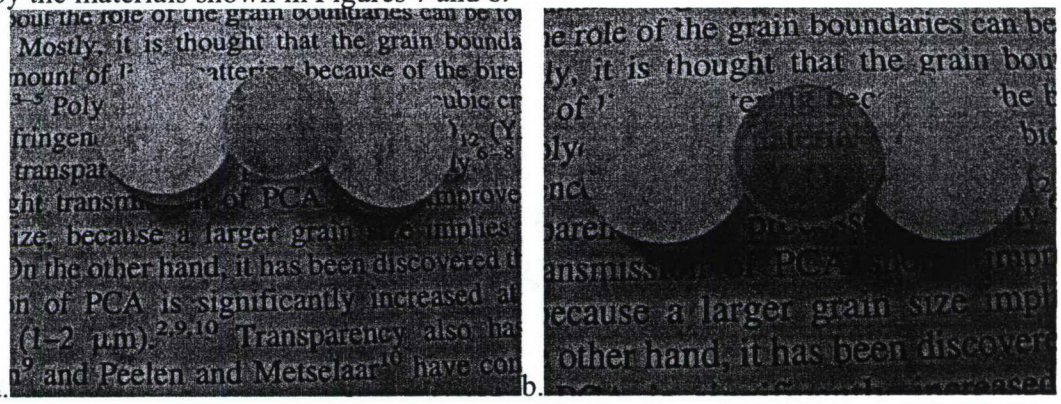

a. b.

Figure 7. a.$(Y_{0.929}Yb_{0.07}Tm_{0.001})O_3$ CIPped at 210 MPa, sintered 10°C/min to 1350°C/5 h, HIPped at 1350°C/3 h b. $(Y_{0.86}Yb_{0.11}Er_{0.03})_2O_3$ CIPped at 210 MPa, sintered 10°C/min to 1400°C/5 h, HIPped at 1400°C/3 h.

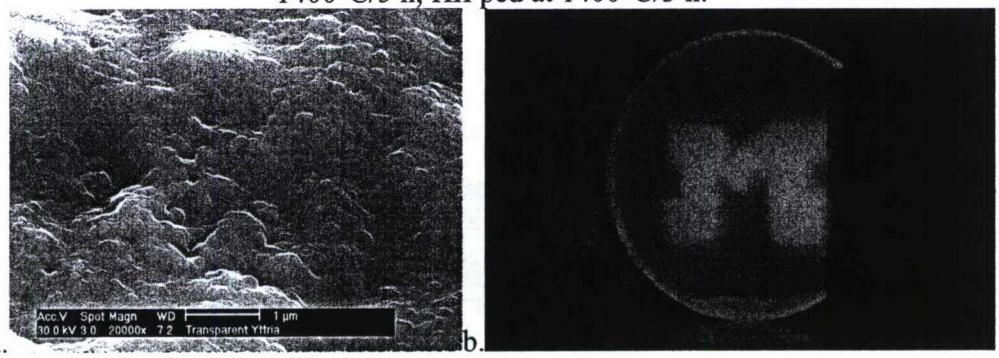

a. b.

Figure 8. a. Fracture surface of Figure **8b**. Upconversion of 960 nm light to 662 nm.

This work demonstrates: (1) nanostructured materials that are transparent, (2) multiple doping with rare earths can produce fully functional photonic materials, (3) and emissions from these materials can be much brighter than expected. The brightness of upconversion is probably related to the very high purity of the materials employed to make the transparent upconversion disk in Fig. **8b** and the high degree of crystallinity maintained in the processed, transparent ceramic. A complete manuscript describing this particular application is attached as appendix H and will be published shortly.

Laser Studies

Early in this program we demonstrated that LF-FSP alumina were also high quality precursor materials for transparent solids with potential laser applications. Alumina powders doped with rare earth ions were first shown to support random laser action in the as-grown form. The difference between emission output on several ultraviolet and visible luminescent transitions and the laser transition at 405 nm in Nd:Al_2O_3 powder excited by an electron beam in vacuum is shown

in Figure **9**. In the figure, only the 405 nm transition rises linearly above a threshold pumping rate, whereas other transitions, including other transitions from the same upper state of Nd, are quenched. This result confirmed that continuous-wave laser action can take place even without the presence of a laser cavity in electrically-pumped alumina powder. Hence in terms of purity the material was confirmed to be of laser-quality, setting the stage for the eventual preparation from them of bulk ceramic laser gain media. Also, this confirmed that the dopant sites were optically active as required for efficient laser action.

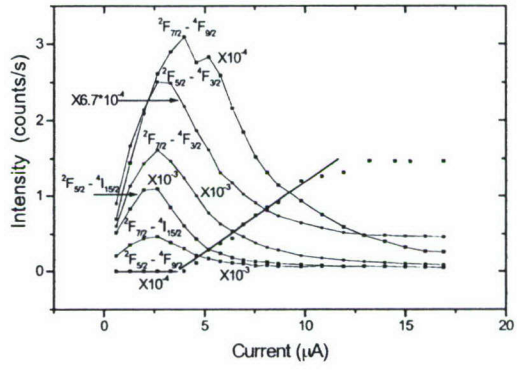

Figure 9. Emission intensities (UV-Vis transitions) in Nd:δ-Al_2O_3 show mirrorless laser action for $^2F_{5/2}$-$^4F_{9/2}$ transition w/ spectral quenching from gain competition on all other transitions.

Demonstration of laser action in nano-δ-alumina nanopowders raised the prospect of identifying new candidate laser materials during this project. In particular, nano-grained alumina was considered as a potential laser material capable of accommodating active ions that are difficult or impossible to incorporate in conventional (commercial) hosts that could even be given unique optical properties such as optical isotropy (unlike single crystal sapphire which is hexagonal and anisotropic). As a consequence we synthesized Sc:δ-Al_2O_3 nanopowders and found that after conversion to α-phase our samples did emit broadband UV-C radiation. This advance was published and not only identified a viable candidate for a ceramic UV laser but also an approach with significant promise for replacing decontamination light sources based on toxic Mercury sources, exploiting the intense UV-C emission indicated in Figure **10**.

These results on the optical properties of δ-alumina nanopowders prompted us to give some initial consideration to other broadband dopants that are well-suited to the alumina host and might yield unique new laser materials. One such dopant is the trivalent transition metal Ti^{3+} which is the pre-eminent active ion for tunable infrared and ultrashort pulse lasers. A unique light source that one can imagine based on controlled processing of nano-grained ceramic Ti^{3+}:Al_2O_3 is a Ti:sapphire fiber laser. Such a source cannot be made sintering micro-grained powders using Japanese ceramic processing because the final grain sizes are necessarily the size of the desired fiber core. Hence losses due to the birefringence of sapphire would be exhorbitant.

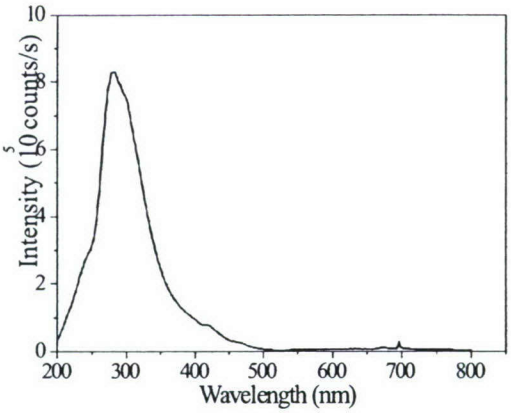

Figure 10. Broadband cathodoluminescence spectrum recorded at room temperature in Sc:Al_2O_3 after conversion of the host nanopowder to α-phase. The small feature visible at 672 nm is an intense Fano resonance associated with a very low concentration of Cr impurities.

This work was published as Appendix I:

8. B. Li, S. L. Oliveira, S. C. Rand, J.A. Azurdia, T. Hinklin, J. C. Marchal, R.M. Laine, "Ultraviolet emission and Fano resonance in doped nano-alumina," J. Appl. Physics, **101**, 053534 (2007).

Nor can Ti^{3+}:Al_2O_3 fibers be prepared by laser-heated pedestal growth of sapphire preforms because the Ti dopant is expelled very efficiently from the fiber as the melt front moves. However with nano-grained sapphire, the final fiber core size can in principle be on the order of the optical wavelength without incurring any scattering losses due to birefringence. In the small grain limit, the optical properties of sapphire are governed by effective medium properties that include isotropy of the refractive index. Hence birefringent scattering losses can be eliminated. Finally we are encouraged by the results of preliminary efforts at UM in which transparency has been achieved for sapphire grain sizes of approximately 200 nm. Optimistically, by employing inhomogeneous dopant distributions in extrudable powder preforms, one can anticipate small effective core sizes in Ti:sapphire fibers and successful single mode operation of a wideband fiber oscillator.

New Advances in Nanostructured Materials

Core shell nanopowders. Figure **11** shows TEMs of selected nanopowders produced in studies of $(ZrO_2)_x(Al_2O_3)_{1-x}$ nanopowders. We observe clear lattice fringes showing a high degree of crystallinity and strain, especially in the high zirconia content sample (49.7 mole % ZrO_2 in Al_2O_3, 79.4 mole % ZrO_2 in Al_2O_3). The lattice fringes are multi-directional and strain directions are different and multi-faceted in single particles, which is likely a consequence of particle formation during rapid quench from the gas phase.

The highest zirconia content sample (79.4 mole % ZrO_2 in Al_2O_3) images show the formation of core-shell materials. This corroborates the XRDs (Appendix I), indicating phase segregation between t-zirconia and δ-alumina. Since Al_2O_3 has a lower vaporization temperature (3000 °C) than ZrO_2 (5155 °C) in LF-FSP, ZrO_2 should condense and nucleate first from the gas phase fol-

lowed by Al_2O_3. We assume that t-zirconia nanoparticles form first during quenching, then δ-alumina nucleates on the t-zirconia nanoparticles forming the observed core-shell nanopowders

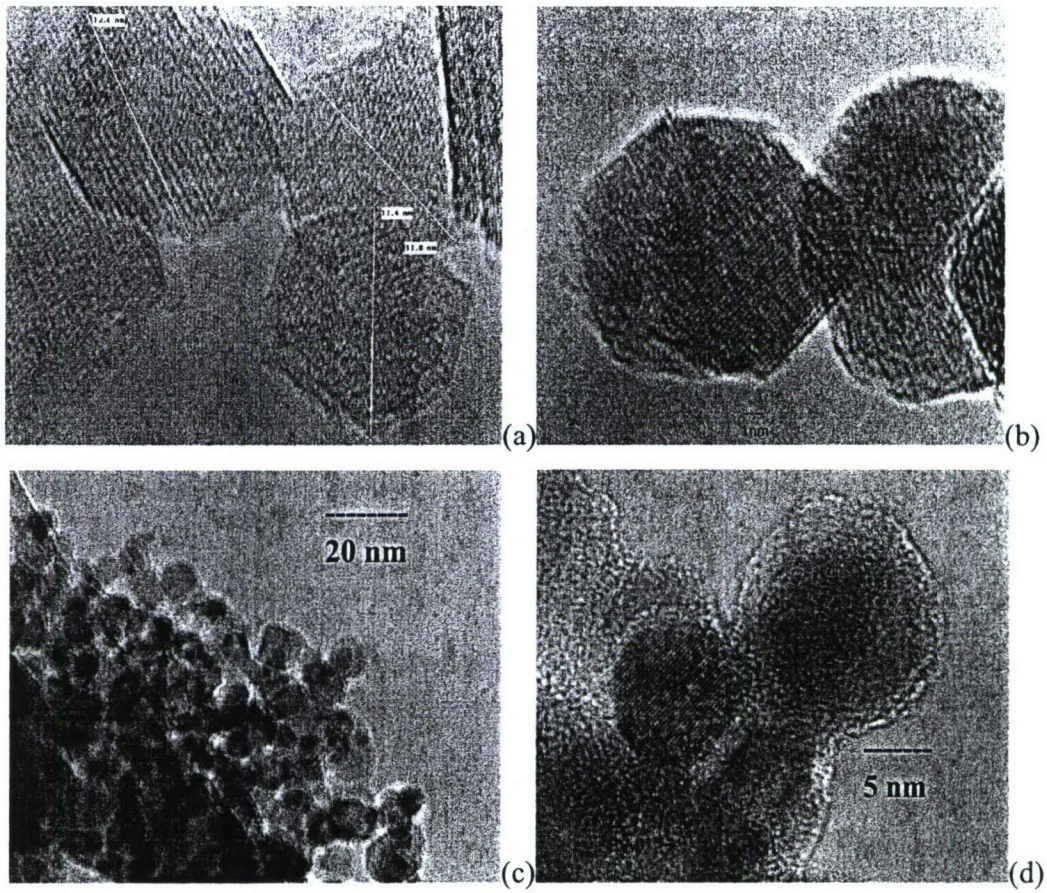

Figure 11. TEM micrographs of (a) 4.1 mole% ZrO_2 in Al_2O_3. (b) 49.7 mole % ZrO_2 in Al_2O_3. (c),(d) 79.4 mole % ZrO_2 in Al_2O_3.

in single step. We have also produced $(CeO_2)_x(Al_2O_3)_{1-x}$ nanopowders and $(Ce/ZrO_x)_x(Al_2O_3)_{1-x}$ nanopowders that also place the ceria and zirconia/ceria solid solution within an alumina shell. These materials sinter to full density, with the finest final grain structures we have seen to date. Furthermore, the zirconia maintains its tetragonal phase and the alumina is present as the alpha phase. These materials demonstrate transformation toughening without yttria additions and represent materials that have been impossible to produce before. They also provide a proof of concept for the production of transparent nanocomposites for dual functional lasers. Studies on the ZTA materials shown in Figure 11 are presented in Appendix J and have been published as:

9. M. Kim, R.M. Laine, "Combinatorial processing of mixed-metal oxide nanopowders along the ZrO_2-Al_2O_3 tie line using liquid-feed flame spray pyrolysis (LF-FSP)," J. Ceramic Processing Research **8** 129-36 (2007).

Bifunctional (multi-wavelength) lasers

The successful preparation during this project of nano-composites with good prospects for transparency (Figure **12**) gave rise to a new concept for solid state laser technology. By developing nano-composite laser hosts with chemical inhomogeneities on a scale much less than the optical wavelength, not only can optically uniform gain media be synthesized as we described earlier, but "bifunctional" laser media with the capability of operating simultaneously at two or more wavelengths become possible.

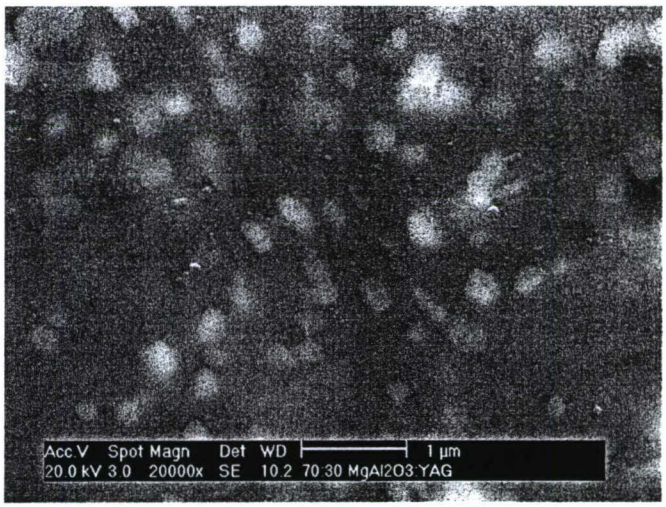

Figure 12. 70:30 $(MgO)_{0.40}(Al_2O_3)_{0.60}/Y_{3.5}Al_{4.5}O_{12}$ wt % sintered to 1450 °C leading to phase separation of YAG and spinel (white phase) both of which are potentially dopable providing potential access to bifunctional lasers

Nano-composites are intimately mixed, dual host materials. Consequently, the possibility of producing active hosts that can support laser action at more than one wavelength becomes a viable proposition. In the past, multi-wavelength lasers in homogeneous gain media exhibited instabilities due to nonlinear coupling between the dynamics at different wavelengths. This was due to the fact that there was only one active species supporting two different processes in the one material. Given two possible pathways on which to drive one sets of active ions, interference between them is inevitable. However, in nano-composites the gain regions for different wavelengths would be physically distinct. For example, gain for wavelength λ_1 would be confined to nanoparticles of type NP_1, whereas gain for wavelength λ_2 would be available only in nanoparticles of type NP_2, even if a single pumping source was used. Consequently the interplay of population dynamics would be eliminated and stable operation at two independently controllable wavelengths would be achieved.

References

1. a. R.L. Coble, "Transparent Alumina and Method of Preparation," U.S. Patent 3,026,210 (1962). b. Sintering Alumina. Effect of Atmosphere, J. Am. Ceram. Soc. **45**, 123-7 (1962).
2. a. W.H. Rhodes, G.C. Wei, "Ceramic Lamp Envelopes," in Concise Encyc. Of Advanced Ceramics, Ed. R.J. Brook, Pergammon Press, N.Y. 1990, pp 273-6. b. S.J. Bennison, M.P. Harmer, "A History of the Role of MgO in the Sintering of α-Al_2O_3, in Ceramic Trans. Vol. **7**, Sintering of Advanced Ceramics, Ed. C.A.

Handwerker, J.E. Blendell, W.A. Kaysser, Am. Ceram. Soc., Columbus, OH 1990, pp. 13-49. c. William Rhodes, private communication, June 10,2002.
3. a. D.J. Sellers, W.H.Rhodes, T. Vasilos, "Method of Preparing Transparent Alumina," U.S. Patent 3,899,560. b. W.H. Rhodes, F.J. Reid, "Transparent Yttria Ceramics and Method of Producing Same," U.S. Patent 4,098,612. c. W.H. Rhodes, "Transparent Yttria Ceramics and Method of Producing Same," U.S. Patent 4,147,744. d. W.H. Rhodes, F.J. Reid, "Transparent Yttria Ceramics Containing Magnesia or Magnesium Aluminate," U.S. Patent 4,174,973.
4. G.C. Wei, W.H. Rhodes, "Sintering Translucent Alumina in a Nitrogen-Hydrogen Gas Atmosphere," J. Am. Ceram. Soc. **83**, 1641-8 (2000). b. W.H. Rhodes, "Phase Chemistry in the Development of Transparent Polycrystalline Oxides," Phase Diagrams in Advanced Ceramics, A.M. Alper, ed., Academic Press, N.Y., N.Y. 1995 pp 1-39. c. W. H. Rhodes, P. L. Berenburg, J. E. Niesse, "Development of Transparent Spinel," AMMRC CR-70-19, 1970.
5. M.A. Parot, "Translucent Ceramics as Lamp Envelopes," Light. Res. Technol. **6**, 1114-22 (1974).
6. A.M. Thompson, M.P. Harmer, "Influence of Atmosphere on the Final Stage Sintering of Alumina to Theoretical Density," J. Am. Ceram. Soc. **76**, 2248-56 (1993).
7. "Ceramic Scintillators, C. Greskovich and S. Duclos, GE R&D Technical Information Series, Article 96CRD166. Dec. 1966.
8. C. Greskovich, J.P. Cernoch, "Polycrystalline Ceramic Lasers," J. Appl. Phys., **44**, 4599-4606 (1973).
9. C. Greskovich, J.P. Chernoch, "Improved Polycrystalline Ceramic Lasers," J. Appl. Phys. **45**, 4495-4502 (1974).
10. a. A. Ikesue, T. Kinoshita, "Fabrication and Optical Properties of High-Performance Polycrystalline Nd:YAG Ceramics for Solid State Lasers, J. Am Ceram. Soc. **78**, 1033-40 (1995). b. " J-G. Li, T. Ikegami, J-H. Lee, T. Mori, "Low-Temperature Fabrication of Transparent Yttrium Aluminum Garnet (YAG) Ceramics without Additives," J. Am. Ceram. Soc. **83**, 961-63 (2000). C. " J-G. Li, T. Ikegami, J-H. Lee, T. Mori, "Fabrication of Translucent Magnesium Aluminum Spinel Ceramics," J. Am. Ceram. Soc. **83**, 2866-8 (2000).
11. V. Lupei, T. Taira, N. Pavel, I. Shoji, A. Ikesue, "Laser emission under resonant pumping in the emitting level of highly doped Nd. Materials. Proceedings of the Conference on Lasers and Electro-Optics (CLEO '01), May, Baltimore, MD p. 559-60.
12. I. Shoji, S. Kurimura, Y. Sato, T. Taira, A. Ikesue, K. Yoshida, "Optical properties and laser characteristics of highly Nd^{3+} doped $Y_3Al_5O_{12}$ ceramics," Appl. Phys. Lett. **77**, 939-41 (2000).
13. J. Lu, M. Prabhu, J. Song, C. Li, J. Xu, K. Ueda, A.A. Kaminskii, H. Yagi, T. Yanagitani, "Optical properties and highly efficient laser oscillation of Nd:YAG ceramics," Appl. Phys. B 71, 469-73 (2000).
14. J. Lu, T. Murai, K. Takaichi, T. Uematsu, K. Misawa, M. Prabhu, K. Ueda, H. Yagi, T. Yanagitani, A.A. Kaminiskii, "High powder Nd:YAG ceramic laser," Proceedings of the Conference on Lasers and Electro-Optics (CLEO '01), May, Baltimore, MD p. 560.
15. I. Shoji, Y. Sato, S. Kurimura, T. Taira, A. Ikesue, K. Yoshida, "Thermal birefringence in Nd^{3+} doped YAG ceramics," Proceedings of the Conference on Lasers and Electro-Optics (CLEO '01), May, Baltimore, MD pp. 560-1.
16. a. K. Ueda et al in Proceedings of the Conference on Lasers and Electro-Optics CLEO '02) May, Long Beach, CA pp. b. J-G. Li, T. Ikegami, J.-H. Lee, T. Mori, Y. Yajima, "Reactive yttrium aluminate garnet powder via coprecipitation using ammonium hydrogen carbonate as the precipitant, J. Mater. Res. **15**, 1864-66 (2000).
17. R. Apetz, M.P.B van Bruggen, "Transparent Alumina: A Light Scattering Model," *J. Am. Ceram. Soc.* **86**, 480-6 (2003).
18. W.H. Rhodes, "Agglomerate and Particle Size Effects on Sintering Yttria-Stabilized Zirconia," J. Am. Ceram. Soc. **64**, 19-22 (1981). This is the first example of sintering of nanopowders to high density at low temperatures.
19. G. Skandan, H. Hahn, and J.C. Parker, "Nanostructured Y_2O_3: Synthesis and relation to microstructure and properties," Scripta Metall. et. Mater. **25**, 2389-93 (1991).
20. M. R. Gallas, B. Hockey, A. Pechenik, and G. J. Piermarini, "Fabrication of Transparent γ-Al_2O_3 from Nanosize Particles," J. Am. Ceram. Soc., **77**, 2107-12, (1994).
21. C.R. Bickmore, K.F. Waldner, D.R. Treadwell, R.M. Laine, "Ultrafine Spinel Powders by Flame Spray Pyrolysis of a Magnesium Aluminum Double Alkoxide," J. Am. Ceram. Soc. 79, 1419-23 (1996).
22. C.R. Bickmore, K.F. Waldner, R. Baranwal, T. Hinklin, D.R. Treadwell, R.M. Laine, "Ultrafine Titania by Flame Spray Pyrolysis of a Titanatrane Complex: Part I," J. Europ. Ceram. Soc. **18**, 287-97 (1998).
23. R. Baranwal, M. P. Villar, R. Garcia and R. M. Laine, "Synthesis, Characterization, and Sintering Behavior of Nano-mullite Powder and Powder Compacts," J. Am. Ceram. Soc. **84**, 951- 61 (2001).

24. A.C. Sutorik, S.S. Neo, T. Hinklin, R. Baranwal, D.R. Treadwell, R.Narayanan, R.M. Laine, "Synthesis of Ultrafine β"-Alumina Powders via Flame Spray Pyrolysis of Polymeric Precursors," J. Am. Ceram. Soc. **81**, 1477-86 (1998).
25. A.C. Sutorik and M.S. Baliat, "Solid-solution behavior of $Ce_xZr_{1-x}O_2$ Prepared by Flame Spray Pyrolysis of Solvent-Borne Precursors," J. of Metastable and Nanocrystalline Materials, **13**,371-6 (2002)
26. J. Marchal, T. Hinklin, R. Baranwal, T. Johns, and R. M. Laine, "Yttrium aluminum garnet nanopowders by flame spray pyrolysis," Chem. Mater. **16**, 822-831 (2004).
27. A. Krell, J. Klimke, J. Am. Ceram. Soc., **89**, 1985-92 (2006).

Personnel Supported

Mr. Julien Marchal, Thomas Hinklin (Graduate Students).
Mr. Bin Li

Publications

1. J. Marchal, J. Azurdia, R.M. Laine, "The Gas-Phase Synthesis of nano-α-Alumina from Liquid-Feed Flame Spray Pyrolysis (LF-FSP) of nano-δ-alumina," in preparation.
2. R.M. Laine, J. Marchal, S. Kim, J. Azurdia, M. Kim, "Liquid-Feed Flame Spray Pyrolysis of Single and Mixed Phase Mixed-Metal Oxide Nanopowders," in Ceramic Nanomaterials and Nanotechnology III, S. Lu, M.Z. Hu, Y. Gogotsi eds, Ceramic Transactions Vol. **159**, 2004, pp 22-29.
3. R.M. Laine, J. Marchal, H.J. Sun, X.Q. Pan, "A new $Y_3Al_5O_{12}$ phase produced by liquid-feed flame spray pyrolysis (LF-FSP)," Adv. Mater. **17**, 830-33 (2005).
4. J.A. Azurdia, J.C. Marchal, P. Shea, H. Sun, X. Q. Pan, R.M. Laine; "Liquid-feed flame spray pyrolysis (LF-FSP) as a method of producing mixed-metal oxide nanopowders of potential interest as catalytic materials. Nanopowders along the $NiO-Al_2O_3$ tie-line including $(NiO)_{0.22}(Al_2O_3)_{0.78}$, a new inverse spinel composition." Chemistry of Materials, Revised paper submitted.
5. R.M. Laine, J.C. Marchal, H.P. Sun, X.Q. Pan, "Nano-α-Al_2O_3 by liquid-feed flame spray pyrolysis (LF-FSP) of nano-transition aluminas," Nature materials to be revised.
6. J.A. Azurdia, J.C. Marchal, R.M. Laine, "Combinatorial processing of mixed-metal oxide nanopowders along the $Co_3O_4-Al_2O_3$ tie line using liquid-feed flame spray pyrolysis (LF-FSP)," manuscript to be submitted.
7. S. Kim, M. Kim, R.M. Laine, "Combinatorial processing of mixed-metal oxide nanopowders along the $CuO-Al_2O_3$ tie line using liquid-feed flame spray pyrolysis (LF-FSP)," manuscript to be submitted.
8. S. Kim, M. Kim, R.M. Laine, "Combinatorial processing of mixed-metal oxide nanopowders along the $ZnO-Al_2O_3$ tie line using liquid-feed flame spray pyrolysis (LF-FSP)," manuscript to be submitted.
9. T. R. Hinklin, R.M. Laine, "Combinatorial processing of mixed-metal oxide nanopowders along the $MgO-Al_2O_3$ tie line using liquid-feed flame spray pyrolysis (LF-FSP)," manuscript to be submitted.
10. R.M. Laine, J. Marchal, J. Azurdia, "Liquid Feed Flame Spray Modification of Nanoparticles," filed.
11. S.M. Redmond, S.L. Oliveira, G.L. Armstrong, H.-Y. Chan, E. Mattson, A. Mock, B. Li, J.R. Potts, S.C. Rand, J. Marchal, T. Hinklin, and R.M. Laine, "Electrical Generation of Stationary Light in Random Scattering Media", J.O.S.A. B21, (2004).
12. S.M. Redmond, S.C. Rand, X. Ruan, and M. Kaviany, "Multiple scattering and nonlinear thermal emission of Yb^{3+},Er^{3+}:Y_2O_3 nanopowders", J. Appl. Phys. 95, 4069 (2004).
13. B. Li and S.C. Rand, "Coherence experiments in a random color center laser system", Int. Quantum Electronics Conf. (IQEC '04), San Francisco, CA, May 16-21, 2004, paper IFB2.
14. B. Li and S.C. Rand, "Nonlinear spectral quenching in random lasers", Nonlinear Optics Topical Meeting, Hawaii, Aug. 2-6(2004), paper ThB2.
15. B. Li, T. Hinklin, R.M. Laine and S.C. Rand, "Ultraviolet Nanophosphors", J. Lumin. 122-123, 345-347 (2007).
16. B. Li and S.C. Rand, "Continuous-wave amplification and light storage in optically- and electrically-pumped random media", J.O.S.A. B.24, 799 (2007)
17. X. Ruan, S.C. Rand and M. Kaviany, "Entropy and efficiency in laser cooling of solids" Phys. Rev. B75, 214304(2007).
18. B. Li, S. L. Oliveira, S.C. Rand, J. A. Azurdia, T. R. Hinklin, J. C. Marchal, and R.M. Laine, "Ultraviolet emission and Fano resonance in doped nano-alumina", J. Appl. Phys.101, 053534 (2007).
19. S.L. Oliveira and S.C. Rand, "Intense nonlinear magnetic dipole radiation at optical frequencies, molecular scattering in a dielectric liquid", Phys. Rev. Lett. 98, 093901 (2007).

S.C. Rand, S.L. Oliveira, L. A. Gómez, L. H. Acioli and C. B. de Araújo, "Optically-induced Magnetic Interactions in Nonlinear Optics", in *Nonlinear Optics and Recent Advances in Optics*, ed. H. Abdeldayem, Research Signpost, Chapter 12, pp. 299-318, 2007.

Transitions

Alpha-alumina nanopowder processing methods have been patented and the University of Michigan is in the process of licensing this technology to Nano-Alpha a spin-off of the Laine group.

A patent application was filed:

1. R.M. Laine, J. Marchal, J. Azurdia, "Liquid Feed Flame Spray Modification of Nanoparticles," filed.

(15 coronal slices, repetition time (TR)/echo time (TE) = 635/17 ms, FOV = 20 cm × 20 cm, acquisition matrix = 320 × 512, flip angle = 90°, slice thickness = 1.5 mm with no gap, number of averages = 3).

Received: July 12, 2004
Final version: November 8, 2004

[1] M. E. Ladd, H. H. Quick, J. F. Debatin, *J. Magn. Reson. Imaging* **2000**, *12*, 534.

[2] a) G. Decher, *Science* **1997**, *277*, 1232. b) J. Park, P. T. Hammond, *Adv. Mater.* **2004**, *16*, 520. c) C. Picart, J. Mutterer, L. Richert, Y. Luo, G. D. Prestwich, P. Schaaf, J.-C. Voegel, P. Lavalle, *Proc. Natl. Acad. Sci. USA* **2002**, *99*, 12531. d) V. Phuvanartnuruks, T. J. McCarthy, *Macromolecules* **1998**, *31*, 1906. e) N. Jessel, F. Atalar, P. Lavalle, J. Mutterer, G. Decher, P. Schaaf, J.-C. Voegel, J. Ogier, *Adv. Mater.* **2003**, *15*, 692. f) N. Benkirane-Jessel, P. Schwinté, P. Falvey, R. Darcy, Y. Hadkel, P. Schaaf, J.-C. Voegel, J. Ogier, *Adv. Funct. Mater.* **2004**, *14*, 174. g) P. T. Hammond, *Adv. Mater.* **2004**, *16*, 1271.

[3] a) B. Thierry, F. M. Winnik, Y. Mehri, J. Silver, M. Tabrizian, *Biomacromolecules* **2003**, *4*, 1564. b) B. Thierry, F. M. Winnik, Y. Mehri, M. Tabrizian, *J. Am. Chem. Soc.* **2003**, *125*, 7494.

[4] X. Jiang, H. Yu, R. Frayne, O. Unal, M. Strother, *Chem. Mater.* **2002**, *14*, 1914.

[5] S. Gouin, M. V. Valencia Grayeb, F. M. Winnik, *Macromol. Symp.* **2002**, *186*, 105.

[6] L. Richert, P. Lavalle, E. Payan, X. Z. Shu, G. D. Prestwich, J.-F. Stoltz, P. Schaaf, J.-C. Voegel, C. Picart, *Langmuir* **2004**, *20*, 448.

[7] a) P. Lavalle, V. Vivet, N. Jessel, G. Decher, J.-C. Voegel, P. J. Mesini, P. Schaaf, *Macromolecules* **2004**, *37*, 1159. b) J. M. Garza, P. Schaaf, S. Muller, V. Ball, J.-F. Stoltz, J.-C. Voegel, P. Lavalle, *Langmuir* **2004**, *20*, 7298.

[8] a) F. Hook, B. Kasemo, T. Nylander, C. Fant, K. Sott, H. Elwing, *Anal. Chem.* **2001**, *73*, 5796. b) M. V. Voinova, M. Jonson, B. Kasemo, *Biosens. Bioelectron.* **2002**, *17*, 835.

[9] C. Picart, P. Lavalle, P. Hubert, F. J. G. Cuisinier, G. Decher, P. Schaaf, J.-C. Voegel, *Langmuir* **2001**, *17*, 7414.

[10] a) S. Park, J. P. Bearinger, E. P. Lautenschlager, D. G. Castner, K. E. Healy, *J. Biomed. Mater. Res.* **2000**, *53*, 568. b) S. P. Ho, N. Nakabayashi, Y. Iwasaki, T. Boland, M. Laberge, *Biomaterials* **2003**, *24*, 5121.

A New $Y_3Al_5O_{12}$ Phase Produced by Liquid-Feed Flame Spray Pyrolysis (LF-FSP)**

By *Richard M. Laine*,* *Julien Marchal*, *Haiping Sun*, and *Xiao Qing Pan*

Yttrium aluminum garnet (YAG, $Y_3Al_5O_{12}$) materials have been studied extensively over many decades because of their exceptional high-temperature mechanical strength coupled with low creep, utility as phosphors, and, most importantly, their photonic properties.[1–5] Single-crystal YAG dominates commercial solid-state laser markets while also offering aesthetic beauty as YAG jewelry.

Laser applications have provided the impetus for in-depth examinations of the properties and processing of $Y_3Al_5O_{12}$ composition melts, glasses, and single-phase materials.[6–10] The recent advent of transparent polycrystalline YAG lasers that outperform single-crystal YAG lasers has intensified interest in the development of very fine YAG particles that are easily sintered to full density and transparency.[11,12] We report here efforts to produce nanosized $Y_3Al_5O_{12}$ powders for this purpose that result in a new phase with higher densities than YAG and sinter to full density at relatively low temperatures.

We recently described a new method of producing large quantities of single and mixed-metal oxide nanopowders with exceptional control of composition based on liquid-feed flame spray pyrolysis. (LF-FSP).[13] In this process, metallo-organic precursors (e.g., metal carboxylates) with the exact composition of the metals desired in the final oxide nanopowders are dissolved in an alcohol (typically ethanol) and the solutions aerosolized with oxygen. The aerosol mist is ignited to produce flame temperatures exceeding 1500 °C. Rapid quenching of the gas-phase species produces nanosized oxide "soot" with the exact metal composition of the starting solution, including any impurities or dopants. Given that nanosized oxide powders are known to sinter at temperatures well below those of micrometer-sized powders, a set of precursors designed to produce the $Y_3Al_5O_{12}$ composition were assessed. The resulting nanopowder was found to form a new hexagonal $Y_3Al_5O_{12}$ phase, which we describe here.

In studies reported in detail elsewhere,[13] we found that 3:5 mixtures of $Y(O_2CCH_2CH_3)_2OH$ and $Al(Acac)_3$ (Acac = acetylacetonate) dissolved in ethanol gave nanopowders with average particle sizes (APS) below 50 nm (Fig. 1a). The as-produced particles are unnecked, easily dispersed, and single crystals, as determined by high-resolution TEM (Fig. 1b).

In contrast to what we anticipated, the digital diffraction and XRD powder patterns for the as-produced powders do not match those of YAG. As shown in Figure 2, the XRD most closely resembles that of the hexagonal phase of $YAlO_3$. Since this is a commonly observed kinetic phase in this system, this finding was not too surprising. However, if we had produced $YAlO_3$, then the overall stoichiometry of the system would be $3YAlO_3{\cdot}Al_2O_3$. The excess alumina (25 mol-%) would be expected to be visible as a crystalline phase (not observed), an amorphous phase with an amorphous hump in the XRD powder patterns (not observed), or last (and least likely), as a component in a defect structure.

On careful examination, the XRD peak intensities obtained differ from those expected for $YAlO_3$. This prompted examination of the low-angle XRD pattern, revealing a peak at $2\theta = 8.3$–$8.5°$ corresponding to a lattice parameter of ≈ 1.1 nm, close to the unit-cell dimensions for crystalline YAG and the (001) interplanar distance of hexagonal $YAlO_3$. However, neither true YAG samples (obtained after annealing at 1200 °C for 30 min) nor authentic samples of LF-FSP nanohexagonal

[*] Prof. R. M. Laine, J. Marchal, Dr. H. Sun, Prof. X. Q. Pan
Department of Materials Science and Engineering
University of Michigan
Ann Arbor, MI 48109-2136 (USA)
E-mail: talsdad@umich.edu

[**] J. M. and R. M. L. thank AFOSR (F49620-03-1-0389) for support of this work.

  DOI: 10.1002/adma.200401001

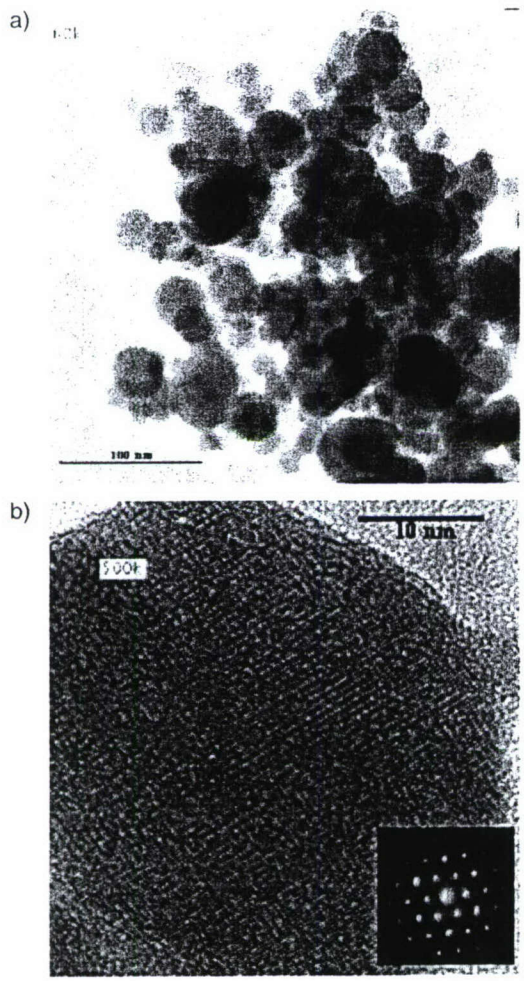

Figure 1. a) Transmission electron microscopy (TEM) of LF-FSP-produced $Y_3Al_5O_{12}$ composition nanopowders and b) high-resolution TEM (HRTEM) of single crystal with digital diffraction pattern (inset). (APS measured as 20–50 nm by X-ray diffraction [XRD] line broadening; surface area of 40–90 $m^2 g^{-1}$ determined by Brunauer–Emmett–Teller [BET] surface area analysis.)

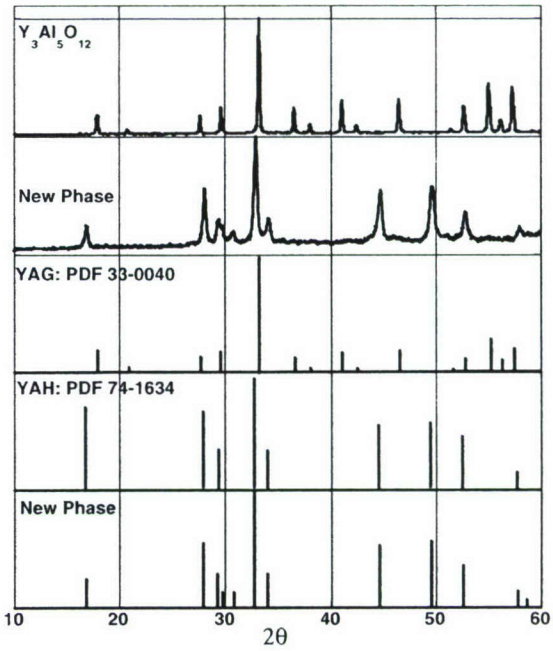

Figure 2. XRD patterns of a) YAG from annealed powder; b) new phase (low-angle peak at $2\theta = 8.2°$ not shown); c) YAG (International Centre for Diffraction Data [ICDD] No. 33-0040); d) hexagonal $YAlO_3$ (ICDD No. 74-1634); e) simulation of XRD powder pattern of new phase (see Experimental).

$YAlO_3$ show this peak. These are respectively due to the structure factor of YAG and the equivalency of the $YAlO_3$ (002) and (001) planes.

Fourier-transform IR (FTIR) studies also suggest a novel material. The $Y_3Al_5O_3$ composition powders contain small but typical O–H and carbonate C–O bands in the 3400–3600 cm^{-1} and 1400–1600 cm^{-1} regions, respectively. Both result from the high concentrations of water and CO_2 in the flames. Likewise, peaks for Al–O and Y–O are common to most of the materials along the the Y_2O_3–Al_2O_3 couple. However, one peak at 740 cm^{-1} is unique to the new material. This peak is usually assigned to asymmetric Al–O in *isolated* AlO_4 tetrahedra, as in the YAG phase. Alternately, it is observed for specific interactive vibrations between AlO_4 or AlO_5 species bound to AlO_6 octahedra, as discussed by Saniger[14] and Tarte.[15] Restated, this band appears when at least one AlO_4 or AlO_5 species forms Al–O–Al(Y) bonds with a second AlO_6 species. As such, this peak is not observed in δ-alumina, $Al(OH)_3$, or hexagonal $YAlO_3$.

In the Y_2O_3–Al_2O_3 system, this peak might be expected if excess Al^{3+} (Y/Al ratio < 1) substitutes for Y^{3+} in the hexagonal $YAlO_3$ phase, resulting in AlO_6 octahedra connected to AlO_4 or AlO_5 species, forming a regular defect structure.

Random substitution of Y^{3+} by Al^{3+} would not show either the 740 cm^{-1} FTIR peak or differences in the XRD pattern. Furthermore, the XRD powder pattern reported above can be closely simulated (Fig. 2; see Experimental) in terms of peak positions and intensities, suggesting a regular atomic ordering of atoms and thus a new phase of $Y_3Al_5O_{12}$ composition.

The simulation also allows us to suggest a hexagonal structure for the new phase with $a = 0.736$ nm and $c = 1.052$ nm. This unit cell resembles hexagonal $YAlO_3$, but is four times bigger and has a regular defect structure in the (002) plane: half of the Y^{3+} are substituted by Al^{3+}, forming a regular pattern. The structure, shown in Figure 3, is best described layer by layer (all parallel to the 001 plane). Layer a consists of a hexagonal layer of yttrium ions, while layer b is a hexagonal layer of oxygen ions. Layer c is a hexagonal layer of alternating five coordinated Al^{3+} and O^{2-} ions, while layer d consists of a hexagonal layer of alternating octahedral Y^{3+} and octahedral Al^{3+} ions. Thus, the unit cell consists of an ABCBDBCBA arrangement, contrasting with the ABCBABCBA layers of hexagonal $YAlO_3$. This causes the extra $2\theta = 8.4°$ peak in the low-angle

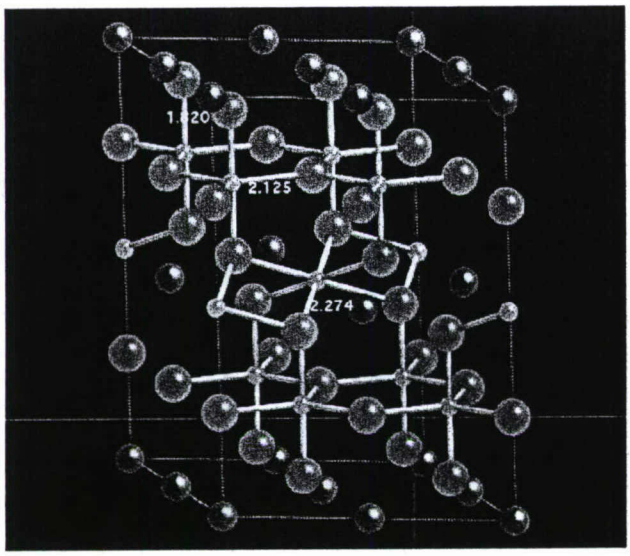

Figure 3. Three-dimensional model of the hexagonal $Y_3Al_5O_{12}$ crystal structure (grey: yttrium; red: oxygen; blue: aluminum). The three different Al–O bond distances are indicated in white.

XRD pattern. These unit-cell dimensions indicate that the density of this material is 5.52 g cm^{-3} versus 4.51 g cm^{-3} for YAG.

The literature on YAG glasses[8,9] suggests formation of two glass phases, one having a lower density than the other and being the thermodynamically most stable of the two. It is tempting to argue that LF-FSP-produced hexagonal $Y_3Al_5O_{12}$ may arise from gas-phase formation of the more dense of these two glasses, followed by crystallization. However, the structure of these materials is dominated by a tetrahedral-alumina framework, which differs from that observed here where it appears that the only Al^{3+} ions present are penta- or hexa-coordinate. As YAG glasses form with all three Al^{3+} ion types, a different crystallization route seems more probable.

Thermal gravimetric analysis–differential thermal analysis (TGA–DTA) showed a single-step conversion to the YAG phase around 1100 °C. To determine the activation energy (E_a), we used the constant-heating method and the modified Kissinger equation

$$\ln\left(\frac{\alpha}{T_m - T_0}\right) = \frac{1}{T_m}\frac{E_a}{R} + k_0 \quad (1)$$

to calculate E_a from the shift of the YAG exotherm in the DTA ($T_m - T_0$, where T_m and T_0 are the peak temperatures observed with heating rates of α and α_0, respectively) with changes in heating rate, and where k_0 is a constant dependent on the reference heating rate α_0 and R is the universal gas constant.[1] The E_a for conversion to the YAG phase was determined to be ≈110 kJ mol^{-1},[13] which is much lower than the 550 kJ mol^{-1}[16] reported for conversion from $YAlO_3$ and Al_2O_3 to YAG. Hence, there appears to be a very strong driving force for formation of the YAG phase. This driving force when coupled with the roughly 20 % higher density of the hexagonal phase should provide improved sintering, as conversion to the lower-density YAG phase may aid in removing porosity during the sintering process. This prompted the following sintering studies.

Powders were milled and ultrasonically dispersed with 2 wt.-% poly(ethylene oxide)/poly(vinyl alcohol) (PEO/PVA) binder to remove weak agglomerates and then uniaxially pressed to 120 MPa providing green bodies with densities of 63–64 % of theory. These pellets were sintered to nearly full density at 1400 °C (heated at 10 °C min^{-1} to 800 °C for 2 h, then at 10 °C min^{-1} to 1000 °C for 2 h under vacuum, then at 10 °C min^{-1} to 1400 °C for 6 h) while maintaining grain sizes less than 500 nm (Fig. 4); this will be discussed in detail in a full paper.

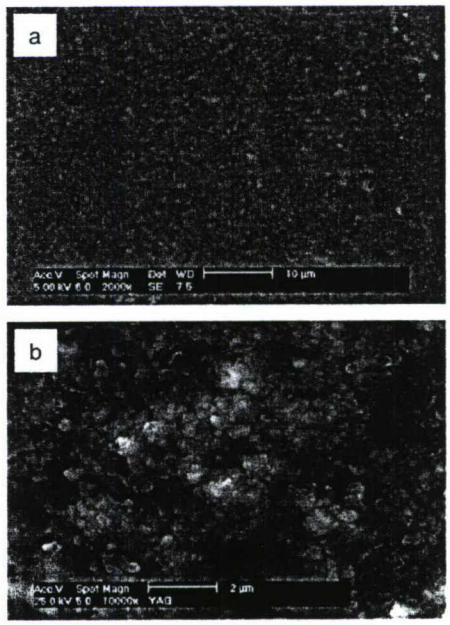

Figure 4. Hexagonal $Y_3Al_5O_{12}$ compacted green powder heated at 10 °C min^{-1} to 800 °C under O_2, then at 10 °C min^{-1} to 1000 °C under vacuum for 2 h, then at 10 °C min^{-1} to 1400 °C for 6 h. a) Cut and polished surface; b) fracture surface.

In summary, the LF-FSP process allows the synthesis of a new hexagonal $Y_3Al_5O_{12}$ phase characterized using FTIR, XRD, TGA–DTA, and TEM. The new phase is calculated to be 20 % denser than the YAG phase, which can be used to advantage in sintering to full density. The as-processed material consists of a spherical, easily dispersed, high-surface-area (70–90 m^2 g^{-1}) nanopowder that converts to the YAG phase with an activation energy of ≈110 kJ mol^{-1}. Hexagonal $Y_3Al_5O_{12}$ nanopowder is easily processed with small amounts of binder and can be uniaxially pressed into green bodies at 62–64 % of theoretical density and then sintered to essentially full density at 1400 °C. The LF-FSP process allows doping and should provide access to hexagonal $Y_3Al_5O_{12}$ nanopowders with rare-earth dopants (e.g., Nd, Y) of use in producing polycrystalline, transparent YAG lasers.

Experimental

Precursor Materials and Nanopowders: These materials and their methods of preparation are described in a previous paper [13].

X-ray Diffraction Studies: As-prepared and calcined samples were characterized using a Rigaku Rotating Anode Goniometer. Details are provided in a previous paper [13]. Low-angle XRD scans were also obtained from $2\theta = 4$–$10°$ using a scan rate of $0.25° \text{ min}^{-1}$ in 0.01° increments. Jade (Version 3.1 from Materials Data, Inc., Livermore, CA) was used to identify the crystallographic phases and relative phase compositions. CrystalMaker and CrystalDiffract (Versions 6 and 4, respectively, from CrystalMaker, Bicester, UK) were used to model the new phase and to simulate the XRD pattern.

Diffuse-reflectance Fourier-transform IR spectra (DRIFTS), specific surface analyses (Brunauer–Emmett–Teller analysis), and scanning electron microscopy data were recorded as described elsewhere [13].

Transmission Electron Microscopy: Micrographs were obtained using a JEOL 2100 XL. Samples were prepared using a carbon-coated copper TEM grid (300 mesh). The powder was dispersed in distilled water using an ultrasonic horn as before [13], and then a drop of the dispersed powder/water mixture was deposited on the grid. The grid was then dried for 4 h at 80 °C. The JEOL 2100 XL was used with an accelerating voltage of 200 kV.

Received: June 24, 2004
Final version: October 28, 2004

[1] W. R. Blumenthal, D. S. Phillips, *J. Am. Ceram. Soc.* **1996**, *79*, 1047.
[2] S. Karato, Z. Wang, K. Fujino, *J. Mater. Sci.* **1994**, *29*, 6458.
[3] Y. Pan, Y. Sun, M. Wu, Q. Su, *J. Phys. Chem. Solids* **2004**, *65*, 845.
[4] Y. H. Zhou, J. Lin, M. Yu, S. M. Han, S. B. Wang, H. J. Zhang, *Mater. Res. Bull.* **2003**, *38*, 1289.
[5] J. McKittrick, L. E. Sheab, C. F. Bacalskia, E. J. Boszea, *Displays* **1999**, *19*, 169.
[6] K. Nagashio, K. Kuribayashi, *Acta Mater.* **2001**, *49*, 1947.
[7] P. Yang, P. Deng, Z. Yin, Y. Tian, *J. Cryst. Growth* **2000**, *218*, 87.
[8] M. C. Wilding, P. F. McMillan, A. Navrotsky, *Phys. Chem. Glasses* **2002**, *43*, 306.
[9] M. C. Wilding, P. F. McMillan, A. Navrotsky, *Physica A (Amsterdam, Neth.)* **2002**, *314*, 379.
[10] J. Zhang, J. Ning, X. Liu, Y. Pan, L. Huang, *J. Mater. Sci. Lett.* **2003**, *22*, 13.
[11] A. Ikesue, K. Yoshida, K. Kamata, *J. Am. Ceram. Soc.* **1996**, *79*, 507.
[12] J. Lu, M. Prabhu, J. Song, C. Li, J. Xu, K. I. Ueda, H. Yagi, T. Yanagitani, A. A. Kaminskii, *Jpn. J. Appl. Phys., Part 2* **2001**, *40*, L552.
[13] J. Marchal, J. Tyrone, R. Baranwal, T. Hinklin, R. M. Laine, *Chem. Mater.* **2004**, *16*, 822.
[14] J. M. Saniger, *Mater. Lett.* **1995**, *22*, 109.
[15] P. Tarte, *Spectrochim. Acta, Part A* **1967**, *23*, 2127.
[16] R. S. Hay, *J. Am. Ceram. Soc.* **1994**, *77*, 1473.

Prefluorescent-Dye-Induced, Chemically Reversible Fluorescent Imaging Based on a Polymeric Photobase Generator

By *Won San Choi*, *Yong-Young Noh*, and *Kyu Ho Chae**

In recent years, the formation of fluorescent images in thin polymer films has attracted considerable interest due to their possible application in the areas of optical data storage[1] and displays.[2] Fluorescence imaging has been used with fluorescence probes to study photoacid generation efficiencies and acid diffusion in microlithography[3–6] and for mapping photogenerated radicals in thin polymer films.[7]

A number of methods for the formation of fluorescent images have been reported, including photoacid-induced protonation,[8,9] acid-catalyzed chemical amplification,[10–13] and the use of a prefluorescent radical probe.[7] Most of these methods are based on photogenerated acids. Such generation of fluorescent images consists of a two-step process. The first step is the selective removal of acid-labile protecting groups by way of photochemical transformation, and the second involves the chemisorption of a fluorescent organic dye from a solution into the patterned polymer film.

Similar to fluorescent-image formation based on photogenerated acids, fluorescence imaging based on a photogenerated base is also possible.[14] Photobase generators, analogously to photoacid generators, produce an amine upon irradiation and are being increasingly used in the development of new technologies. For example, they have been applied to the photolithographic micropatterning of electroluminescent polymers[15] and patterning of conductive polyaniline films,[16] as well as various types of photoresists.

Several fluorescent dyes that react with amino groups are known. Since most of these fluorescent dyes are intrinsically fluorescent, the unreacted dye must be removed by washing in the second stage of image development. Among the fluorescent dyes for amino groups, fluorescamine[17] attracted our attention because while fluorescamine intrinsically has no fluorescence, it becomes fluorescent through reaction with amino groups, as shown in Scheme 1. Fluorescamine has been

[*] Prof. K. H. Chae, W. S. Choi
Department of Applied Chemistry
Chonnam National University
300 Yongbong-dong, Buk-gu
Gwangju, Chonnam 500-757 (Korea)
E-mail: khochae@chonnam.ac.kr
Y.-Y. Noh
Center for Frontier Materials
Department of Materials Science and Engineering
Gwangju Institute of Science and Technology (GIST)
1 Oryong-Dong, Buk-gu
Gwangju 500-712 (Korea)

DOI: 10.1002/adma.200400841

Nano-α-Al_2O_3 by liquid-feed flame spray pyrolysis

R. M. LAINE*, J. C. MARCHAL, H. P. SUN AND X. Q. PAN

Department of Materials Science and Engineering, University of Michigan, Ann Arbor, Michigan 48109-2136, USA

*e-mail: talsdad@umich.edu

Published online: 6 August 2006; doi:10.1038/nmat1711

Nanometre-sized particles of transition (t)-aluminas are important for the fabrication of high-quality alumina ceramics. Multiple tons are produced each year using a variety of gas-phase processes[1–4]. The nanoparticles produced by these methods consist mainly of the undesired δ phase with some γ- and θ-Al_2O_3. Nano-t-aluminas should provide access to dense nano/submicrometre-grained α-Al_2O_3 shapes offering significant advantages over micrometre-grained shapes[5–11]. Unfortunately, polymorphism coupled with the high activation energy for nucleating α-Al_2O_3 greatly impedes efforts to process dense α-Al_2O_3 with controlled grain sizes, especially for submicrometre materials. Typically α-Al_2O_3 nucleation within t-aluminas is sporadic rather than uniform, leading to exaggerated grain growth and vermicular microstructures without full densification[5]. Thus, production of quantities of nano-α-Al_2O_3 from multiple nano-t-aluminas for seeding or direct processing of α-Al_2O_3 monoliths could greatly change how α-Al_2O_3 components are processed. We report here that liquid-feed flame spray pyrolysis[3] of nano-t-aluminas converts them to dispersible 30–80 nm α-Al_2O_3 powders (50–85% phase transformed). Surprisingly, the powder surfaces are fully dehydrated. These powders pressureless sinter to more than 99.5% dense α-Al_2O_3 with final grain sizes $\leq$500 nm without sintering aids.

From a commercial perspective, there is considerable impetus to develop an economical source of sub-100-nm average particle size (APS) α-Al_2O_3 for applications ranging from tough prosthetic implants, to transparent armour, transparent rather than translucent sodium vapour lamp envelopes, and possibly polycrystalline lasers, as well as more common applications[5–11]. Despite this considerable potential, there are no commercial sources of sub-100-nm α-Al_2O_3.

From an academic perspective, there is considerable speculation in the literature as to why it is apparently impossible to make polycrystalline nano-α-Al_2O_3 monoliths, let alone free-flowing nanopowders of α-Al_2O_3 (refs 12–16). On the basis of studies of high-surface-area polycrystalline t- and α-alumina, the literature suggests that it may be difficult to generate α-Al_2O_3 nuclei under conditions where complete conversion of t-aluminas to the alpha phase will occur without extensive grain growth. More problematic, the vermicular microstructures caused by this phase change inhibit any further densification of these materials. Studies by McHale *et al.* suggest that polycrystalline nano-α-Al_2O_3 is not stable with respect to polycrystalline nano-γ-Al_2O_3 at surface areas of $\approx$125 $m^2 g^{-1}$, equivalent to grain sizes of $\approx$8 nm (ref. 16). One possible explanation is that hydrated, nanostructured polycrystalline γ-Al_2O_3 might be more stable than similarly hydrated α-Al_2O_3; however, the studies by McHale *et al.* seem to rule this out[16]. It should be noted that a brief report by Krell *et al.* describes the preparation of nano-α-Al_2O_3 by templating crystallization of amorphous aluminium-*s*-butoxide and aluminium nitrate with diaspore[17]. This work highlights the difficulties in obtaining homogenous green bodies from nanopowders.

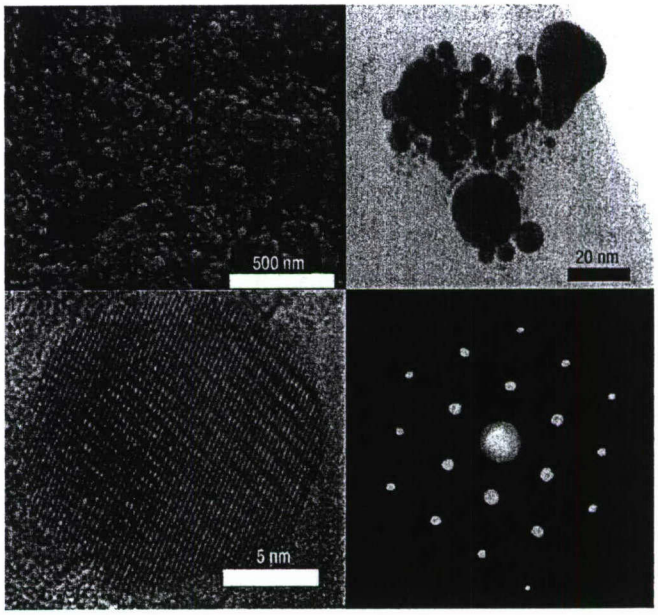

Figure 1 Electron microscopy of nano-α-Al_2O_3. From top left to bottom right: scanning electron micrograph, transmission electron micrograph, high-resolution transmission electron micrograph and electron diffraction pattern of a single particle showing hexagonal symmetry. See also Supplementary Information, Fig. S2 for additional transmission electron micrographs.

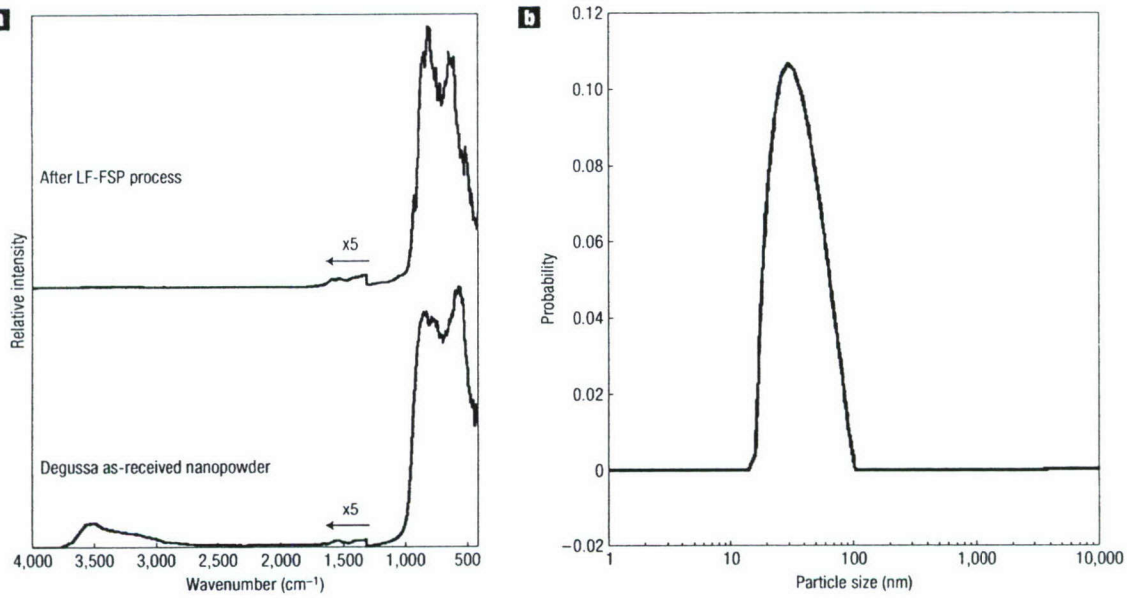

Figure 2 Analysis of Degussa nano-*t*-alumina. a, Fourier-transform infrared spectra before and after LF-FSP. The arrows indicate that everything below and to the left are multiplied by 5. **b**, Dynamic light scattering particle size distribution after LF-FSP processing.

Table 1 Rietveld-refined phase composition of nano-Al_2O_3 before/after LF-FSP.

	As-received/as-processed powders			
PDF No./Size	LF-FSP	Degussa	Gibbsite†	Nanophase
δ: 46-1131	32	63	0	0
δ*: 46-1215	48	6	0	0
δ^c: 01-77-3965	0	0	0	68
γ: 29-0063	8	31	0	32
α: 71-1124	5	0	0	0
S†: 70-2038	0	0	100	0
θ: 23-1009	7	0	0	0
Particle size‡ (nm)	15	11	>100	35
	After LF-FSP processing			
α: 71-1124	86	77	54	77
θ: 23-1009	14	23	46	23
Particle size‡ (nm)	29	36	88	36

† Spacerite (gibbsite).

‡ The APSs reported here are based on Rietveld refinement but are consistent with BET-determined particle sizes. The error is ±3%.

Previous studies on liquid-feed flame spray pyrolysis (LF-FSP) (detailed elsewhere[3]) indicate that, because it offers access to kinetic products, it has the potential to produce novel phases as well as to expand known phase fields[18,19]. Our initial objective was to coat nano-alumina powders with other oxides; however in the process we discovered that LF-FSP provides a simple and general method of transforming ethanol dispersions of a wide variety of commercial t-Al_2O_3 nanopowders produced primarily by gas phase to α-Al_2O_3 nanopowders without also causing aggregation (see Table 1; Supplementary Information, Fig. S1 shows X-ray diffraction, XRD, patterns). The process is not yet optimized but the results are already promising.

In our process, as-received (as-processed[3]) 1–10 wt% nano-t-alumina powders are milled with alumina media in ethanol for 24 h, then ultrasonicated for 30 min with a 500 W titanium horn. This dispersion is aerosolized with O_2, using previously described techniques[3], and combusted at temperatures near 1,600 °C. The resultant powders, produced at 100 g h^{-1}, are collected 1 m downstream in electrostatic precipitators. The as-collected powders exhibit XRD powder patterns (see Table 1 and Supplementary Information, Fig. S1) that indicate a high degree of conversion to mixtures of θ- and α-Al_2O_3, with the gibbsite-derived powders having the lowest conversions at roughly 50% and the LF-FSP, Nanophase and Degussa δ-Al_2O_3 nanopowders having conversions at 80–85%. The initial presence of θ- and traces of α-Al_2O_3 in the LF-FSP t-alumina may explain the higher α conversion for these powders, and also suggests that complete transformation may be accessible in one step under different process conditions. Hence this approach seems to be general and simple.

Electron microscopy of representative samples, Fig. 1, demonstrates the uniformity of the as-produced α-Al_2O_3 with no particles greater than 150 nm for the gibbsite-derived powders and none greater than 100 nm for the other powders. High-resolution transmission electron microscopy and digital diffraction show a 15 nm α-Al_2O_3 particle. Typical surface areas for finer powders are 40–60 m^2 g^{-1}.

Unlike the starting nano-transition aluminas, which have highly hydrated surfaces, the resulting α-Al_2O_3 particle surfaces are nearly devoid of hydroxyl groups, see Fig. 2.

To our knowledge there are no precedents for converting t-aluminas to dispersible sub-100-nm α-Al_2O_3 powders. Thus, the actual conversion mechanism here can only be conjecture. It may be that although hydration energetics are not an issue in determining the relative stability of polycrystalline, high-surface-area α- versus γ-Al_2O_3 (ref. 14), it is an issue here, in an environment where grain-boundary interactions are non-existent. This seems to be a reasonable argument given that the LF-FSP process generates enormous amounts of H_2O and CO_2, at high temperatures, yet the recovered powders have essentially no hydroxyl groups.

One of the difficulties in processing the resulting powder is that, contrary to regular LF-FSP transition alumina (which disperses

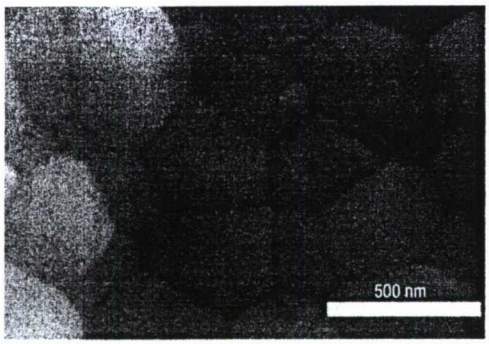

Figure 3 Scanning electron micrograph of a fractured surface of sintered pellets (after additional thermal etching).

spontaneously in ethanol)[3], surfactants are essential to dispersing these powders. Bicine (2–3 wt%) was most efficient[20], allowing homogenous drying of the dispersions and further processing into green bodies.

To confirm the APS of the resulting nano-α-Al_2O_3, bicine dispersions of the twice LF-FSP processed powders were examined by dynamic laser light scattering (Fig. 2b) giving APS of 30–40 nm indicating that the powders are mostly single crystals. This is in keeping with APS values obtained from XRD line broadening and the Brunauer–Emmett–Teller (BET) data in Table 1.

Although the resulting α-Al_2O_3 nanopowders are not 100% phase pure in these proof-of-principle studies, the residual θ-Al_2O_3 is expected to convert without vermicular growth due to the high number of α-nuclei as shown in work with Taimicron powders[21]. Preliminary work was then done to assess the sintering behaviour and sintering mechanisms, exponents and activation energies of the 86% α-Al_2O_3 nanopowders as will be discussed in greater detail in a later paper.

The 86% α-Al_2O_3 powder previously dispersed with bicine was uniaxially (45 MPa) and then cold isostatically pressed (200 MPa) to give green densities of $63 \pm 2\%$. Following binder burnout (5 °C min^{-1} to 800 °C with a 2 h hold; air) and two-step pressureless sintering (10 °C min^{-1} to 1,425 °C with a 2 h hold, then decreasing to 1,350 °C with a 5 h hold in vacuum), the resulting bodies are more than 99.5% dense (geometrical) with average grain sizes of $\leq$500 nm (see Fig. 3).

No efforts were made to optimize this process, yet the densities and grain sizes obtained are comparable to previous work on the sintering behaviour of ultrafine α-Al_2O_3 (with MgO, with or without hot isostatic pressing)[14,21]. In particular, efforts to obtain more-homogeneous green bodies are under investigation as advanced processing methods[17,22] are needed to obtain fully dense materials.

Using the Perez–Maqueda approach[23] to interpret the first step of sintering, we obtained a sintering exponent of $n = 2.0$ and an activation energy for sintering, E_a, of 85 ± 5 kJ mol^{-1}. This sintering exponent is expected for the sintering of unaggregated faceted particles.

METHODS

PRECURSOR MATERIALS AND NANOPOWDERS

The majority of nanopowders were received as gifts from the respective companies or were generated, as described previously[3].

XRD STUDIES

All samples were characterized as described previously[3]. Jade (Version 7 from Materials Data) was used to identify crystallographic phases, APSs and relative phase compositions.

HIGH-RESOLUTION TRANSMISSION ELECTRON MICROSCOPY

Micrographs were taken on a JEOL 3011 using methods described elsewhere[3].

DIFFUSE-REFLECTANCE FOURIER-TRANSFORM INFRARED SPECTRA

Diffuse-reflectance Fourier-transform infrared spectra, specific surface analyses (BET) and scanning electron microscopy data were recorded as described elsewhere[3].

Received 6 May 2005; accepted 29 June 2006; published 6 August 2006.

References

1. Swihart, M. T. Vapor-phase synthesis of nanoparticles. *Curr. Opin. Colloid Interface Sci.* **8,** 127–133 (2003).
2. Gutsch, A. *et al.* Gas phase production of nanoparticles. *Kona* **20,** 24–37 (2002).
3. Hinklin, T. *et al.* Liquid-feed flame spray pyrolytic synthesis of nanoalumina powders. *Chem. Mater.* **16,** 21–30 (2004).
4. Johnston, G. P., Muenchhausen, R., Smith, D. W., Fahrenholtz, W. & Foltyn, S. Reactive laser ablation synthesis of nanosize alumina powder. *J. Am. Ceram. Soc.* **75,** 3293–3298 (1992).
5. Yarbrough, W. A. & Roy, R. Microstructural evolution in sintering of AlOOH gels. *J. Mater. Res.* **2,** 494–515 (1987).
6. Parimal, J. P. *et al.* in *Inorganic Optical Materials II* (eds Marker, A. J. & Arthurs, E. G.) 1–14 (Proc. SPIE, Vol 4102, SPIE Optical Engineering Press, Bellingham, Washington, 2000).
7. Fischman, G. Validated microstructural assessment of femoral heads. *J. ASTM Int.* **1,** 1–14 (2004).
8. Saikko, V. & Keränen, J. Wear simulation of alumina-on-alumina prosthetic hip joints using a multidirectional motion pin-on-disk device. *J. Am. Ceram. Soc.* **85,** 2785–2791 (2002).
9. D'Antonio, J., Capello, W., Manley, M. & Bierbaum, B. New experience with alumina-on-alumina ceramic bearings for total hip arthroplasty. *J. Arthroplasty* **17,** 390–398 (2002).
10. Krell, A. *et al.* Transparent sintered corundum with high hardness and strength. *J. Am. Ceram. Soc.* **86,** 12–18 (2003).
11. Apetz, R. & van Bruggen, M. P. B. Transparent alumina; a light scattering model. *J. Am. Ceram. Soc.* **86,** 480–486 (2003).
12. Bagwell, R. B., Messing, G. L. & Howell, P. R. The formation of alpha-Al_2O_3 from theta-Al_2O_3: The relevance of a "critical size" and: Diffusional nucleation or 'syncro-shear'? *J. Mater. Sci.* **36,** 1833–1841 (2001).
13. Wen, H.-L. & Yen, F.-S. Growth characteristics of boehmite-derived ultrafine theta and alpha-alumina particles during phase transformation. *J. Cryst. Growth* **208,** 696–708 (2000).
14. Echeberria, J., Tarazona, J., He, J. Y., Butler, T. & Castro, F. Sinter-HIP of α-alumina powders with sub-micron grain sizes. *J. Eur. Ceram. Soc.* **22,** 1801–1809 (2002).
15. Hale, J. M., Aurox, A., Perotta, A. J. & Navrotsky, A. Surface energies and thermodynamic phase stability in nanocrystalline aluminas. *Science* **277,** 788–791 (1997).
16. McHale, J. M., Navrotsky, A. & Perrotta, A. J. Surface energies and thermodynamic phase stability in nanocrystalline aluminas. *J. Phys. Chem. B* **101,** 603–613 (1997).
17. Hongwei, M. & Krell, A. Synthesis and processing of nano-alpha-Al_2O_3 powders. *Key Eng. Mater.* **200,** 43–46 (2002).
18. Azurdia, J. A. *et al.* Liquid-feed flame spray pyrolysis as a method of producing mixed-metal oxide nanopowders of potential interest as catalytic materials. Nanopowders along the NiO-Al_2O_3 tie line including $(NiO)_{0.22}(Al_2O_3)_{0.78}$, a new inverse spinel composition. *Chem. Mater.* **18,** 731–739 (2006).
19. Laine, R. M., Marchal, J., Sun, H. P. & Pan, X. P. A new $Y_3Al_5O_{12}$ phase produced by liquid-feed flame spray pyrolysis (LF-FSP). *Adv. Mater.* **17,** 830–833 (2005).
20. Kimel, R. A. & Adair, J. H. Aqueous synthesis at 200 °C of sub-10 nanometer yttria tetragonally stabilized zirconia using a metal-ligand approach. *J. Am. Ceram. Soc.* **88,** 1133–1138 (2005).
21. Godlinski, D., Kuntz, M. & Grathwohl, G. Transparent alumina with submicrometer grains by float packing and sintering. *J. Am. Ceram. Soc.* **85,** 2449–2456 (2002).
22. Bowen, P., Carry, C., Luxembourg, D. & Hofmann, H. Colloidal processing and sintering of nanosized transition alumina. *Powder Technol.* (in the press).
23. Perez-Maqueda, L. A., Criado, J. M. & Real, C. Kinetics of the initial stage of sintering from shrinkage data: Simultaneous determination of activation energy and kinetic model from a single nonisothermal experiment. *J. Am. Ceram. Soc.* **85,** 763–768 (2002).

Acknowledgements

This work was supported by the Air Force Office of Scientific Research on Contract F49620-03-1-0389. We thank G. Varga of Degussa and R. Brotzman of Nanophase for providing samples of nano-*t*-aluminas and M. Solomon and M. Kogan for help with the dynamic light scattering experiments.

Correspondence and requests for materials should be addressed to R.M.L.

Supplementary Information accompanies this paper on www.nature.com/naturematerials.

Author contributions

J.C.M. and R.M.L. were responsible for the experimental work, planning and the majority of the data analysis. X.P. and H.P. were responsible for the design and execution of weeks of extensive transmission electron microscopy work.

Competing financial interests

The authors declare that they have no competing financial interests.

Combinatorial Synthesis of Metastable Phases in the Magnesium Spinel □ Alumina System

Journal:	*Chemistry of Materials*
Manuscript ID:	draft
Manuscript Type:	Article
Date Submitted by the Author:	n/a
Complete List of Authors:	Hinklin, Thomas; University of Michigan, Materials Science and Engineering Laine, Richard; University of Michigan, Dept. of MSE
Subject Headings:	Precursor Routes to Materials (including Polymer-Derived Ceramics), Nanomaterials (Nanoparticles, Nanotubes, etc.), Inorganic Solids and Ceramics

Combinatorial Synthesis of Metastable Phases in the Magnesium Spinel – Alumina System

T. R. Hinklin and R. M. Laine
Contribution from the Department of Materials Science and Engineering,
University of Michigan, Ann Arbor, MI 48109-2136

Abstract

We report here the use of liquid-feed flame spray pyrolysis (LF-FSP) to produce fourteen nanopowders along the Al_2O_3-$MgAl_2O_4$ tie line by combusting varied ratio aerosolized ethanol solutions of alumatrane [$Al(OCH_2CH_2)_3N$] and magnesium acetylacetonate [$Mg(C_5H_7O_2)_2$]. The resulting nanopowders were characterized by X-ray fluorescence, N_2 adsorption (BET), scanning electron microscopy (SEM), X-ray diffraction (XRD), and infrared spectroscopy (FTIR). The powders typically consist of single-crystal particles < 30 nm diameter and specific surface areas (SSAs) of 30-80 m^2/g. Complementary XRD and FTIR studies show a gradual change in powder patterns and spectra from δ-Al_2O_3 to $MgAl_2O_4$. Intermediate compositions exhibit phases which fall well outside of the established phase diagram and provide insight into the structure of transition aluminas. These materials have been shown to exhibit novel photonic behavior and have potential value as a new catalyst or support.

Introduction

The spinel-alumina binary phase system includes materials used for many important industrial applications including catalyst supports, refractories, abrasives, transparent, high strength and radiation tolerant ceramics.[1-7] The ability to combinatorially generate ultrafine or nanosized powders of controlled chemical and phase composition along the $(MgO)_x(Al_2O_3)_{1-x}$ tieline offers the opportunity to tune the desired properties for these current applications. Furthermore, nanosized powders may offer novel properties in their own right in addition to easier processing for all applications.

Liquid feed flame spray pyrolysis (LF-FSP) is a highly flexible tool that allows development of nanosized, non-porous, unaggregated, mixed-metal oxides of controlled composition.[8-12] LF-FSP offers access to known phases as well as difficult, or impossible to access phases and phase compositions.[13,14] Based on the flexibility of LF-FSP, we report here combinatorial tailoring along the $MgAl_2O_4$-Al_2O_3 tie line as a means to access nanopowders with complete control of chemical composition. These materials, especially those with unusual phases or phase compositions, may offer properties hitherto unknown for this extremely well-studied system.

We are particularly interested in developing these materials to create transparent fine-grained monoliths for applications ranging from transparent armor to polycrystalline lasers and IR transparent radomes.[4,7,15] In this context, one aspect of the work reported here is to produce and characterize nanopowders with low MgO concentrations (0.1-2 mol%) to investigate their utility as homogenously doped nano-transitional aluminas for sintering to fully dense, fine grained α-alumina monoliths, as recently described.[16] In addition, nano-alumina powders with MgO con-

centrations of 1-10 mol% are being investigated for novel UV emission based on defects associated with Mg^{2+} in the tetragonal alumina structure, as reported elsewhere.[17]

We have previously reported the LF-FSP production of stoichiometric nano-$MgAl_2O_4$ spinel and pure ∂-Al_20_3.[8,9] In addition to this study, similar binary compositional studies in the Ni, Co, Zn, and Cu aluminate systems were undertaken and recently published.[14,18,19] These studies provide the basis for developing ternary, quaternary or greater compositions for advanced photonic and catalyst applications. In this paper, we continue our efforts to develop materials of potential interest in these scientific domains. This study explores and characterizes the Al_2O_3-$MgAl_2O_4$ phase field created through LF-FSP of simple metalloorganic precursors suitable for industrial scale production.[8-14]

Experimental

MATERIALS

Magnesium acetylacetonate $Mg(Acac)_2$ [$Mg(C_5H_7O_2)_2$ 98+%], triethanolamine [$N(CH_2CH_2OH)_3$ 98%], Tetrahydrofuran THF [C_4H_8O 99+% stabilized] and anhydrous ethanol [CH_3CH_2OH, 99$^+$%] were purchased from Alfa Aesar and used as received. Aluminum tri-(sec-butoxide), [$Al(OsBu)_3$, 97%] was purchased from Chattem Chemical Co. and used as received.

PRECURSOR FORMULATIONS

Alumatrane $Al[N(CH_2CH_2O)_3]$ was synthesized from $Al(OsBu)_3$ and $N(CH_2CH_2OH)_3$ as described elsewhere [8] then diluted with ethanol such that the ceramic yield was 7.5 wt.% by TGA. The magnesium precursor, was prepared by dissolving the $Mg(Acac)_2$ in 50:50 THF:EtOH while stirring for 24 h. This solution was filtered through No. 40 filter paper *(Whatman)* to remove the $\approx$ 0.5 wt% of residual solids. The resulting solution was characterized by TGA for MgO content, typically 3-4 wt %. Volumetric measurements were used to mix both the MgO and Al_2O_3 solutions with the desired stoichiometric amounts such that the final concentration of ceramic (Al_2O_3 + MgO) in solution was 2 wt% and THF:EtOH ratio was 50:50.

LIQUID-FEED FLAME SPRAY PYROLYSIS

Precursor formulations are atomized at 50 mL/min in an ultrasonic oxygen atomizer to generate an oxygen rich aerosol which is ignited via methane/oxygen pilot torches in the device's ignition chamber. Combustion occurs at temperatures up to 2000°C producing nanopowder and gaseous byproducts. A steep temperature gradient, >500°C/sec, between the combustion chamber and the 300°C collection point provides rapid quenching of the powder after combustion, as the powders are carried away from the combustion area by the natural flow of gases aided by a high velocity (>700 cfm) inline blower. The powders are collected downstream in a pair of 6' x

3" wire in tube electrostatic precipitators (ESP) maintained at a 10 kV pseudo DC potential. After the run is complete, powders are recovered from the ESP tubes and stored in plastic bags. Other descriptions of this technique have been published elsewhere.[8]

X-RAY DIFFRACTION

The phases and crystallite sizes of as-prepared samples were characterized by XRD, using a Rigaku Rotating Anode Goniometer (Rigaku Denki Co. Ltd., Tokyo, Japan), Powder samples for the Rigaku diffractometer were prepared by pressing ≈ 100 mg in amorphous silica slides) for data collection. Cu Kα (λ = 1.54 Å) radiation with a Ni filter was used with a working voltage and current of 40 kV and 100 mA, respectively. Scans were continuous from 10–80° 2θ with a step scan of 2° 2θ/min and increments of 0.05° 2θ. Scan data was processed using Jade software version 7.0 (Materials Data, Inc, Livermore, CA). The processing included phase determination, crystallite size and unit cell dimensions.

DIFFUSE REFLECTANCE INFRARED FOURIER TRANSFORM SPECTROSCOPY (DRIFTS).

DRIFT spectra were recorded on a Mattson Galaxy Series FTIR 3000 spectrometer (Mattson Instruments, Inc., Madison, WI). Optical grade, random cuttings of KBr (International Crystal Laboratories, Garfield, NJ) were ground using an alumina mortar and pestle, with 1.0 wt% of the sample to be analyzed and packed firmly in the sample holder, leveled off at the upper edge to provide a smooth surface. Samples were transferred to the FTIR sample chamber, which was flushed continuously with N_2. Each spectrum is continuous in the range 4000-400 cm^{-1} with a scan resolution of 4 cm^{-1} with an average of 128 scans.

SPECIFIC SURFACE AREA ANALYSIS.

Specific surface areas (SSA) were obtained using a Micromeritics ASAP 2010 sorption analyzer (Norcross, GA). Samples (200 mg) were degassed at 400°C for 2 h or until the degas rate

was less than 0.005 Torr. Analysis was conducted at –196°C (77K) with nitrogen as the adsorbate gas. The SSAs were determined by the BET multipoint method using at least five data points with relative pressures of 0.001-0.20. The particles average size was derived from the formula:

$$< R >= \frac{3}{\rho \times ssa}$$

SCANNING ELECTRON MICROSCOPY (SEM).

A field emission SEM (Model XL-30, Phillips, Germany) was used to image powder morphologies. Powder samples were prepared by dispersing the powder (0.1 g) in distilled water (10 ml). A drop of the suspension was placed on a polished Al stub and allowed to dry. The dried powder films were spark coated with a thin film of carbon to reduce charging effects. An operating voltage of 30.0 kV was used with a spot size of 3.

X-RAY FLUORESCENCE

Samples were prepared by mixing 0.50g of sample into 10.0g of $Li_2B_4O_7$ glass flux. The sample and glass flux were mechanically stirred for 5 minutes in a methacrylate vial with three methacrylate balls using a SPEX 6000 ball mill. The mixtures were fused into glass beads by placing them in an oven held at 1000°C for 10 min. The samples were analyzed using a Panalytical PW2400 X-Ray Fluorescence spectrometer (formerly Philips), equipped with a WDS detection system (wavelength dispersive).

Results and discussion

We report here the synthesis and characterization of a series of samples that lie along the $MgAl_2O_4$-Al_2O_3 tie line. These nanopowder materials were produced in a single-step process, bypassing the more labor-intensive and costly routes, typically used to synthesize such materials. We have previously demonstrated LF-FSP processing provides compositions that are otherwise hard or impossible to attain.[13-18] Here we continue a series of studies demonstrating that LF-FSP is a highly effective process for developing metastable materials with the spinel crystal structure that lie well outside the thermodynamic phase field. In addition, as-produced low MgO concentration and stoichiometric spinel nanopowders, with effective ceramic processing, can be sintered to high densities with retained fine microstructures, as will be reported elsewhere.

All samples exhibit relatively high surface areas, Table **1**, have no microporosity and exhibit faceted-spherical morphology. These features also combine controlled stoichiometry with a high degree of crystallinity making them excellent candidates for catalytic and photonic applications. Because there are no micropores present, and their very high thermal stability[14] suggest that these materials will likely retain their catalytic properties even after being exposed to high temperature or pressure environments. When doped with the appropriate ions, the high degree of crystallinity in these materials should offer ideal emission behavior without the need to anneal or calcine as is typically required for phosphors made by alternative routes.[17,20]

In the following sections, we discuss the formulation of precursors and nanopowder production. We then discuss the series of produced nanopowders in terms of crystalline phases present, their specific surface areas, the dominant metal-oxygen coordination and morphology. A study of the thermal properties gives insight into the stability of the phases present.

Precursor formulations

A set of fourteen precursor formulations, Table **1**, was prepared by mixing precise amounts of alumatrane, $Al[N(CH_2CH_2O)_3]$, and magnesium, $Mg(Acac)_2$, precursors. The solutions were diluted with THF:EtOH and mechanically stirred for 1 h prior to powder synthesis. All solutions were formulated to contain 2 wt% ceramic yield in order to minimize complications with LF-FSP process, such as solubility differences and to ensure a constant flux density of metal oxide species in the flame.

Table 1: $MgO\text{-}Al_2O_3$ compositions as target mol% MgO compared to XRF values of produced by LF-FSP, with their average particle sizes by SSA and XRD line broadening.

Mol % MgO	**0**	**0.1**	**0.2**	**0.5**	**1**	**2.5**	**5**	**6.06**	**7.17**	**10**	**20**	**30**	**40**	**50**
SSA (nm)	25	23	26	24	24	28	31	28	28	26	29	26	29	32
XRD (nm)	11	10	11	12	12	16	16	17	17	20	26	23	21	28
XRF mol%	0	0.06	0.22	0.49	1.03	2.44	4.74	5.91	7.09	10.1	20.5	29.6	40.2	49.8

Powder characterization.

The compositions reported here are the targeted compositions. Based upon the calibration curve established, using the WDXRF values, the targeted and measured compositions are within the assumed error of ±2%, Table **1**.

The average particle sizes (APSs) calculated from specific surface area analyses (SSAs) of all the as-produced samples are shown in Table **1**. The APS is roughly constant with increasing MgO content to stoichiometric $MgAl_2O_4$. The difference in density between stoichiometric spinel (3.6 g/cc) and pure δ-alumina (3.6 g/cc) is negligible and is assumed to not vary significantly with the incorporation of the Mg ions into the $Mg_xAl_{2-x}O_4$ matrix. No microporosity was expected or detected in any sample.

The average particle sizes (APSs) values obtained by Debye-Scherer XRD line-broadening analyses are shown in Table **1**. APS values obtained by XRD increase with increasing MgO content. This is likely due to the presence of additional phases at low MgO contents (Figure **3**) and the documented small domain structure of the transition aluminas.[28] The APS of all powders is >30 nm regardless of technique used to calculate the values.

Scanning electron microscopy

SEMs of all samples were taken in order to study particle morphology. Figure **1** shows micrographs of the 0 mol% MgO:Al_2O_3, 0.5 mol% MgO:Al_2O_3, 2.5 mol% MgO:Al_2O_3, 5 mol% MgO:Al_2O_3, 30 mol% MgO:Al_2O_3, and 50 mol% MgO:Al_2O_3 samples, which are representative of all other samples. The powders exhibit homogenous spherical morphologies, also evident is the narrow particle size distribution. The APSs of the particles is clearly > 60 nm, agreeing with the results obtained by BET and XRD. The amount of coalesced secondary particles increases with increasing MgO content likely due to the change in LF-FSP conditions as the high viscosity alumatrane is replaced by the subliming $Mg(acac)_2$. The exact impact on combustion parameters and conditions are unknown. This is still consistent with XRD and SSA results since both analysis methods are insensitive to the presence of a small portion of larger particles.

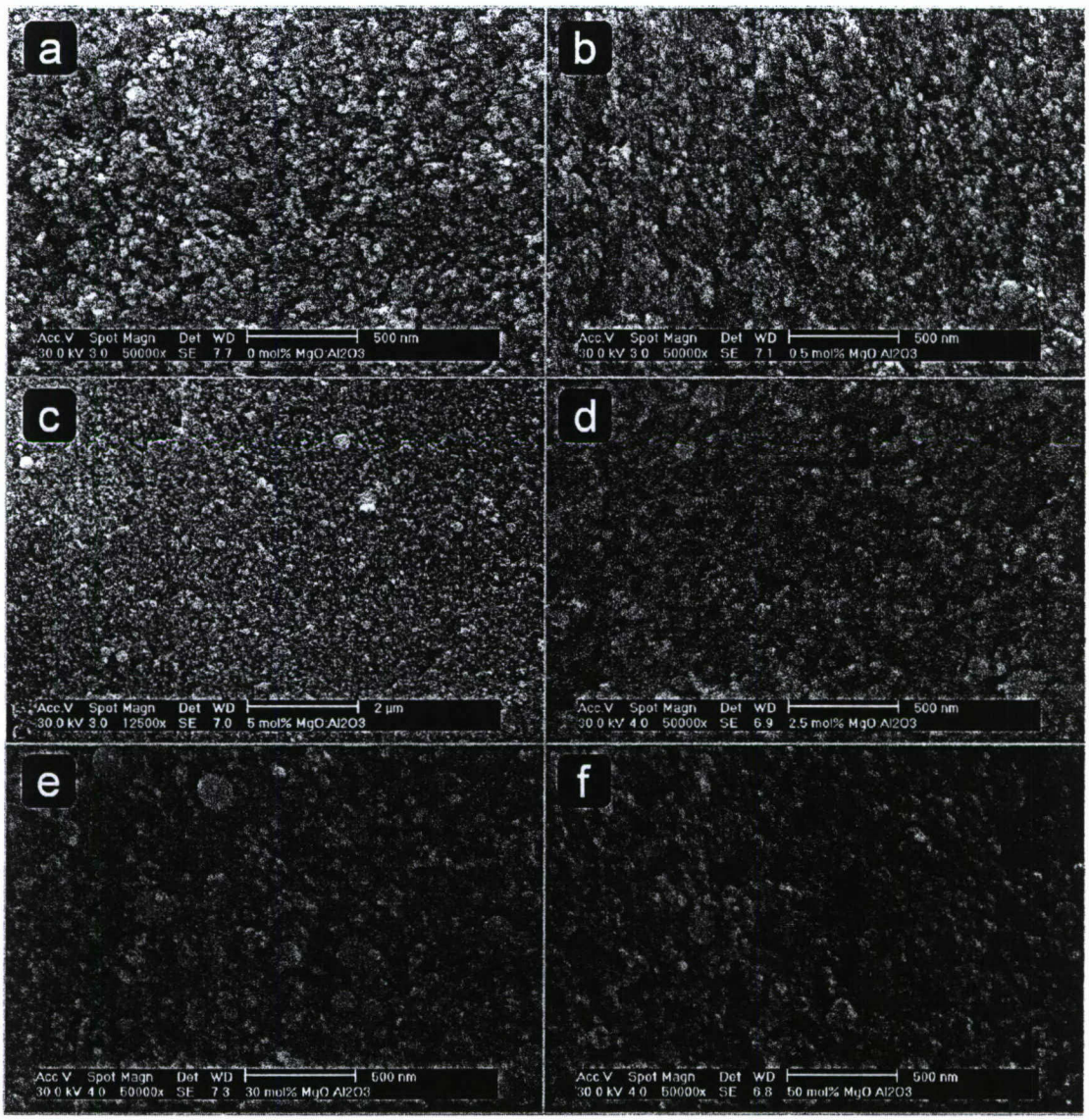

Figure 1: SEM images of as-produced $MgO:Al_2O_3$ powders: (a) 0 mol% $MgO:Al_2O_3$, (b) 0.5 mol% $MgO:Al_2O_3$, (c) 2.5 mol% $MgO:Al_2O_3$, (d) 5 mol% $MgO:Al_2O_3$, (e) 30 mol% $MgO:Al_2O_3$, (f) 50 mol% $MgO:Al_2O_3$.

X-ray powder diffraction patterns (XRD)

XRD of selected compositions in $MgAl_2O_4$-Al_2O_3 phase field are given in Figure **2**. The relevant ICDD cards are ($MgAl_2O_4$:73-1959, $MgAl_{26}O_{40}$: 20-0660, ∂^t-Al_2O_3:16-394, ∂^o-Al_2O_3:46-1131, and ∂*-Al_2O_3:46-1215 and θ-Al_2O_3:23-1009). A gradual change in the XRD patterns is observed from pure alumina (Al_2O_3) through the stoichiometric magnesium spinel

$MgAl_2O_4$). Figure **3** graphs the percent of each phase present in the as-produced LF-FSP powders. Figure **4** uses cell refinement calculations (see experimental) based on the peak positions of the six strongest lines of the dominant phase to plot the lattice parameters of the *dominant* phase verses composition.

The pure Al_2O_3 samples made by LF-FSP are a mixture of four transitional alumina phases; ∂^t, ∂^o, ∂^* and θ. A more detailed analysis of these phases can be found elsewhere.[9] The amount of the non-tetragonal transitional phases decreases with increasing MgO content. The addition of MgO stabilizes the ∂^t-Al_2O_3 phase because the Mg ions preferentially substitute for tetrahedrally coordinated Al^{3+} in the ∂^o-Al_2O_3 lattice. The ∂^t-Al_2O_3 phase is isostructural with the $MgAl_{26}O_{40}$ phase previously identified by Lejus[21] having a slightly larger unit cell due to the incorporation of the relatively large Mg-O tetrahedral and octahedral species.

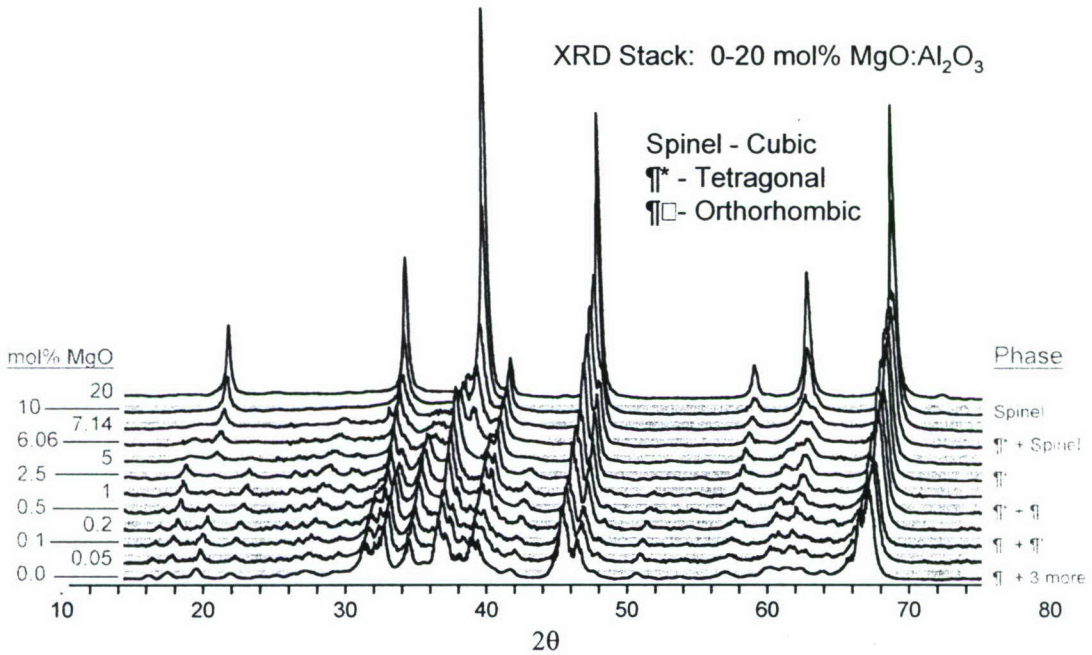

Figure 2: XRD powder patterns for $(MgO)_x(Al_2O_3)_{1-x}$ for x = 0-20 mol %.

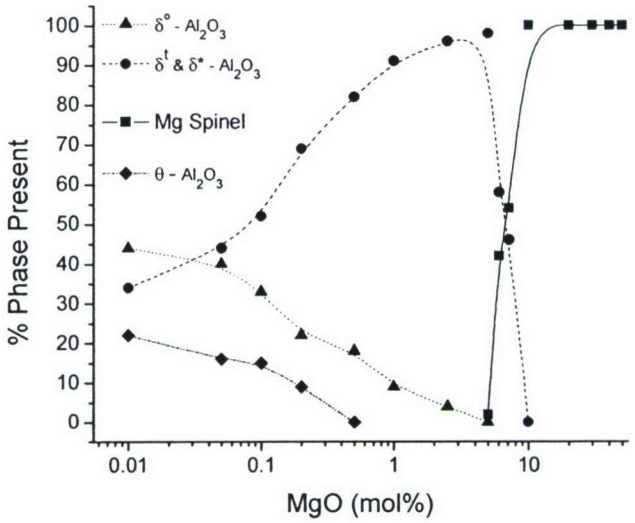

Figure 3: Dominant phase vs. mol % MgO from calculations using Figure 2 data.

The stoichiometric magnesium aluminate ($MgAl_2O_4$) shows the expected phase pure spinel pattern and the cubic spinel phase is preserved down to 10 mol% MgO. Samples with 7.17, 6.06 and 5 mol% MgO content begin to show peaks corresponding to $MgAl_{26}O_{40}$ (∂^t) phase with $MgAl_2O_4$ content decreasing with decreasing MgO content, until only the tetragonal phase is observed below 5 mol%. The thermodynamic phase diagram[22] depicts a wide spinel solid solution to arise at high temperatures (1400-2000°C), extending down to ≈10 mol% MgO at the eutcitc while at STP the spinel solid solution is limited to 48-50 mol% MgO.

To our knowledge there are no reports in the literature suggesting that the spinel structure along the $MgAl_2O_4$-Al_2O_3 tie-line remains stable to such low MgO contents. However, a thermodynamic revision of the MgO-Al_2O_3 diagram conducted by Hallstedt[22] suggests that the Al_2O_3 solvus extends to 11.4 mol% MgO at 2267K. According to Hallstedt's calculation the solvus extends to a peritectic where the minimum liquidus is at 16.4 mol% MgO at 2264K. These calculations were based on a significant number of assumptions based on conflicting and sparse experi-

mental data, therefore the values should be seen as guides not hard numbers. The development of a metastable phase at the eutectic composition is not unexpected.[23,24] The development of kinetic metastable phases follows the same phase rules as thermodynamically stable phases.

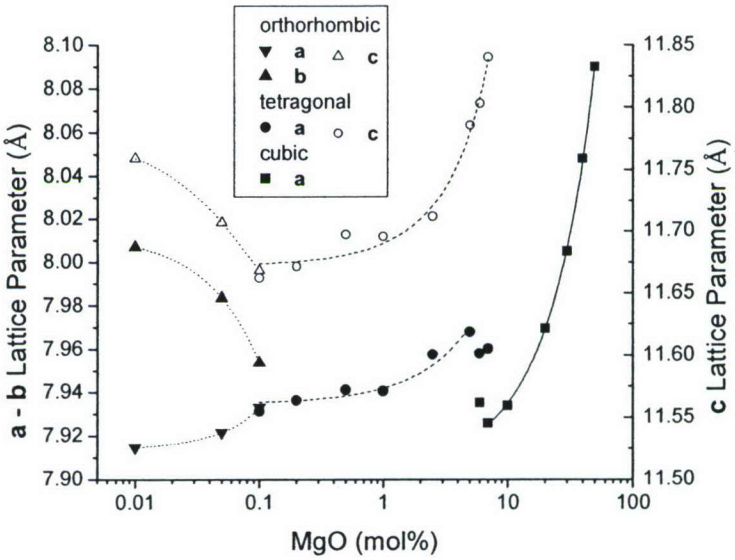

Figure 4: Lattice parameters of dominant phase with increasing MgO concentration from calculations using Figure 2 data. Lines are linear fits to the data.

To best illustrate the phase development in the $MgAl_2O_4$-Al_2O_3 system, the structures will be explained as deviations from the stoichiometric $MgAl_2O_4$ spinel structure. In the ideal spinel structure, the oxygen atoms form a face centered cubic lattice where Al^{3+} occupies half of the octahedral sites and Mg^{2+} occupies one eighth of the tetrahedral sites. It has been well documented that Mg^{2+} can also occupy the octahedral sites. The amount of octahedral occupancy is quantified as the degree of inversion. The degree of inversion found in natural and synthetic stoichiometric spinels can range from 0 to 40% based on the model by O'Neill and Navrotsky[25] and typical degrees of inversion are from 15 to 30%.[26] Assuming an ideal structure, as the MgO content is reduced from the stoichiometric spinel, the Al^{3+} ions occupy an increasing number of

tetrahedral positions. The Al^{3+} ions are accommodated in the tetrahedral positions and the spinel structure is maintained to 10 mol% MgO.

Below 10 mol% MgO, a new metastable phase develops. This structure is a tetragonal distortion of the cubic spinel where the c-axis is expanded by 50%. In the literature,[21] this phase is considered to be $MgAl_{20}O_{40}$ or 7.17 mol%, but the associated ICDD XRD crystal pattern is based on a unit cell with 48 oxygen atoms which, assuming one Mg atom in the crystal structure, corresponds to $MgAl_{31}O_{47.5}[]_{0.5}$ or 6.06 mol%. This tetragonal structure is dominant until the MgO content decreases below 1 mol% where an orthorhombic distortion of the tetragonal cell begins to develop and becomes dominant below 0.1 mol% MgO. The orthorhombic distortion is an expansion of one a-axis and a contraction of the other, Figure **4**. This distortion becomes larger with decreasing MgO contents. These lattice calculations are based on a minimization of the sum of the square calculations of a rather complex mixture of phases and do not correspond exactly with the published ICDD lattice parameters, but the graphed data fit Vegard's Law well and true structures of transition aluminas are the subject of much speculation in the literature.[27,28,29]

Table 2: Unit cell dimensions for selected transition aluminas and the relevant ICDD cards ($MgAl_2O_4$:73-1959, $MgAl_{26}O_{40}$: 20-0660, ∂^t-Al_2O_3:16-394, ∂^o-Al_2O_3:46-1131, and ∂^*-Al_2O_3:46-1215 and θ-Al_2O_3:23-1009

	∂^o-Al_2O_3: 46-1215	∂^*-Al_2O_3: 46-1131	∂^t-Al_2O_3: 16-394	θ-Al_2O_3: 23-1009	$MgAl_{26}O_{40}$: 20-0660	$MgAl_2O_4$: 73-1959
	Orthorhombic P222 (16)	Tetragonal P4m2 (115)	Tetragonal I	Monoclinic C2/m	Tetragonal I	Cubic Fd3m (227)
a	7.934	5.599	7.934	5.625	7.956	8.05
b β	7.956			2.906 104.1		
c	11.711	23.657	23.657	11.813	11.745	

Transition aluminas have often been referred to as consisting of distorted triple spinel unit cells.[30] The reported unit cell dimensions of selected transition aluminas are listed in Table **2**. The powders used to determine the structures all have different methods of production and thermal histories. The complex nature of atomic diffusion and structural reordering in transition aluminas precludes any bulk sample from being homogeneous or representative. This topic was thoroughly reviewed by Levin and Brandon.[28] However, the family of phases or crystalline reflections, which exist between the well-defined γ- and α-aluminas, can be viewed as diffusion limited structural relaxations dependent on surface energies, impurities and thermal history.

Diffuse reflectance infrared Fourier transform spectra (DRIFT)

DRIFT spectra of all samples are presented in Figure **5**. Two main regions are of interest, 1100-400 cm^{-1} and 4000 to 1500 cm^{-1}. The lower wave number region corresponds to typical νM-O bands and the higher region to absorbed surface species. Absorbed surface water is present on the as-prepared samples in the 3600-3000 cm^{-1} spectral region as a series of overlapping νO-H bands arising from both physisorbed and chemisorbed water. These as-prepared nanopow-

ders have no significant organic species at the surface, as the absence of 2900-1700 cm^{-1} vibrations suggests.

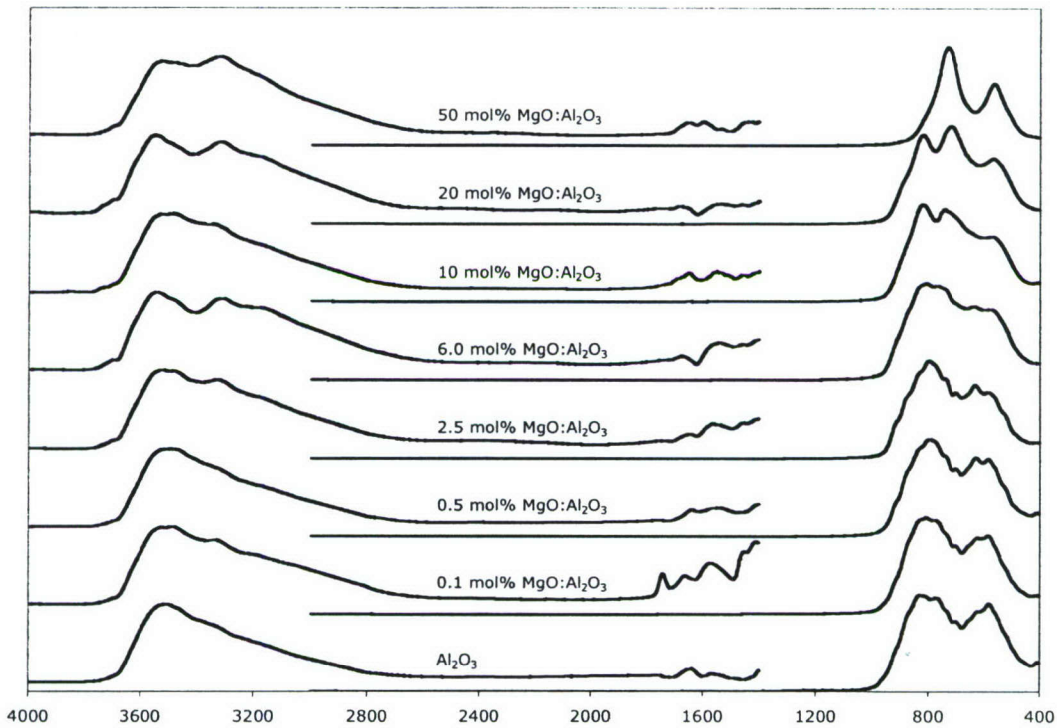

Figure 5: DRIFTS of selected samples along the $MgO\text{-}Al_2O_3$ tieline.

Complementary to following phase changes by XRD, it is possible to associate changes in the IR peak positions of the metal-oxygen stretches with the phases that form as the MgO content increases as illustrated in Figure **6**. The infrared absorbances in the 760 – 840 cm^{-1} spectral region are associated with tetrahedral Al-O ($\nu Al\text{-}O_t$). The conversion from a predominantly orthorhombic to tetragonal structure above 0.1 mol% MgO (XRD Figures **3** and **4**), also results in a convergence of the 780 and 825 cm^{-1} peaks to a single peak, centered at 800 cm^{-1}. The $\nu Al\text{-}O_t$ are dominant from 0.1 to 6 mol% MgO where the spinel structure begins to form. Between 6 and 10 mol% MgO the $\nu Al\text{-}O_t$ shifts back to 830 cm^{-1} and rapidly diminishes in intensity as the composition approaches stoichiometric spinel.

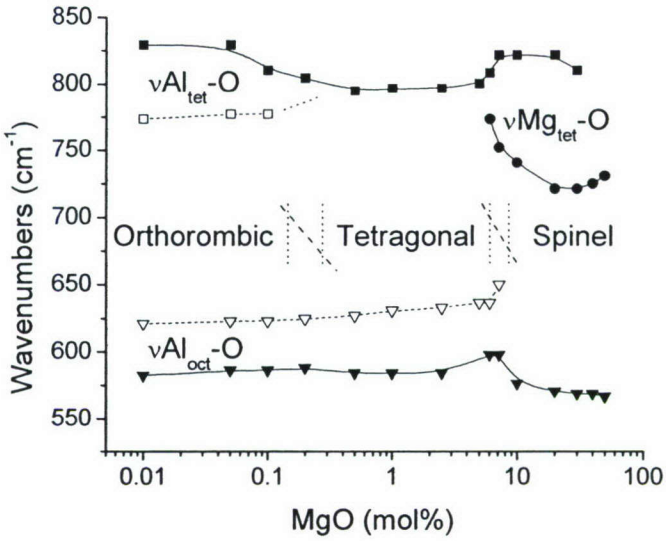

Figure 6: Changes in dominant phase and νM-O with MgO content.

The band centered at 725 cm^{-1}, which appears ≥ 5 mol%, is associated with tetrahedral Mg-O ($\nu Mg\text{-}O_t$) in the spinel structure. The $\nu Mg\text{-}O_t$ intensity is inversely related to the intensity of the 830 cm^{-1} $\nu Al\text{-}O_t$ as the stoichiometric spinel is approached.

The 625 and 585 cm^{-1} spectral bands are associated with octahedral Al-O ($\nu Al\text{-}O_o$). In the pure alumina sample the 625 cm^{-1} $\nu Al\text{-}O_o$ is of greater relative intensity than the 585 cm^{-1}, but as the MgO content increases, and the dominant structure changes from orthorhombic to tetragonal, the 585 cm^{-1} $\nu Al\text{-}O_o$ increases in relative intensity. The 625 cm^{-1} $\nu Al\text{-}O_o$ gradually changes in frequency from 620 to 630 cm^{-1} with increasing MgO content until the formation of the spinel phase when the 625 cm^{-1} $\nu Al\text{-}O_o$ disappears. This suggests that there are two distinct octahedral positions in the orthorhombic and tetragonal structures and only a single position in the cubic spinel. The remaining $\nu Al\text{-}O_o$ rapidly decreases in frequency from 595 to 565 cm^{-1} as the composition approaches the stoichiometric spinel.

In the pure Al_2O_3 sample, water is present primarily as chemisorbed water as evidenced by the comparatively narrow peak centered at 3500 cm^{-1}. As the MgO content increases the absorption due to water broadens to include a second resolved peak centered at 3325 cm^{-1} and an unresolved peak near 3175 cm^{-1}. The relative intensities of the resolved peaks at 3500 and 3325 cm^{-1} do not change with composition. The change in the surface νO-H bands offers the possibility of novel catalytic properties due to the associated change in Lewis site properties.[31]

Conclusions

We explored, combinatorially, the Al_2O_3 - $MgAl_2O_4$ phase field to investigate metastable phase formation and optimize the resultant UV emission behavior (results not shown). The entire phase field was produced using two mutually soluble precursors; alumatrane and magnesium acetylacetonate. We were able to extend the magnesium spinel phase field to below 10 mol% MgO in Al_2O_3. As the content of MgO decreased below the eutectic (6 – 7 mol% MgO), the tetragonal δ-alumina was found to be the dominant phase. With MgO contents below 1 mol%, the orthorhombic δ-alumina phase formed. These transitions were collaborated by XRD and FTIR. This metastable extension of the spinel structure across the entire Al_2O_3 - $MgAl_2O_4$ phase field at the nano scale creates the opportunity for new properties to be found in this well studied system.

When viewed in terms of decreasing MgO content, the structural changes form the cubic spinel to tetragonal δ-alumina to orthorhombic δ-alumina are simple reorganizations of the spinel crystal structure. The continuous replacement of Al^{3+} in the tetrahedral (ideally Mg^{2+}) positions of the spinel structure results in shrinkage of the unit cell and loss of symmetry.

References

(1) Guo, J.; Lou, H.; Zhao, H.; Chai D.; Zheng, X. *Appl. Cat. A* **2004**, 273, 75.

(2) Ghosh, A.; Ritwik S.; Mukherjee B.; Das S.K. *J. Europ. Cer. Soc.* **2004**, 24, 2079.

(3) Bhaduri, S.; Bhaduri, S. B. *Ceram. Inter.* **2002**, 28,153.

(4) Ghosh, A.; White, K. W.; Jenkins, M. G.; Kobayashi, A.S.; Bradt, R. C. *J. Am. Ceram. Soc.* **1991**, 74, 1624.

(5) Devanathan, R.; Yu, N.; Sickafus, K. E.; Nastasi, M. *J. Nuc. Mater.* **1996**, 232, 59.

(6) Chauvin, N.; Albiol, T.; Mazoyer, R.; Noirot, J.; Lespiaux, D.; Dumas, J. C.; Weinberg, C.; Ménard, J. C.; Ottaviani, J. P. *J. Nuc. Mater.* **1999**, 274, 91.

(7) Ginley, D.S.; Bright, C. *MRS Bull.* **2000**, 25 (8), 15.

(8) Bickmore, C. R.; Waldner, K. F.; Treadwell, D. R.; Laine, R. M. *J. Am. Ceram. Soc.* **1996**, **79**, 1419.

(9) Hinklin, T.; Toury, B.; Gervais, C.; Babonneau, F.; Gislason, F. F.; Morton, R. W.; Laine, R. M. *Chem. Mater.* **2004**, 16, 21.

(10) Baranwal, R.; Villar, M. P.; Garcia R.; Laine, R. M. *J. Am. Ceram. Soc.* **2001**, 84, 951.

(11) Marchal, J; Hinklin, T.; Baranwal, R.; Johns, T.; Laine, R. M. *Chem. Mater.* **2004**, 16, 822.

(12) Bickmore, C. R.; Waldner, K. F.; Baranwal, R.; Hinklin, T.; Treadwell, D. R.; Laine, R. M. *J. Europ. Ceram. Soc.* **1998**, 18, 287.

(13) Laine, R. M.; Marchal, J.; Sun, H. J.; Pan, X. Q. *Adv. Mater.* **2005**, 17, 830.

(14) Azurdia, J. A.; Marchal, J. C.; Shea, P.; Sun, H.; Pan, X. Q.; Laine, R. M. *Chem. Mater.* **2006**, 18, 731.

(15) Li, J. G.; Ikegami, T.; Lee, J. H.; Mori, T. *J. Am. Ceram. Soc.* **2000**, 83, 2866.

(16) Laine, R. M.; Marchal, J. C.; Sun, H. P.; Pan, X. Q. *Nat. Mater.* **2006**, 5, 710.

(17) Li, B.; Oliveira, S. L.; Rand, S. C.; Azurdia, J. A.; Hinklin, T. R.; Marchal, J. C.; Laine R. M. *J. Appl. Phys.* **2007**, 101, 053534.

(18) Azurdia, J. A.; Marchal, J. C.; Laine, R. M. *J. Am. Ceram. Soc.* **2006**, 89, 2749.

(19) Laine, R. M.; Hinklin, T. R.; Azurdia, J.; Kim, M.; Marchal, J. C.; Kumar, S. Unpublished.

(20) Li B.; Williams G.; Rand S. C.; Hinklin T.; Laine, R. M. *Opt. Lett.* **2002**, 27, 394.

(21) Lejus, A. M. *Rev. Hautes Temper. Et Refract.* **1964**, I, 53. (In French)

(22) Hallstedt, B. *J. Am. Ceram. Soc.,* **1992, 75**, 1497.

(23) Levi, C. G. *Acta Mater.* **1998**, 46, 787.

(24) Polli, A. D.; Lange F. F.; Levi, C. G. *J. Am. Ceram. Soc.* **1996**, 79 , 1745.

(25) O'Neill, H.; Navrotsky, A. *Am. Miner.* **1983**, 68, 181.

(26) Andreozzi, G. B.; Princivalle, F.; Skogby H.; Giusta, A. D. *Am. Miner.* **2000**, 85, 1164.

(27) Jayaram, V.; Levi, C. G. *Acta Metall.* **1989**, 37, 569.

(28) Levin, I.; Brandon, D. *J. Am. Ceram. Soc.* **1998**, 81, 1995.

(29) Cai, S. H.; Rashkeev, S. N.; Pantelides, S. T.; Sohlberg, K. *Phys. Rev. B* **2003**, 67, 224104.

(30) Lippens, B. C.; de Boer, J. H. *Acta Cryst.* **1964**, 17, 1312.

(32) Morterra, C.; Magnacca, G. *Catal. Today* **1996**, 27 (3-4), 497.

Additional Information

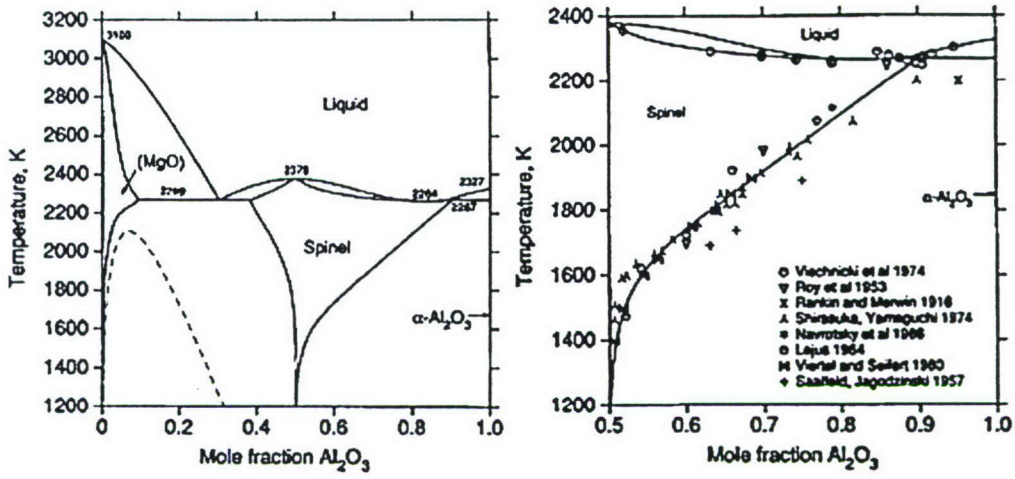

Figure A-1: Phase diagram for the $(MgO)_x(Al_2O_3)_{1-x}$ tie-line.[23]

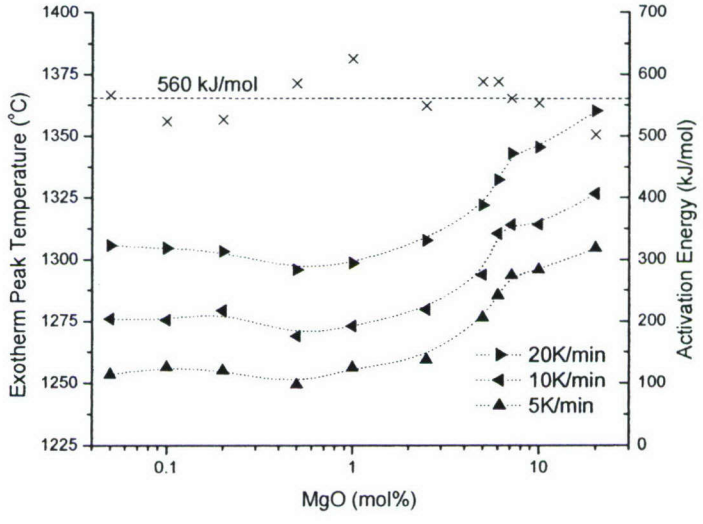

Figure A-2: Compilation of DTA peak positions for alpha alumina formation and corresponding Arrhenius plot activation energy.

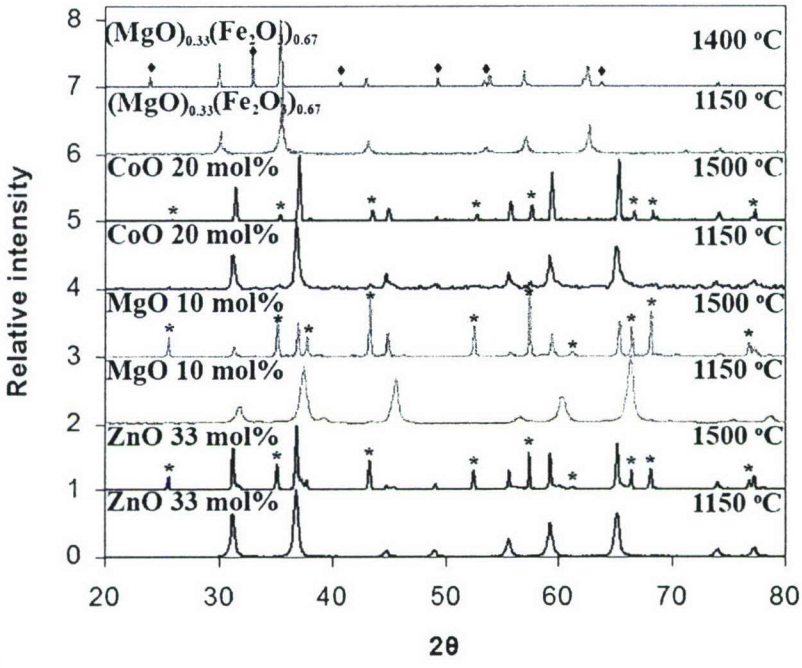

Figure A-3. XRD powder patterns for $(MO)_x(Al_2O_3)_{1-x}$ for x as shown and $(MgO)_{0.33}(Fe_2O_3)_{0.67}$ for powders heated to 1150°C (10°C/min/air) and to 1500°C/12 h. * = α-Al_2O_3, ◊ = α–Fe_2O_3 (1400°).

Finding spinel in all the wrong places

Richard M. Laine,* Thomas R. Hinklin, Jose Azurdia, Min Kim, Julian C. Marchal, Sameer Kumar
Department of Materials Science and Engineering, University of Michigan, Ann Arbor, MI 48109-2136
talsdad@umich.edu

RECEIVED DATE (to be automatically inserted after your manuscript is accepted if required according to the journal that you are submitting your paper to)

Richard M. Laine, Dept of Materials Science and Engineering, University of Michigan, Ann Arbor, MI, 48109-2136. (734) 764-6203, FAX 763-4788, talsdad@umich.edu

Spinel compounds are of continuing interest because they exhibit a wide range of novel and manipulable properties of value in electronic, electrical, magnetic, catalytic, photonic, and structural applications. Thus, the crystal structures, phase equilibria and composition ranges of materials that form both normal and inverse spinels have been studied extensively, frequently to optimize specific properties. We report here the use of liquid-feed flame spray pyrolysis (LF-FSP) to synthesize phase pure spinel aluminate nanopowders $(MO)_x(Al_2O_3)_{1-x}$ [M = Co, Cu, Mg and Zn] at compositions well outside the phase stability regions currently known for these materials. Typical powders consist of unaggregated single crystal particles with average particle sizes of 20-40 nm (TEM, XRD line broadening, BET) and corresponding surface areas of 60-70 m^2/g (BET). We were also successful in producing phase pure $(MgO)_x(Fe_2O_3)_{1-x}$ spinels at compositions outside its thermodynamic phase field to extend the generality of the approach. After heating to 1500°C/10 h, all of these materials transform to the appropriate mixed-phase compositions (spinel phase plus α-Al_2O_3 or α-Fe_2O_3). Given the valuable and diverse properties obtained for many different types of spinels, the possibility of expanding phase

fields and compositions beyond those known offers considerable potential for accessing entirely new materials' properties with mixed-metal nanopowders that are typically stable to 1000°C.

Nanopowders, spinel phase, liquid feed flame spray pyrolysis, kinetic phases, general synthetic techniques.

Liquid-feed flame spray pyrolysis of mixtures of metalloorganic precursors in EtOH at stoichiometries not expected to give spinel phase based on phase diagrams nonetheless produce high surface area, dispersible nanopowders that are often phase pure spinel.

Spinel compounds are of long standing interest because they exhibit valuable and/or unusual electronic, magnetic, catalytic, photonic, and structural properties.[1-16] Thus, the crystal structures, phase equilibria and composition ranges of materials that form both normal and inverse spinels have been studied extensively, frequently to optimize specific properties. Properties optimization drives continuing efforts to produce new materials, extend phase fields and improve homogeneity.[1-19] This in turn provides the impetus to develop new synthesis and processing approaches.

We recently demonstrated that liquid-feed flame spray pyrolysis, LF-FSP provides access to a new hexagonal phase in nano-$Y_3Al_5O_{12}$ and a general route to nano-α-Al_2O_3 (30-90 nm).[20,21] We now find that LF-FSP offers a general route to common phase pure spinel nanopowders, $(MO)_{1-x}(Al_2O_3)_x$ M = Mg, Ni, Co, Zn, and $(MgO)_{0.6}(Fe_2O_3)_{0.4}$, with compositions previously unknown thereby greatly extending their phase fields.[1,2,13-20,22] Given their significant academic and commercial import, access to entirely new compositions in spinel phase materials could expand the horizons of spinel materials' properties greatly.

In LF-FSP, alcohol solutions of metalloorganics [e.g. $Al(OCH_2CH_2)_3N$ (alumatrane) and Mg(2,4-pentanedionato)$_2$] are aerosolized with O_2 into a quartz chamber (1.5 m) and combusted[23] at 1500°-2000°C. Quenching to $\approx$ 300°C in $\leq$ 30 μs over $\approx$ 1 m gives dispersible nanopowders often with novel phases as noted above[20,21] and for example a one step synthesis of the difficult to produce Na^+ doped β"-alumina.[23]

In an effort to dope nano-α-Al_2O_3 with MgO to prevent grain growth during sintering,[24] LF-FSP was used to combinatorially produce MgO doped nano-δ-Al_2O_3 as a prelude to a second pass through the LF-FSP system to produce Mg doped α-Al_2O_3.[25] Figure **1** shows XRDs for LF-FSP generated $(MgO)_x(Al_2O_3)_{1-x}$ nanopowders where x = 0-0.20. Exact compositions were confirmed by XRF analyses.[25]

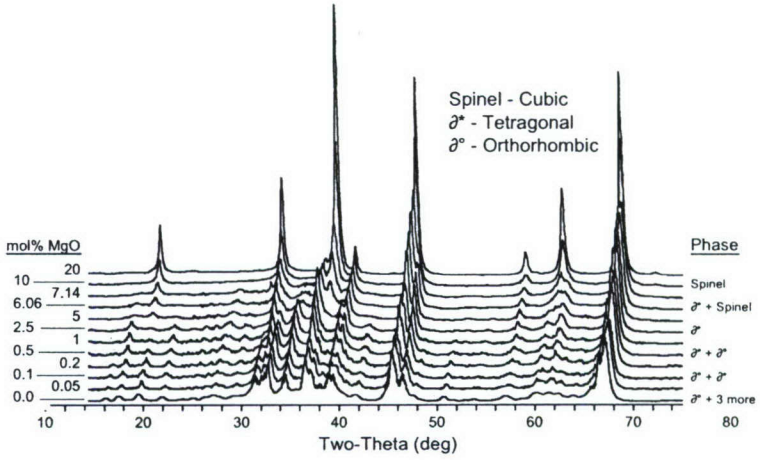

Figure 1. XRDs for $(MgO)_x(Al_2O_3)_{1-x}$ for x = 0-20 mol %, MgO content determined by XRF.[25]

As substantiated by numerous studies,[9-16,26-28] the MgO-Al_2O_3 phase diagram shows that stoichiometric spinel is stable to ≈ 2100°C. It also indicates that in the alumina rich region, off-stoichiometric spinel phase forms at 63-83 mol % Al_2O_3 at 1500°-1900°C, but the stability zone contracts rapidly at higher temperatures. In contrast, LF-FSP processing provides a material that is ≥ 95 % spinel phase at 90 mol % Al_2O_3 as determined by XRD and FTIR.[25] Furthermore, at ≈ 94 mol %, XRD analysis indicates formation of a third phase together with a small amount of δ-Al_2O_3 rather than α-Al_2O_3, the expected second phase.

The third phase, observed at the 6.06 mol % MgO eutectic with an apparent formula of $MgAl_{31}O_{47.5}[]_{0.5}$, was reported previously to form near 93 mol % alumina with a formula of $MgAl_{26}O_{40}$.[27,28] As we will report in more detail later, for $(MgO)_x(Al_2O_3)_{1-x}$, one can also closely track the changes in specific phases observed through changes in lattice parameters and FTIR absorption band positions as a function of composition.

These results combined with studies on nickel aluminates, $(NiO)_x(Al_2O_3)_{1-x}$,[29] prompted efforts to explore the general utility of LF-FSP to produce hitherto unknown spinel compositions in different nano-alumina spinels. Figure **2** provides XRDs for selected compositions of $(MO)_x(Al_2O_3)_{1-x}$ for M = Ni, Co, Mg and Zn which are all stable to 1150°C.

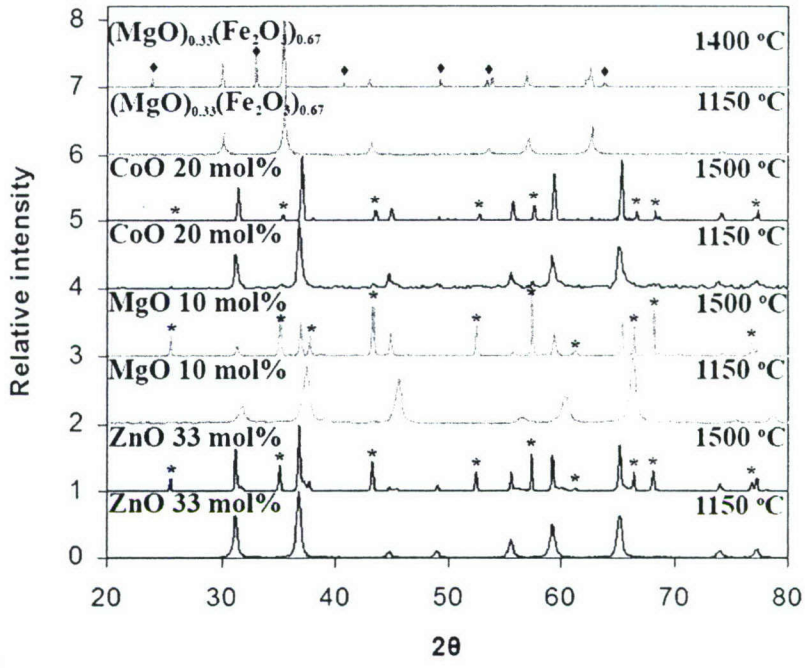

Figure 2. XRD powder patterns for $(MO)_x(Al_2O_3)_{1-x}$ for x as shown and $(MgO)_{0.33}(Fe_2O_3)_{0.67}$ for powders heated to 1150°C (10°C/min/air) and to 1500°C/12 h. * = α-Al_2O_3, ◊ = α–Fe_2O_3 (1400°).

All of these nanopowders have typical average particle sizes of 20-40 nm (see Figure **3** examples) and corresponding surface areas of 50-70 m^2/g. In some instances, as in the nickel system,[29] the materials are mostly the inverse spinel.

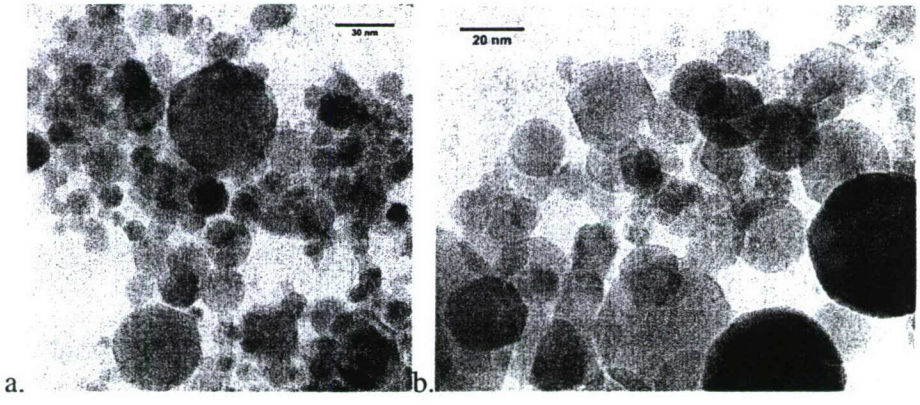

a. b.

Figure 3. TEMs of a. $(NiO)_{0.22}(Al_2O_3)_{0.78}$ and b. $(CoO)_{0.08}(Al_2O_3)_{0.92}$.

The reported $(NiO)_x(Al_2O_3)_{1-x}$ phase diagram shows a spinel phase field in the alumina rich region that extends from x = 0.50 to 0.60 at 1500°C but broadens to ≈ 0.68 at temperatures near 2000°C.[30] Thus,

our observation of a pure spinel phase at x = 0.78 greatly extends this phase field. The resulting spinel is very stable, resisting transformation to the phase diagram composition even on heating for 10 h at 1150°C, Figure **2**.

Similar observations are made for the $(CoO)_x(Al_2O_3)_{1-x}$ system, where at 1500°C the published phase diagram in the alumina rich region extends to 45 mol % (x = 0.45) but expands to 78 mol % near 1950°C.[32,33] We observe a pure spinel phase at 79 mol % and mostly spinel at 90 mol % with some δ-Al_2O_3. Here we appear to be equivalent to the thermodynamic materials. But our materials exhibit a shift in the powder pattern of 0.3-0.4°2θ with the secondary phase being δ- rather than α-Al_2O_3. We assume the shift in °2θ is due in part to some inverse spinel forming and also substitution of the much smaller Al^{3+} ion for Co^{2+} in tetragonal sites.[31,32]

For $(ZnO)_x(Al_2O_3)_{1-x}$, the published phase diagram[33] shows that in the Al_2O_3 rich region at 57 mol % Al_2O_3, the spinel phase is stable only in a very narrow window from 1700° to 1800°C. Below 1700°C a mixture of α-Al_2O_3 and spinel phase are observed. However, in the LF-FSP materials, we observe phase pure spinel at $(ZnO)_{0.33}(Al_2O_3)_{0.67}$ perhaps suggesting that the formation temperatures of our powders are ≥ 1700°C and that we trap the phase pure spinel by rapid quenching. Note that according to the phase diagram,[33] a liquid spinel/solid α-Al_2O_3 mixture form above 1800°C. Given the size of our particles and the fact that nano particles are likely to be liquid well below the bulk melting temperature, we suspect that in our system the as-produced powders form from liquid droplets produced in the flame.

On heating to temperatures of 1400-1500°C, these materials transform to the expected phase compositions [spinel/α-Al_2O_3 (α-Fe_2O_3)] as shown in Figure **2**, confirming the true compositions of the LF-FSP produced nanopowders. However, they are all stable at 1150°C for prolonged periods pointing to their potential to offer unique properties at moderate temperatures, for example as catalysts.

In all of the Figure **2** as-produced materials, the alumina rich region of the phase diagram indicates that only α-Al_2O_3 is the expected second phase for all temperatures. Yet, we observe only δ–Al_2O_3 presumably because in all cases we are producing kinetic products. An alternate explanation is that

δ–Al_2O_3 forms as a separate nanopowder product during LF-FSP rather than in an intimate phase separated mixture. However for the phase pure materials, no evidence of a second δ–Al_2O_3 phase is observed belying this explanation.

To better demonstrate generality, we also prepared $(MgO)_x(Fe_2O_3)_{1-x}$ materials using the same processing conditions as for the $(MO)_x(Al_2O_3)_{1-x}$ systems discussed above. Iron propionate, $Fe(O_2CCH_2CH_3)_3$, and Mg(2,4-pentanedionato)$_2$ were used to make various $(MgO)_x(Fe_2O_3)_{1-x}$ compositions in the range x = 29-63 MgO as measured by XRF.[34] These nanopowders have typical average particle sizes of < 20 nm and corresponding surface areas of $\approx$ 70 m^2/g as confirmed by SEM and BET. The materials were analyzed using powder XRD, and determined to all be single-phase magnesioferrite spinel at compositions up to x = 70.

According to the published phase diagram for the $(MgO)_x(Fe_2O_3)_{1-x}$ system,[35] these materials should exist as phase separated spinel + periclase (MgO) at $x > 0.5$, and spinel + hematite (Fe_3O_4) for $x \leq 0.5$. Similar to the $(MO)_x(Al_2O_3)_{1-x}$ systems, we observe single-phase spinel for compositions as much as $\approx$ 15 mol % outside the thermodynamically determined phase field.

In summary, it is clear that a combination of very homogeneous mixing of ionic species in the gas phase at very high temperatures followed by a very rapid quench provides a general means of producing sets of spinel nanomaterials that were hitherto impossible or very difficult to obtain previously. Furthermore, the $(MgO)_x(Fe_2O_3)_{1-x}$ powders which are superparamagnetic suggest that our approach to novel materials is not limited to aluminates. Because spinel phase materials are of such significant academic and commercial import, the process and the materials described here show considerable portent to develop entirely new materials some of which are certain to have sets of properties hitherto unknown. Thus, the horizons of spinel materials have been expanded greatly.

ACKNOWLEDGMENTS

We thank the Air Force Office of Scientific Research for support of this work through Contract No. F49620-03-1-0389. SK thanks Hyundai Motors for fellowship support.

References

1. O'Neill, H.S.C.; Navrotsky, A., *Am. Mineral.* **1983** *68*, 181.

2. Sickafus, K.E., Wills, J.M., Grimes, N.W. *J. Am. Ceram. Soc.* **1999**, *82*, 3279.

3. Han, M., Vestal, C.R., Zhang, Z.J., *J. Phys. Chem. B* **2004**, *108*, 583.

4. Parker, D.R. *et al*, *J. Am. Chem. Soc.* **2004**, *126*, 2710.

5. Clarke, D.R., , *J. Am. Ceram. Soc.* **1999**, *82*, 485.

6. Gritsyna, V.T *et al*, *J. Am. Ceram. Soc.* **1999**, *82*, 3365.

7. Arean, C.O. *et al Mater. Lett.* **1999**, *39*, 22.

8. Arean, C.O., *et al Micropor. Mater.* **1997**, *8*, 187.

9. Parimal, J.; Patel, P.J.; Glide, G.A.; Dehmer, P.G.; McCauley, J.W.; in Inorganic Optical Materials II, A.J. Marker III, E.G. Arthurs, Eds. SPIE vol **4102** (2000) pp 1-14.

10. Yoo, J.S., Bhattachariyya, A.A., Radlowski, C.A., *Ind. Eng. Chem. Res.* **1991**, *30*, 1444.

11. Kagata, H., Saito, R., Kastumura, H., *J. Electroceram.* **2004**, *13*, 277.

12. Panda, P.C.; Raj, R. *J. Am. Ceram. Soc.* **1986**, *69*, 363.

13. M.F. Zawrah, *Mater. Sci. Eng. A.* **2004**, *382*, 362.

14. Navrotsky, A. Wechsler, B.A.; Geisinger, K.; Seifert, F.; *J. Am. Ceram. Soc.* **1986**, *69*, 418.

15. Bhaduri, S.; Bhaduri, S.B., *Ceram. Internat.* **2002**, *28*, 153.

16. Yang, N., Chang, L.; *Mater. Lett.* **1992**, *15*, 84.

17. Several $MgO{\cdot}Al_2O_3$ spinel precursors have been synthesized, characterized and described in the literature.[18,19]

18. Pflanz, K.B., Riedel, R., Chmiel, H., *Adv. Mater.* **1992**, *4*, 662.

19. Veith, M.; Altherr, A., Wolfanger, H., *Chem. Vap. Deposition*,**1999**, *5*, 87.

20. Laine, R.M. Marchal, J.; Sun, H.J.; Pan, X.Q *Adv. Mater.* **2005**, *17*, 830.

21. Laine, R.M.; Marchal, J.C.; Sun, H.P.; Pan, X.Q *Nature Materials* **2006**, *5*, 710.

22. Bickmore, C.R.; Waldner, K.F.; Treadwell, D.R.; Laine, R.M.; *J. Am. Ceram. Soc.* **1996**, *79*, 1419.

23. Sutorik, A.C.; Neo, S.S.; Hinklin, T.; Baranwal, R.; Treadwell, D.R.; Narayanan, R.; Laine, R.M., *J. Am. Ceram. Soc.* **1998**, *81*, 1477.

24. a. Krell, A., Blank, P.; Ma, H.; Hutzler, T.; Apetz, R.; van Bruggen, M.P.B.; *J. Am. Ceram. Soc.* **2003**, *86*, 12. b. Apetz, R.; van Bruggen, M.P.B., *J. Am. Ceram. Soc.* **2003**, *86*, 480.

25. Hinklin, T.R., Ph.D. Dissertation "Mixed-metal Oxide Nanopowders for Structural and Photonic Applications." University of Michigan, 2006.

26. Hallstedt, B.; *J. Am. Ceram. Soc.* **1992**, *75*, 1497 and references therein.

27. Mangin A., Forestier, H., *C.R. hebd. Séances Acad. Sci.* , *242* 1893-95 (1956).

28. Jagodzinski, H. *Zeitschrift für Kristallographie***1957**, *109* S. 388.

29. Azurdia, J.A.; Marchal, J.C.; Shea, P.; Sun, H.; Pan, X.Q.; Laine; R.M.; *Chem. Mater.* **2006**, *18*,

731.

30. Phillips, B.; Hutta, J.J.; Warshaw, I., *J. Am. Ceram. Soc.*, **1963**, *46*, 581.

31. Azurdia, J., Marchal, J., Laine, R.M., J. *Am. Ceram. Soc.* **2006**, ***89***, 2749.

32. Mori, T., *Nippon. Seram. Kyo. Gak* **1982**, *90*, 100.

33. Hansson, R.; Hayes, P.C.; Jak, E., *Metall. Mater. Trans. B* **2004**, *35B*, 633.

34. Kumar, S.; Laine, R.M. manuscript in preparation.

35. Willshee, J.C.; White, J. *Trans. Br. Ceram. Soc.* **1967**, *54*, 333.

SYNOPSIS TOC

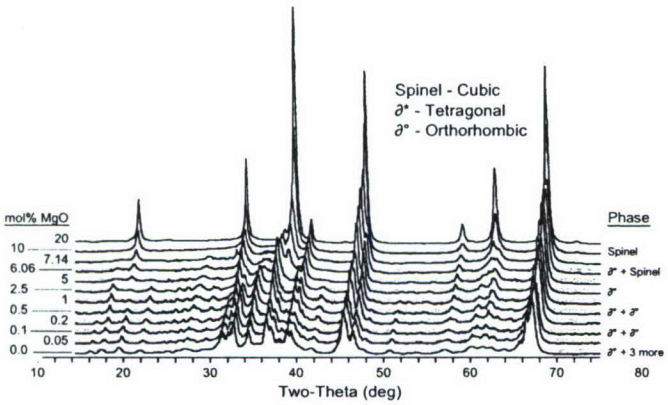

journal

J. Am. Ceram. Soc., 89 [9] 2749–2756 (2006)
DOI: 10.1111/j.1551-2916.2006.01155.x

Synthesis and Characterization of Mixed-Metal Oxide Nanopowders Along the CoO_x–Al_2O_3 Tie Line Using Liquid-Feed Flame Spray Pyrolysis

Jose Azurdia, Julien Marchal, and Richard M. Laine†

Departments of Materials Science and Engineering, and the Macromolecular Science and Engineering Center, University of Michigan, Ann Arbor, Michigan 48109-2136

We report here the use of liquid-feed flame spray pyrolysis (LF-FSP) to produce a series of nanopowders along the CoO_x–Al_2O_3 tie line. The process is a general aerosol combustion synthesis route to a wide range of lightly agglomerated oxide nanopowders. The materials reported here were produced by aerosolizing ethanol solutions of alumatrane [$Al(OCH_2CH_2)_3N$] and a cobalt precursor, made by reacting $Co(NO_3)_2 \cdot 6H_2O$ crystals with propionic acid. The compositions of the as-produced nanopowders were controlled by selecting the appropriate ratios of the precursors. Nine samples with compositions $(CoO)_y(Al_2O_3)_{1-y}$, $y = 0-1$ along the CoO_x–Al_2O_3 tie line were prepared and studied. The resulting nanopowders were characterized by X-ray fluorescence, BET, scanning electron microscopy , high-resolution transmission electron micrographs, X-ray diffraction (XRD), thermogravimetric analysis (TGA), and FTIR. The powders typically consist of single-crystal particles <40 nm diameter and specific surface areas (SSAs) of 20–60 m^2/g. XRD studies show a gradual change in powder patterns from δ-Al_2O_3 to Co_3O_4. The cobalt aluminate spinel phase is observed at stoichiometries (21 and 37 mol%) not seen in published phase diagrams, likely because LF-FSP processing involves a quench of >1000°C in microseconds frequently leading to kinetic rather than thermodynamic products. Likewise, the appearance of Co_3O_4 rather than CoO as the end member in the tie line is thought to be a consequence of the process conditions. TGA studies combined with diffuse reflectance FTIR spectroscopic studies indicate that both physi- and chemi-sorbed H_2O are the principal surface species present in the as-processed nanopowders. The only sample that differs is Co_3O_4, which has some carbonate species present that are detected and confirmed by a sharp mass loss event at ~ 250°C. The thermal behavior of the high cobalt content samples differs greatly from the low cobalt content samples. The latter behave like most LF-FSP-derived nanopowders exhibiting typical 1%–4% mass losses over the 1400°C range due mostly to loss of water and some CO_2. The high cobalt content samples exhibit a sharp mass loss event that can be attributed to the decomposition of Co_3O_4 to CoO.

I. Introduction

Cobalt oxides are used as catalysts for hydrocracking fuels,[1] in several selected and complete oxidation processes,[2,3] as well as in steam reforming of ethanol.[4] Co_3O_4 shows good catalytic activity for the low-temperature combustion of CO and organics.[5] At higher temperatures, the catalyst becomes reducing, converting CO_2 to CO and O_2 without a reducing reagent.[6]

Supported cobalt is often a co-catalyst for hydrocracking waste gases and contaminated fluids[7] to innocuous gases including NO_x. Traditional *de*-NO_x catalysts usually contain one of several very expensive metals including Pd, Pt, Rh, and Ru.[8,9] Supported cobalt systems offer considerable potential as low-cost, selective alternatives for catalytic reduction of NO_x.[10–12]

Cobalt has also been used since prehistoric times as a component in many pigments, particularly for deep blues.[13,14] Typical pigments consist of spinel or olivine phases produced from mixtures of cobalt and SiO_2, ZrO, TiO_2, or Al_2O_3.[15,16] There continues to be considerable active research on cobalt pigment technology to optimize color hues and luminescent properties.[17–19] Cobalt pigments are also used in high-end optical filters and magnetic recording media.[20,21]

The literature is replete with synthetic routes to cobalt oxides, and cobalt-containing materials especially for compositions along the CoO_x–Al_2O_3 tie line. The standard method is via a solid-state reaction of the parent oxides. Other synthesis methods include sol–gel,[22,23] co-precipitation,[24,25] hydrothermal,[26] polymeric precursor,[27] and vapor deposition processing.[28] We demonstrate here the use of liquid-feed flame spray pyrolysis (LF-FSP) to assess combinatorially compositions along the CoO_x–Al_2O_3 tie line. Spray pyrolysis techniques are well known and have been described extensively in the literature: they have been used to synthesize simple and complex oxide powders.[29,30] The advantage of LF-FSP over other techniques is that it allows production of up to 15 different compositions in the time span of a single week and hence can be considered a combinatorial method of synthesizing metal oxide nanopowders.

The LF-FSP process as invented and currently used at University of Michigan,[31] aerosolizes mixtures of metalloorganic compounds (metal carboxylates and/or alkoxides) dissolved in alcohol solvents at known concentration levels using oxygen. The resulting aerosol is ignited via methane pilot torches by combusting the mixture at temperatures between 1500° and 2000°C. The combustion-derived "soot" is collected using wire-in-tube electrostatic precipitators (ESP) as detailed elsewhere.[32] This "soot" consists, normally, of single crystal particles with average particle sizes (APSs) of 10–200 nm depending on processing conditions and corresponding specific surface areas (SSAs) of 100–20 m^2/g. These nanopowders normally have the same composition as that found in the original precursor solution including any inadvertent impurities.

We have previously shown that LF-FSP processing can be used to prepare well-known single metal nanopowders such as alumina (δ-Al_2O_3) and titania (90% anatase, 10% rutile). LF-FSP also provides access to complex mixed-metal oxide materials including mullite, $Y_3Al_5O_{12}$, $SrSi_2Al_2O_8$, and $\beta''Al_2O_3$.[33–35] Because we can control compositional make-up to ppm levels, it is possible to also dope pure materials for photonic, electronic, and catalytic applications.[36,37] In the latter arena, we have recently demonstrated that we can process materials along the

G. Soraru—contributing editor

Manuscript No. 21198. Received November 29, 2005; approved April 7, 2006.
†Author to whom correspondence should be addressed. e-mail: talsdad@umich.edu

TiO_2–Al_2O_3, NiO–Al_2O_3, ZnO–Al_2O_3, and MgO–Al_2O_3 tie lines with the discovery of several unusual phase compositions.[38,39] In this paper, we extend our efforts to develop materials with novel phase compositions of potential interest to the catalyst and pigment industry.

II. Experimental Procedure

(1) Materials

Cobalt nitrate hexahydrate [$Co(NO_3)_2 \cdot 6H_2O$, 99.97%], propionic acid [$CH_3CH_2CO_2H$, 99+%], triethanolamine [$N(CH_2CH_2OH)_3$ 98%], and anhydrous ethanol [CH_3CH_2OH, 99+%] were purchased from Alfa Aesar and used as received. Aluminum tris(sec-butoxide), [$Al(OsBu)_3$, 97%] was purchased from Chattem Chemical Co. and also used as received.

(2) Precursor Formulations

[$Al(OCH_2CH_2)_3N$] was synthesized from $Al(OsBu)_3$ and $N(CH_2CH_2OH)_3$ as described elsewhere,[40] and then diluted with EtOH to produce ~6 L of solution with a ceramic loading of 21 wt% by thermogravimetric analysis (TGA).

Cobalt precursor was prepared by adding 200.0 g (0.687 mole) of $Co(NO_3)_2 \cdot 6H_2O$ crystals to a 500 mL flask equipped with a still head and an N_2 sparge. $CH_3CH_2CO_2H$ (400 mL, 5.36 moles) was added and the resulting solution was heated to ~150°C for 6 h to distill off ~140 mL of liquid (water/$CH_3CH_2CO_2H$) and coincidentally remove NO_x gas. The remaining liquid product was placed in a clean 500 mL Nalgene® bottle. The ceramic loading of the solution was determined by TGA to be 3.3 wt%. We did not further identity this precursor because it is very volatile and coated our TGA instrument, reacting rapidly with any exposed Al_2O_3 forming a cobalt aluminate spinel.

(3) LF-FSP

The LF-FSP system has been described elsewhere in detail.[41] Ethanol precursor solutions were prepared by diluting the sample precursors to a 2–5 wt% ceramic yield, typically 4 wt%. These solutions are then atomized with O_2 through a nozzle. The fine mist generated is ignited with methane–oxygen pilot torches achieving combustion temperatures >1500°C. The products are carried downstream by a radial pressure blower (19.8 m^3/min), and collected downstream in ESP maintained at a 10 kV DC potential. The nanopowders are finally recovered manually from the ESP tubes after the system has cooled down.

(4) Analytical Methods

Chemical analyses were obtained by X-ray fluorescence (XRF) from Ford Motor Company (Dearborn, MI). XRF samples were prepared by mixing 0.50 g of sample in 10.0 g of $Li_2B_4O_7$ glass flux. The sample and glass flux were mechanically stirred for 5 min in a methacrylate vial with three methacrylate balls using an SPEX 6000 ball mill. The mixtures were fused into glass beads by placing them in an oven held at 1000°C for 10 min. The samples were analyzed using a Panalytical PW2400 XRF spectrometer (formerly Philips), equipped with a WDS detection system (wavelength dispersive), by Ford Motor Company personnel.

Surface area analyses were obtained using a Micromeritics ASAP 2010 sorption analyzer (Norcross, GA) for all powders. Samples were loaded (350 mg) and degassed at 350°C until a degas rate of <5 mTorr was achieved, followed by analysis at 77 K with N_2 as the adsorbate gas. The SSAs were calculated using the BET multipoint method. The particles' average diameter was determined by:

$$d = \frac{6}{\rho \times \mathrm{SSA}} \quad (1)$$

where ρ is the theoretical density of the powders and SSA is the specific surface area.

Scanning electron microscopy (SEM) A Philips XL30 SEM (Philips, Eindhoven, the Netherlands) instrument was used to acquire electron micrographs of all samples. The powder samples were first dispersed in 5 mL of DI water using an ultrasonic horn (Vibra-cell, Sonics and Materials Inc., Newton, CT), and next a drop was placed on an SEM sample stub, which was heated on a covered hot plate. The stubs were sputter coated using a Technics Hummer VI sputtering system (Anatech Ltd., Alexandria, VA) to improve resolution.

High-resolution transmission electron micrograph (HR-TEM) images were acquired using a JEOL 4000EX (Osaka, Japan) electron microscope operated at 400 kV. Samples were mounted on a Gatan double-tilt goniometer; they were prepared by dispersing ~5 mg in 5 mL of isopropanol. An ultrasonic water bath at room temperature was used for 5 min to create a homogeneous dispersion. A drop of the dispersion was then placed on a holey carbon film on Cu grids, 300 mesh (SPI Industries, Indianapolis, IN), and placed on a covered hot plate to dry.

X-ray diffraction analysis (XRD) was performed on a Rigaku Rotating Anode Goniometer (Rigaku Denki Co. Ltd., Tokyo, Japan). The powder samples were prepared by packing ~100 mg into in an amorphous silica holder, which were loaded into the machine. Continuous scans were performed from 20° to 80° 2θ, in 0.05° increments at 2°/min. Cu$K\alpha$ radiation (l = 1.54 Å) with a working voltage of 40 kV and a current of 100 mA were used to produce the X-rays. Scan data was analyzed to determine APSs and phases present, using Jade software (Materials Data Inc., Livermore, CA).

Thermogravimetric and differential thermal analysis (TGA–DTA) were performed on an SDT 2960 simultaneous DTA–TGA instrument (TA Instruments Inc., New Castle, DE). Samples were prepared by weighing ~40 mg of powder and pressing it into a pellet (3.0 mm diameter) using a dual action hand press. The samples were placed in an alumina holder and an empty pan was used as a reference. The instrument was ramped 10°C/min up to 1400°C under a continuous flow of 60 mL/min of synthetic air.

Diffuse reflectance infrared fourier transform spectrometry (DRIFTS) for all powders was acquired using a Mattson Galaxy Series FTIR 3000 spectrometer (Mattson Instruments Inc., Madison, WI). Background scans of optical grade KBr were performed by grinding ~400 mg using an alumina mortar and pestle and then packing the powder into a sample holder, and collecting a spectrum. Samples were prepared by adding 4 mg of sample to 400 mg of KBr and grinding them as the background sample. Spectra were collected continuously in the range of 4000–400 cm^{-1} with a scan resolution of ± 4 cm^{-1}, with an average of 156 scans. The sample chamber was flushed continuously with N_2 to remove atmospheric CO_2 and moisture.

III. Results and Discussion

We report here the synthesis and characterization of nine nanopowders with compositions along the CoO_x–Al_2O_3 tie line. These materials, produced in a single-step process, offer advantages over more conventionally prepared materials because LF-FSP provides access to phase compositions that are otherwise hard or impossible to attain. This method is extremely versatile, allowing combinatorial alterations of compositions with minimal effort and precise control. Thus, it is possible to produce 40 g samples of 15 different compositions in roughly 5 days or more samples with smaller sample sizes.

All samples exhibit relatively high SSAs, have no microporosity (from T-plot analysis and transmission electron micrographs (TEMs) micrographs), and have spherical morphologies. These and other properties make them excellent candidates for catalytic or pigment applications, both as pure materials and supported on alumina, silica, or other inert oxide support.

Table I. Precursor Compositions

Sample	(Mol%) Co
1	0
2	4
3	8
4	21
5	37
6	50
7	87
8	94
9	100

A discussion on the formulation of the precursors and nanopowder production follows. We then discuss particle morphology in terms of SSAs, shape and size, and surface species using a variety of characterization methods.

(1) Precursor Formulations

Nine different precursor formulations (see Section *II* and Table I) were used to produce nanopowders along the CoO_x–Al_2O_3 tie-line. Precise amounts of $[Al(OCH_2CH_2)_3N]$ and cobalt precursor solutions were diluted with EtOH and stirred mechanically before use for LF-FSP processing. Solutions used to produce the powders contained 2–4 wt% ceramic in precursor form by TGA, to minimize rheological complications with the LF-FSP process. The compositions produced are listed in Table I. We produced 40 g samples of all powders at 30–100 g/h rates. XRF was used to obtain elemental analyses of selected samples, and the results showed that the compositions were within experimental error of the precursor compositions.

(2) Powder Characterization

SSAs of all as-produced samples are shown in Fig. 1. The SSAs clearly decrease toward the CoO_x-rich end of the tie line, with the exception of the Co_3O_4 powder. The decrease appears coincident with the formation of cobalt spinel phase as Co^{3+} ions are incorporated into the Al_2O_3 matrix. The increase in surface area of the last sample results from oxidation of CoO to Co_3O_4, which causes a phase change coincident with a change in density, leading to an intrinsic increase in SSA. No microporosity was expected nor detected in any of the samples.

The APSs were estimated from the SSAs and the theoretical density of the powders, and compared with values obtained by Debye–Scherrer XRD peak-broadening analyses. The theoretical density values where computed using the known values of the end members and middle composition of the tie line, (Al_2O_3, $CoAl_2O_4$, and Co_3O_4) and interpolating using compositions in mole percent for the various samples. Particle sizes obtained by Debye–Scherrer peak broadening differ somewhat from those calculated from BET calculations (see Table II).

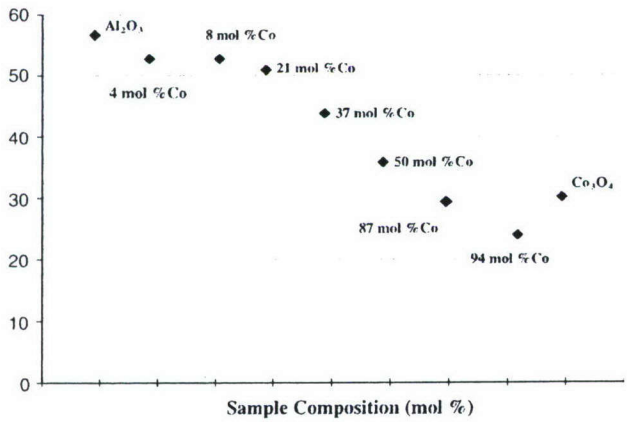

Fig. 1. Specific surface areas (SSAs) of all powder samples. SSAs are ± 2 m^2/g.

Table II. Average Particle Sizes (APS) from BET and XRD Data

Sample	(Mol%) Co	BET APS (nm)	XRD APS (nm)
1	Al_2O_3	29	29
2	4	31	18
3	8	30	21
4	21	30	20
5	37	32	19
6	50	38	22
7	87	35	21
8	94	40	22
9	100	32	20

XRD, X-ray diffraction.

The APS values from peak-broadening technique are lower by ~10–20 nm; this is possibly due to a difference in actual versus theoretical densities of the powder, except for the value of pure Al_2O_3, which corresponds well with the value calculated from the SSA. The APS of all powders is <40 nm regardless of the technique used to calculate the value, and remains relatively constant for all compositions studied.

Scanning electron micrographs (SEMs) of all samples provided an understanding of particle morphology. Figure 2 shows SEMs of the 21 and 50 mol% Co samples, which are representative of all other samples. The powders exhibit spherical morphologies throughout and the images suggest relatively narrow particle size distributions. The SEMs show a few particles in the 100–150 nm range and some agglomerates formed via electrostatic interactions. Figure 2(b) was taken at low magnification to

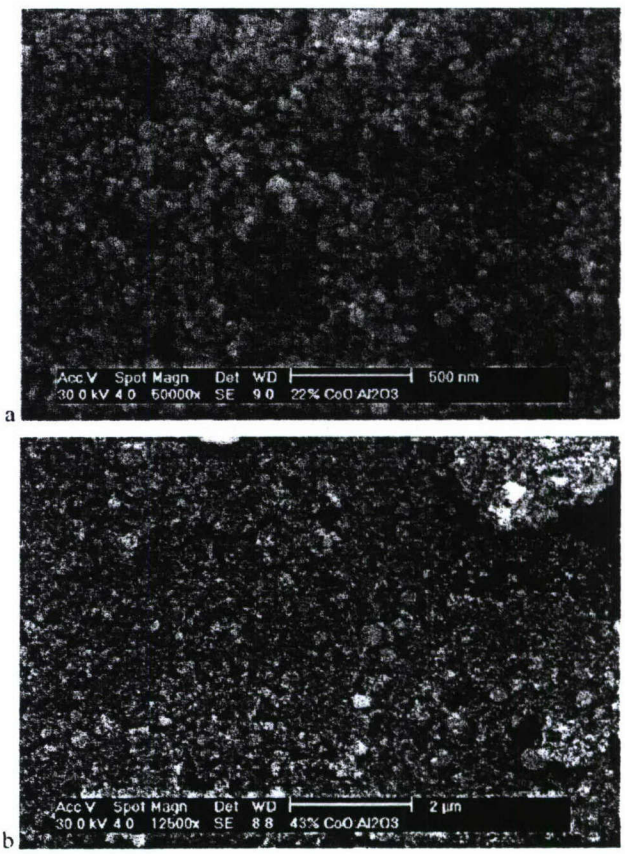

Fig. 2. SEMs showing homogenous spherical morphology and narrow particle distribution.

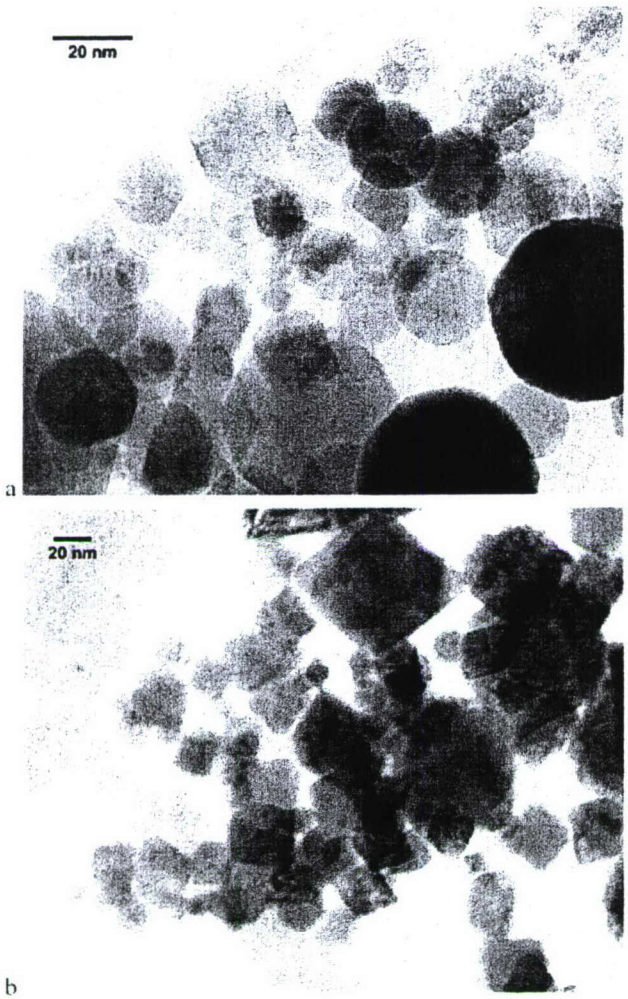

Fig. 3. Transmission electron micrographs of 8 and 87 mol% Co samples. Note the change in particle morphology.

provide an overview of the general particle population that allows one to conclude that no micron size particles are produced during LF-FSP of these materials.

TEMs are shown in Fig. 3. These images are, respectively, from the 8 and 87 mol% Co samples. Most of the particles are spherical and well below 80 nm in diameter, with the vast majority <30 nm. Note the change in morphology, which is mostly faceted and spherical for the 8 mol% sample (Fig. 3(a)), while nearly all particles in the 87 mol% sample (Fig. 3(b)) appear rhombic. This is attributed to the formation of the highly crystalline spinel phase coincident with increases in Co content. Particle necks, while occasionally visible in the 8 mol% sample, are not a major morphological feature. All samples prepared here consist primarily of soft agglomerates created during dispersion or from the strong electrostatic interactions that particles of this size exhibit. There is no evidence for any microporosity, as expected from the *t*-plot results and analyses.

XRDs for all samples are presented in Fig. 4. Figure 5 shows the relevant ICDD cards (CoO:43-1004, Co_3O_4:42-1467, $CoAl_2O_4$:44-0160, δ-Al_2O_3:46-1131, δ^*-Al_2O_3:46-1215). The phase composition changes gradually from δ-Al_2O_3 through the spinel phase to Co_3O_4.

The 4 mol% Co sample shows no trace of any Co-containing crystalline phase; thus, all of the Co^{3+} seems to substitute for Al^{3+} ions in the δ-Al_2O_3 lattice as expected based on our studies on rare-earth-doped δ-Al_2O_3.[41]

Samples with higher Co contents exhibit powder patterns corresponding to formation of $CoAl_2O_4$ spinel. These broad peaks first appear at 21 mol% Co and give way to sharper, better-defined peaks as the correct stoichiometry is reached. Stoichiometric cobalt aluminate shows a phase-pure pattern (ICDD ref.: 44-0160), indicative of the capabilities of LF-FSP. Figure 5 shows the compositions and the phases that are expected to form at these compositions. The formation of off-stoichiometric spinels (21 and 37 mol% samples) is believed to result from the extremely fast quench that these materials undergo in the LF-FSP apparatus. The shifts in the peak positions are indicative of a change in lattice cell parameters; however, in order to determine the exact atom positions in these materials, further studies are required.

In the 87 mol% Co sample, a CoO phase is detected as the excess Co^{3+} ions have no more sites to replace in the spinel structure. This phase is evident by a shift to higher 2θ°($\sim 0.8\theta$°) in the 220 reflection, and the emergence of a shoulder on the 400 reflection of $CoAl_2O_4$ and Co_3O_4. In the 94 mol% sample, the CoO phase is clearly evidenced by the emergence of the CoO 200 reflection ($\sim 42°$ 2θ) and the 220 reflection ($\sim 62°$ 2θ) Fig. 6.

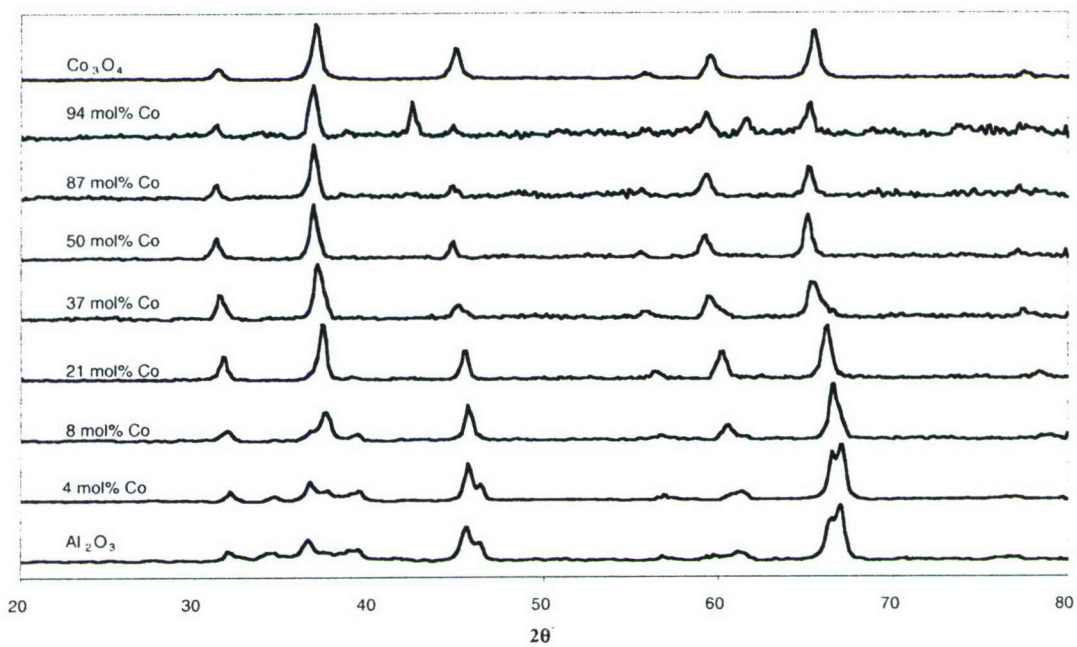

Fig. 4. X-ray diffraction of all as-prepared samples.

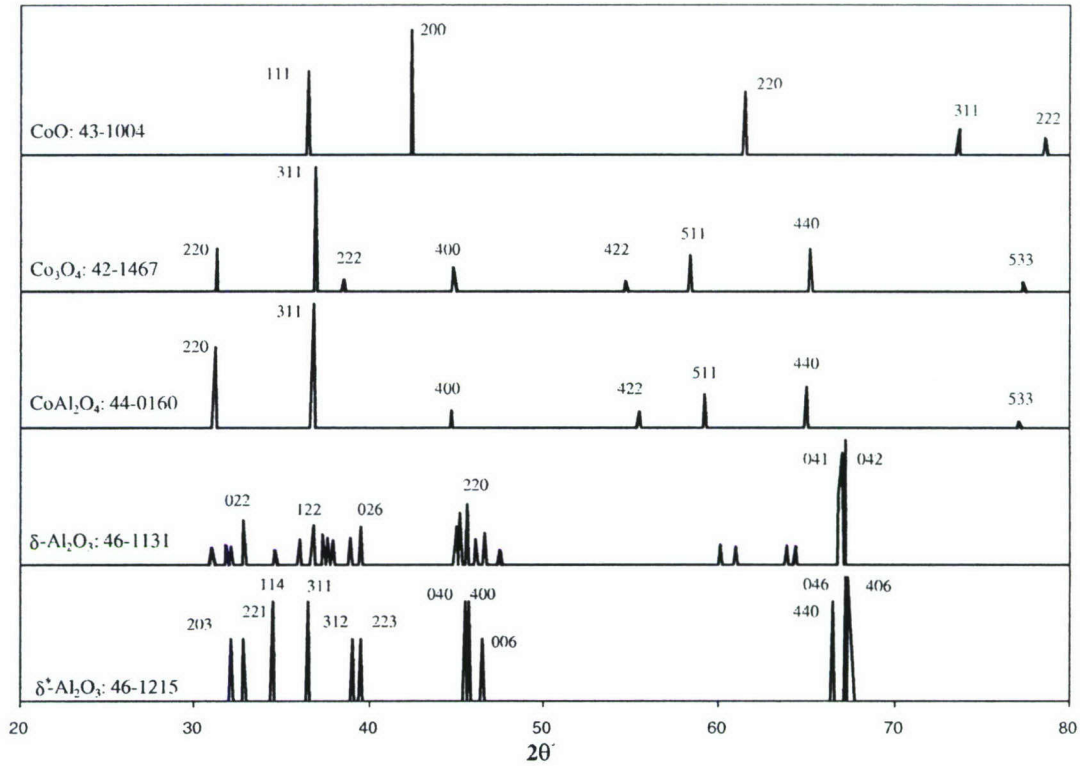

Fig. 5. Relevant ICDD files for the CoO_x–Al_2O_3 system.

The 94 mol% Co sample consists of a mixture of two phases, spinel $CoAl_2O_4$ and cubic CoO, as expected based on the elemental composition and the phase diagram.[42] The pure cobalt oxide XRD corresponds to Co_3O_4, which has a spinel structure from the ICDD card. We do not observe the thermodynamically expected cubic CoO because LF-FSP syntheses use O_2-rich atmospheres. The excess oxygen favors the formation of Co^{3+}, which in turn favors the formation of the spinel [Co_1(II)-Co_2(III)O_4] structure, detected by XRD.

TGA were performed on all as-prepared samples to determine the relative amounts of adsorbed surface species (H_2O and carbonate species) and thermal behavior. The 87, 94 mol% Co and Co_3O_4 show no mass loss events below ~900°C. At this temperature, these materials exhibit a sharp mass loss event that can be attributed to decomposition from Co_3O_4 to CoO:

$$2Co_3O_4 \rightarrow 6CoO + O_2 \quad (2)$$

The theoretical mass loss for such a reaction is 6.64%; the observed losses are 6.13, 6.02, and 6.09, respectively, for the 87, 94 mol% Co and Co_3O_4. These values are within the

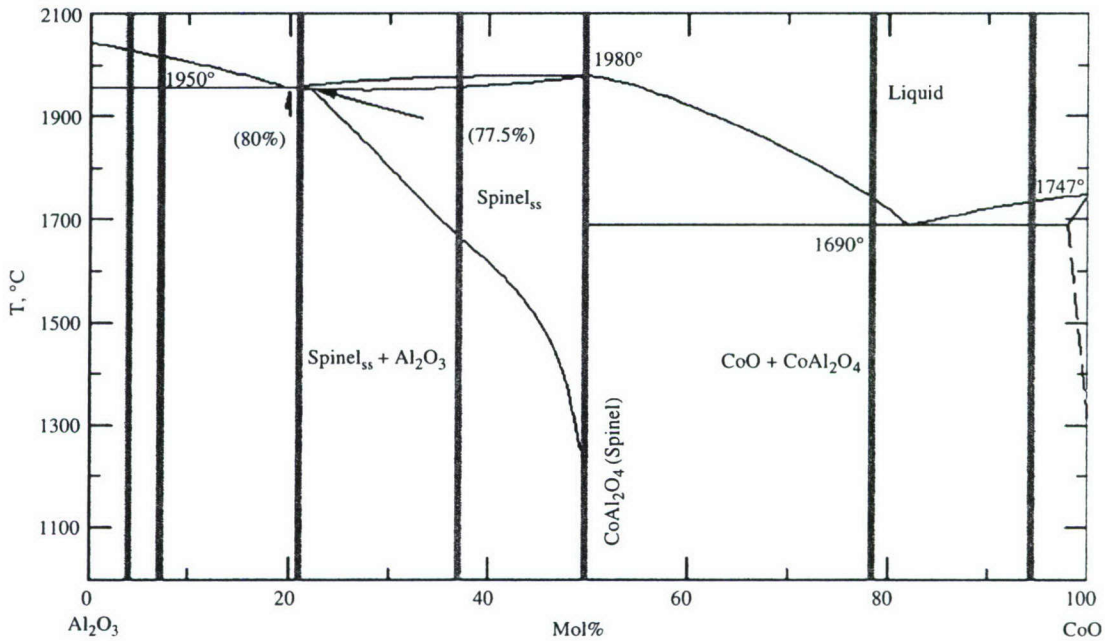

Fig. 6. Published phase field diagram for the CoO–Al_2O_3 system.[42]

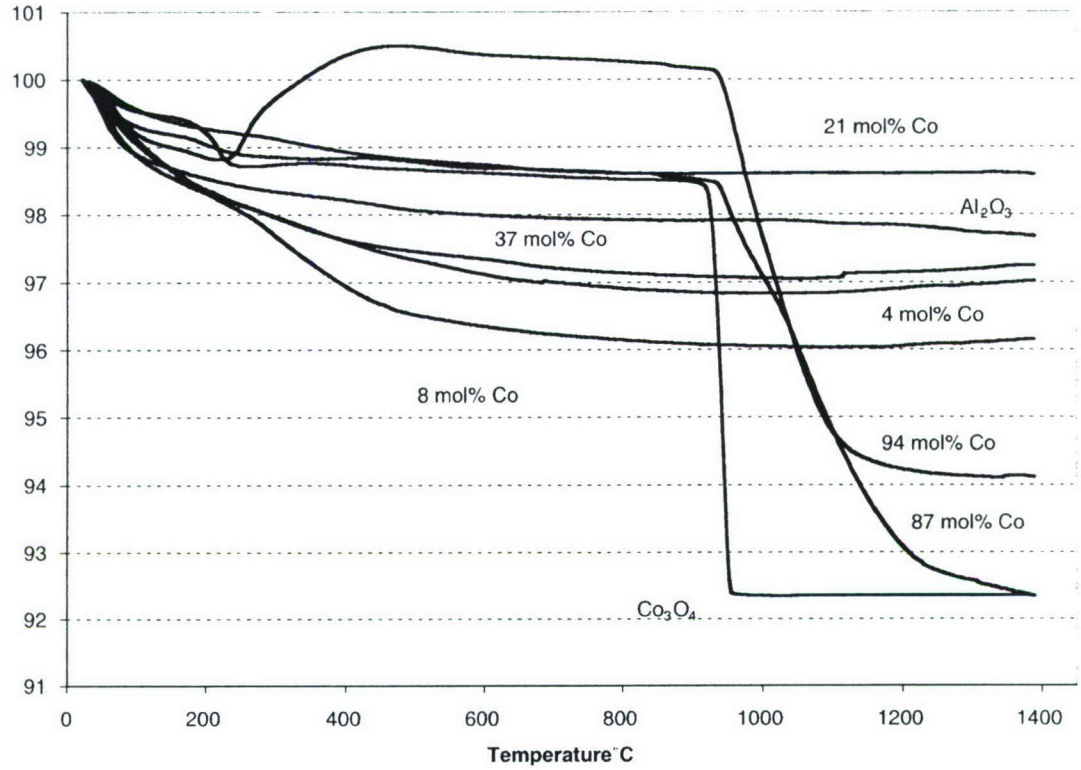

Fig. 7. Thermal behavior (10°C/min, 60 mL/min in air) for all as-prepared samples.

error limits of the analysis, given that these samples contain some CoO (see XRD analyses). The Co_3O_4 end member exhibits the sharpest mass loss event, which is observed to broaden at lower Co contents. One possible explanation is that oxygen is more tightly bound to nanopowders with some $CoAl_2O_4$ spinel phase present, although this was not confirmed here.

There is a small mass increase (0.5 wt%) between 240° and 450°C in the 94 mol% Co sample; we suspect that this increase results from oxidation of some CoO to Co_3O_4 or cobalt spinel. Such an oxidation might be expected for Co^{2+} ions substituted for octahedral Co^{3+} ions in the as-prepared material. These ions occupy traditional "B" sites in spinels that require a 3^+ charge to be stoichiometric.

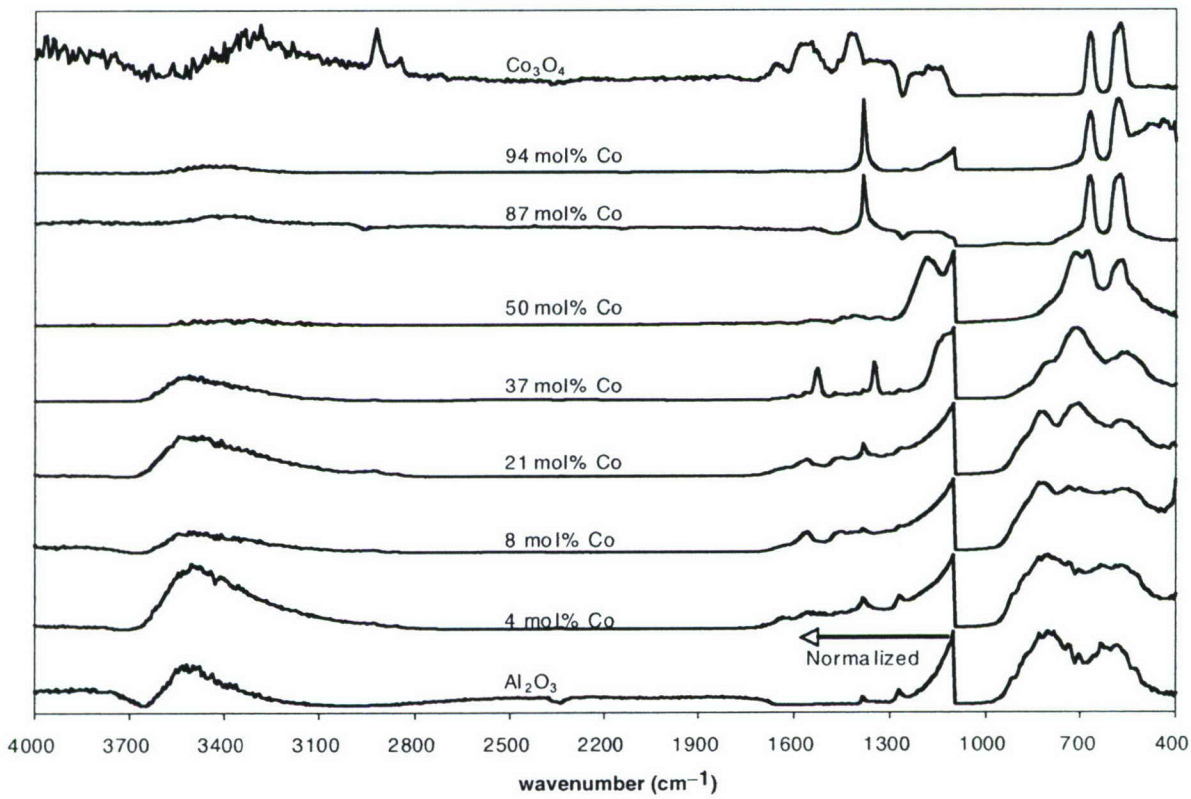

Fig. 8. Full FTIR spectra of all as-prepared samples.

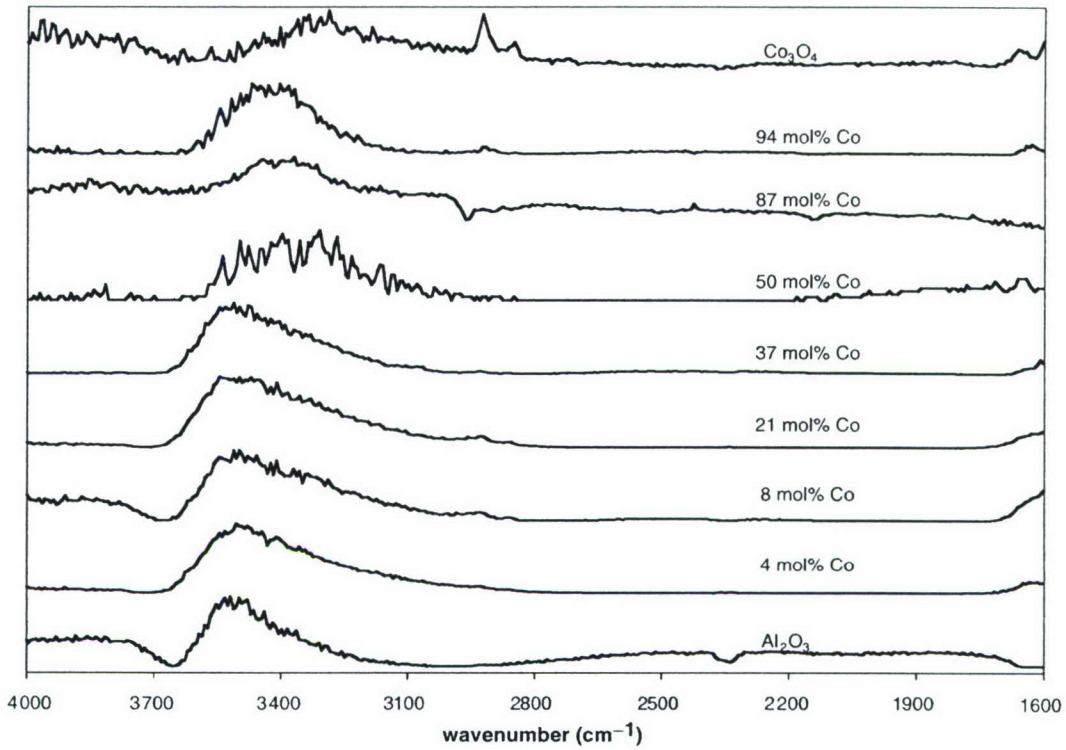

Fig. 9. FTIR spectra of all normalized samples in the 4000–1600 cm^{-1} region.

The other five samples exhibit typical 1%–4% mass losses (for nanopowders produced via LF-FSP) over the 1400°C range. This loss is expected and associated with loss of physi- and chemi-sorbed water resulting from the combustion process and atmosphere due to their relatively high surface areas, although they exhibit far less hydration than microporous powders.[43] The only sample that has a sharp mass loss event is Co_3O_4 at ~250°C; this event can be associated with loss of CO_2 or CO_3^{2-}.[33] DRIFTS data (discussed below) confirm the presence of organics.

DRIFTS for all samples are presented in Fig. 8. All spectra above 1200 cm^{-1} were normalized by taking the highest count in this range of any particular spectrum and normalizing this value to 1; this was done so that a fair comparison can be made among all spectra.

There are two main regions of interest: 4000–2800 and 1100–400 cm^{-1}. The first region, expanded in Fig. 9, reveals a series of overlapping ν–OH bands arising from both physi- and chemi-sorbed water. The higher ν–OH vibrations (3700–3200 cm^{-1}) are typical of overlapping hydroxyl groups on alumina surfaces.[44,45] There are no sharp peaks in this region, only broad bands. Furthermore, the νO–H bands fall off with increases in Co content, suggesting that the surface hydroxyls are only associated with the alumina species. With the exception of Co_3O_4, no significant organic species are observed as evidenced by the absence of νC–H bands in the 2900–2700 cm^{-1} region. These bands are associated with a 2% mass loss seen at >250°C in the TGA trace and could be a result of incomplete combustion of the precursor. However, this seems unlikely as they are not normally observed in any other nanopowders prepared previously and may be better explained as resulting from some steam reforming in the flame. But this conclusion remains speculative.

The lower wavenumber region exhibits typical νM–O bands. δ-alumina has two νAl–O bands at 810 and 610 cm^{-1},[46] associated with the tetrahedral and octahedral Al–O vibrations, respectively. Cobalt oxide (Co_3O_4) has two well-defined νM–O bands, 690 and 605 cm^{-1},[47] which emerge clearly in the higher Co content samples. These sharp bands become visible in sample 7:87 mol% Co, and are associated with the high degree of crystallinity of these samples.

IV. Conclusions

LF-FSP offers the opportunity to produce mixed-metal oxide nanopowders with exceptional control of stoichiometry, phase, and phase purity. Here, we demonstrate the use of LF-FSP to produce combinatorially a series of nine powders along the CoO_x–Al_2O_3 tie line with well-defined stoichiometries. The precursors used to synthesize these nanopowders are inexpensive and can be easily prepared.

We find that along the CoO_x–Al_2O_3 tie line, increases in Co content steadily reduce the SSAs by as much as 65% (from 60 to 20 m^2/g), likely as a consequence of the formation of the cobalt spinel phase. Particle sizes (from XRD data) vary very little; the BET-derived APS values are slightly higher most likely because of miscalculations in the true particle densities. The unexpected SSA increase observed for the end-member cobalt oxide is attributed to the formation of Co_3O_4 instead of CoO. The most probable explanation for this result is that the excess oxygen used in the LF-FSP process favors formation of Co^{3+}, which in turn favors the formation of a spinel [Co_1(II)Co_2(III)O_4] structure. We also detected cobalt aluminate spinel phases that should only be stable at high temperatures, but found they were metastable at lower temperatures. Therefore we can conclude that LF-FSP offers access to kinetic phases rather than the thermodynamic phases accessible by standard processing techniques.

For the most part, TGA and FTIR studies provide results that correspond to typical nanopowders produced via LF-FSP. These materials exhibit typical 1%–4% mass losses over the 1400°C range, with only physi- and chemisorbed water as a surface species. Carbonate species, often detected on the surfaces of LF-FSP powders, here Co_3O_4, yield mass loss events at ~250°C attributed to elimination of CO_2. The sharp mass loss event of the high cobalt content samples likely results from decomposition of Co_3O_4 to CoO but is at present only speculation.

References

[1]S. Ucar, S. Karagoz, T. Karayildirim, and J. Yanik, "Conversion of Polymers to Fuels in a Refinery Stream," *Polym. Degrad. Stabil.*, **75**, 161–71 (2002).

[2]J. Rodriguez, C. Guimon, A. J. Marchi, A. Borgna, and A. Monzon, "Activity, Selectivity and Coking of Bimetallic Ni–Co-Spinel Catalysts in Selective Hydrogenation Reactions," *Stud. Surf. Sci. Catal.*, **111**, 183–90 (1997).

[3]P. Thormahlen, E. Fridell, N. Cruise, M. Skoglundh, and A. Palmqvist, "The Influence of CO_2, C_3H_6, NO, H_2, H_2O or SO_2 on the Low-Temperature Oxidation of CO on a Cobalt–Aluminate Spinel Catalyst ($Co_{1.66}Al_{1.34}O_4$)," *Appl. Catal. B-Environ.*, **31** [1] 1–12 (2001).

[4]J. Llorca, P. D. Ramiirez De La Piscina, J.-A. Dalmon, and N. Homs, "Transformation of Co_3O_4 During Ethanol Steam-Re-Forming. Activation Process for Hydrogen Production," *Chem. Mater.*, **16**, 3573–8 (2004).

[5]F. Grillo, M. M. Natile, and A. Glisenti, "Low Temperature Oxidation of Carbon Monoxide: The Influence of Water and Oxygen on the Reactivity of a Co_3O_4 Powder Surface," *Appl. Catal. B-Environ.*, **48**, 267–74 (2004).

[6]L. B. Backman, A. Rautiainen, M. Lindblad, and A. O. I. Krause, "Effect of Support and Calcination on the Properties of Cobalt Catalysts Prepared by Gas Phase Deposition," *Appl. Catal. A-Gen.*, **191** [1–2] 55–68 (2000).

[7]S. Karagoz, T. Karayildirim, S. Ucar, M. Yukselc, and J. Yanikb, "Liquefaction of Municipal Waste Plastics in VGO Over Acidic and Non-Acidic Catalysts," *Fuel*, **82**, 415–23 (2003).

[8]A. Hadi and I. Yaacob, "Synthesis of PdO/CeO_2 Mixed Oxides Catalyst for Automotive Exhaust Emissions Control," *Catal. Today*, **96** [3] 165–70 (2004).

[9]T. Kanazawa, "Development of Hydrocarbon Adsorbents, Oxygen Storage Materials for Three-Way Catalysts and NO_x Storage-Reduction Catalyst," *Catal. Today*, **96** [3] 171–7 (2004).

[10]M. Richter, M. Langpape, S. Kolf, G. Grubert, R. Eckelt, J. Radnik, M. Schneider, M. M. Pohl, and R. Fricke, "Combinatorial Preparation and High-Throughput Catalytic Tests of Multi-Component deNO_x Catalysts," *Appl. Catal. B-Environ.*, **36** [4] 261–77 (2002).

[11]S. Matsumoto, "Recent Advances in Automobile Exhaust Catalysts," *Catal. Today*, **90** [3–4] 183–90 (2004).

[12]J. Li, J. Hao, L. Fu, T. Zhu, Z. Liu, and X. Cui, "Cooperation of Pt/Al_2O_3 and In/Al_2O_3 Catalysts for NO Reduction by Propene in Lean Burn Condition," *Appl. Catal. A-Gen.*, **265** [1] 43–52 (2004).

[13]P. Colomban, "Lapis Lazuli as Unexpected Blue Pigment in Iranian Lajvardina Ceramics," *J. Raman Spectrosc.*, **34** [6] 420–3 (2003).

[14]C. Roldan, J. Coll, J. L. Ferrero, and D. Juanes, "Identification of Overglaze and Underglaze Cobalt Decoration of Ceramics from Valencia (Spain) by Portable EDXRF Spectrometry," *X-ray Spectrom.*, **33** [1] 28–32 (2004).

[15]L. Koroleva, "Synthesis of Spinel-Based Ceramic Pigments from Hydroxycarbonates," *Glass Ceram.*, **61** [9–10] 299–302 (2004).

[16]S. Djambazov, Y. Ivanova, A. Yoleva, and N. Nedelchev, "Ceramic Pigments on the Base of the CoO–ZnO-SiO_2 System Obtained by a Sol–Gel Method," *Ceram. Int.*, **24** [4] 281–4 (1998).

[17]J. Merikhi, H.-O. Jungk, and C. Feldmann, "Sub-Micrometer $CoAl_2O_4$ Pigment Particles—Synthesis and Preparation of Coatings," *J. Mater. Chem.*, **10**, 1211–314 (2000).

[18]T. Junru, H. Yunfang, H. Wenxiang, C. Xiuzeng, and F. Xiansong, "The Preparation and Characteristics of Cobalt Blue Mica Coated Titania Pearlescent Pigment," *Dyes Pigm.*, **52** [3] 215–22 (2002).

[19]M. Llusar, A. Fores, J. A. Badenes, J. Calbo, M. A. Tena, and G. Monros, "Colour Analysis of Some Cobalt-Based Blue Pigments," *J. Eur. Ceram. Soc.*, **21** [8] 1121–30 (2001).

[20]Z.-Z. Chen, E.-W. Shi, W.-J. Li, Y.-Q. Zheng, and W.-Z. Zhong, "Hydrothermal Synthesis and Optical Property of Nano-Sized $CoAl_2O_4$ Pigment," *Mater. Lett.*, **55** [5] 281–4 (2002).

[21]M. P. Morales, S. A. Walton, L. S. Prichard, C. J. Serna, D. P. E. Dickson, and K. O'grady, "Characterisation of Advanced Metal Particle Recording Media Pigments," *J. Magn. Magn. Mater.*, **190**, 357–70 (1998).

[22]C. O. Arean, M. P. Mentruit, E. E. Platero, F. X. L. I. Xamena, and J. B. Parra, "Sol–Gel Method for Preparing High Surface Area $CoAl_2O_4$ and Al_2O_3–$CoAl_2O_4$ Spinels," *Mater. Lett.*, **39**, 22–7 (1999).

[23]F. Meyer, A. Dierstein, C. Beck, W. Hartl, R. Hempelmann, S. Mathur, and M. Veith, "Size-Controlled Synthesis of Nanoscaled Aluminium Spinels Using Heterobimetallic Alkoxide Precursors Via Water/Oil Microemulsions," *Nanostruct. Mater.*, **12**, 71–4 (1999).

[24]N. Ouahdi, S. Guillemet, J. J. Demai, B. Durand, L. Er Rakho, R. Moussa, and A. Samdi, "Investigation of the Reactivity of $AlCl_3$ and $CoCl_2$ Toward Molten Alkali-Metal Nitrates in Order to Synthesize $CoAl_2O_4$," *Mater. Lett.*, **59** [2–3] 334–40 (2005).

[25]S. Chokkaram, R. Srinivasan, D. R. Milburn, and B. H. Davis, "Conversion of 2-Octanol Over Nickel–Alumina, Cobalt–Alumina, and Alumina Catalysts," *J. Mol. Catal. A-Chem.*, **121**, 157–69 (1997).

[26]Z.-Z. Chen, E. W. Shi, W.-J. Li, Y.-Q. Zheng, J.-Y. Zhuang, B. Xiao, and L.-A. Tang, "Preparation of Nanosized Cobalt Aluminate Powders by a Hydrothermal Method," *Mater. Sci. Eng. B-Solid*, **107**, 217–23 (2004).

[27]W.-S. Cho and M. Kakihana, "Crystallization of Ceramic Pigment $CoAl_2O_4$ Nanocrystals From Co–Al Metal Organic Precursor," *J. Alloy Compounds*, **287** [1–2] 87–90 (1999).

[28]V. Dureuil, C. Ricolleau, M. Gandais, C. Grigis, J. P. Lacharme, and A. Naudon, "Growth and Morphology of Cobalt Nanoparticles on Alumina," *J. Cryst. Growth*, **233**, 737–48 (2001).

[29]a. W. Stark, L. Madler, M. Maciejewski, S. Pratsinis, and A. Baiker, "Flame Synthesis of Nanocrystalline Ceria–Zirconia: Effect of Carrier Liquid," *Chem. Commun.*, [5] 588–9 (2003). b. A. Camenzind, R. Strobel, and S. E. Pratsinis, "Cubic or Monoclinic Y_2O_3:Eu^{3+} Nanoparticles by One Step Flame Spray Pyrolysis," *Chem. Phys. Lett.*, **415**, 193–7 (2005). c. R. Mueller, R. Jossen, H. K. Kammler, S. E. Pratsinis, and M. K. Akhtar, "Growth of Zirconia Particles Made by Flame Spray Pyrolysis," *J. AIChE*, **50**, 3085–94 (2004). d. R. Mueller, R. Jossen, S. E. Pratsinis, M. Watson, and M. K. Akhtar, "Zirconia Nanoparticles Made in Spray Flames at High Production Rates," *J. Am. Ceram. Soc.*, **87**, 197–202 (2004).

[30]L. S. Wang, Y. H. Zhou, Z. W. Quan, and J. Lin, "Formation Mechanisms and Morphology Dependent Luminescence Properties of Y_2O_3: Eu Phosphors Prepared by Spray Pyrolysis Process," *Mater. Lett.*, **59** [10] 1130–3 (2005).

[31]a. R. M. Laine, K. Waldner, C. Bickmore, and D. R. Treadwell, "Ultrafine Powders by Flame Spray Pyrolysis," U.S. patent 5,958,361, September 28, 1999. b. R. M. Laine, S. C. Rand, T. Hinklin, and G. Williams, "Ultrafine Powders as Lasing Media," International patent application allowed. WO 0038282 H01S 20000629. c. A. C. Sutorik, R. M. Laine, J. Marchal, T. Johns, and T. Hinklin, "Mixed-Metal Oxide Particles by Liquid Feed-Flame Spray Pyrolysis of Oxide Precursors in Oxygenated Solvents," WO03070640 issued 2003-08-28. U.S. Patent issued.

[32]C. R. Bickmore, K. F. Waldner, D. R. Treadwell, and R. M. Laine, "Ultrafine Spinel Powders by Flame Spray Pyrolysis of a Magnesium Aluminum Double Alkoxide," *J. Am. Ceram. Soc.*, **79** [5] 1419–23 (1996).

[33]J. Marchal, T. John, R. Baranwal, T. Hinklin, and R. M. Laine, "Yttrium Aluminum Garnet Nanopowders Produced by Liquid-Feed Flame Spray Pyrolysis (LF-FSP) of Metalloorganic Precursors," *Chem. Mater.*, **16** [5] 822–31 (2004).

[34]D. R. Treadwell, A. C. Sutorik, S. S. Neo, R. M. Laine, and R. Svedberg, "Synthesis of Beta″-Alumina Polymer Precursor and Ultrafine Beta″–Alumina Composition Powders," *Acs. Sym. Ser.*, **681**, 146–56 (1998).

[35]R. Baranwal, M. P. Villar, R. Garcia, and R. M. Laine, "Flame Spray Pyrolysis of Precursors as a Route to Nano-Mullite Powder: Powder Characterization and Sintering Behavior," *J. Am. Ceram. Soc.*, **84** [5] 951–61 (2001).

[36]S. M. Redmond, G. L. Armstrong, H. Y. Chan, E. Mattson, A. Mock, B. Li, J. R. Potts, M. Cui, S. C. Rand, S. L. Oliveira, J. Marchal, T. Hinklin, and R. M. Laine, "Electrical Generation of Stationary Light in Random Scattering Media," *J. Opt. Soc. Am. B*, **21** [1] 214–22 (2004).

[37]G. R. Williams, S. B. Bayram, S. C. Rand, T. Hinklin, and R. M. Laine, "Laser Action in Strongly Scattering Rare-Earth-Metal-Doped Dielectric Nanophosphors," *Phys. Rev. A*, **65** [1] 13807–12 (2002).

[38]S. Kim, J. J. Gislason, R. W. Morton, X. Q. Pan, H. P. Sun, and R. M. Laine, "Liquid-Feed Flame Spray Pyrolysis of Nanopowders in the Alumina–Titania System," *Chem. Mater.*, **16** [12] 2336–43 (2004).

[39]J. Azurdia, J. C. Marchal, P. Shea, H. Sun, X. Q. Pan, and R. M. Laine, "Liquid-Feed Flame Spray Pyrolysis (LF-FSP) as a Method of Producing Mixed-Metal Oxide Nanopowders of Potential Interest as Catalytic Materials. Nanopowders Along the NiO–Al_2O_3 Tie-Line Including $(NiO)_{0.22}(Al_2O_3)_{0.78}$, A New Inverse Spinel Composition," *Chem. Mater.*, **18** [3] 731–9 (2006).

[40]K. F. Waldner, R. M. Laine, S. Dhumrongvaraporn, S. Tayaniphan, and R. Narayanan, "Synthesis of a Double Alkoxide Precursor to Spinel ($MgAl_2O_4$) Directly from $Al(OH)_3$, MgO, and Triethanolamine and its Pyrolytic Transformation to Spinel," *Chem. Mater.*, **8** [12] 2850–7 (1996).

[41]T. Hinklin, B. Toury, C. Gervais, F. Babonneau, J. J. Gislason, R. W. Morton, and R. M. Laine, "Liquid-Feed Flame Spray Pyrolysis of Metalloorganic and Inorganic Alumina Sources in the Production of Nanoalumina Powders," *Chem. Mater.*, **16** [1] 21–30 (2004).

[42]T. Mori, "Phase Diagram of the System Cobalt(II) Oxide–Aluminum Oxide," *Nippon. Seram. Kyokai. Gakkaishi*, **90** [2] 100–1 (1982).

[43]J. M. Mchale, A. Navrotsky, and A. J. Perrotta, "Effects of Increased Surface Area and Chemisorbed H_2O on the Relative Stability of Nanocrystalline -Al_2O_3 and -Al_2O_3," *J. Phys. Chem. B*, **101** [4] 603–13 (1997).

[44]D. H. Lee and S. Condrate, "An FTIR Spectral Investigation of the Structural Species Found on Alumina Surfaces," *Mater. Lett.*, **23** [4–6] 241–6 (1995).

[45]J. M. Saniger, "Al–O Infrared Vibrational Frequencies of [Gamma]-Alumina," *Mater. Lett.*, **22** [1–2] 109–13 (1995).

[46]P. Tarte, "Infra-Red Spectra of Inorganic Aluminates and Characteristic Vibrational Frequencies of AlO_4 Tetrahedra and AlO_6 Octahedra," *Spectrochim. Acta A-M*, **23** [7] 2127–43 (1967).

[47]P. Nkeng, J.-F. Koenig, J. L. Gautier, P. Chartier, and G. Poillerat, "Enhancement of Surface Areas of Co_3O_4 and $NiCo_2O_4$ Electrocatalysts Prepared by Spray Pyrolysis," *J. Electroanal. Chem.*, **402**, 81–9 (1996). □

Journal of Ceramic Processing Research. Vol. 8, No. 2, pp. 129~136 (2007)

J O U R N A L O F
Ceramic Processing Research

Liquid-feed flame spray pyrolysis (LF-FSP) for combinatorial processing of nanooxide powders along the $(ZrO_2)_{1-x}(Al_2O_3)_x$ tie-line. Phase segregation and the formation of core-shell nanoparticles

Min Kim and Richard M. Laine*

Department of Materials Science and Engineering, University of Michigan, Ann Arbor, MI 48109-2136

We report here the synthesis of $(ZrO_2)_{1-x}(Al_2O_3)_x$ nanooxide powders with molar ratios that span the ZrO_2-Al_2O_3 composition range. Liquid-feed flame spray pyrolysis (LF-FSP) of mixtures of $N(CH_2CH_2O)_3Al$ (alumatrane) and $Zr(CH_3CH_2COO)_2(OH)_2$ precursors dissolved in ethanol, were aerosolized with O_2, combusted at temperatures of 1500-2000°C and rapidly quenched thereafter to provide $(ZrO_2)_{1-x}(Al_2O_3)_x$ nanopowders of selected compositions. All powders exhibit average particle sizes (APSs) < 20 nm and corresponding surface areas of ≈50 m^2/g when produced at rates of 100-300 g/h. The as-processed powders were characterized in terms of phase, APS, specific surface area, composition, and morphology by BET, XRD, XRF, SEM, TEM, FT-IR, and TGA-DTA. The presence of δ-alumina and tetragonal zirconia is observed over most of the compositions studied. Furthermore, this phase segregation leads to the formation of core-shell materials. Evidence is presented suggesting the incorporation of $Zr^{2+/3+}$ ions above the published solubility limit of ZrO_2 in δ-alumina.

Key words: core-shell nanoparticles, liquid-feed flame spray pyrolysis, $(ZrO_2)_{1-x}(Al_2O_3)_x$ nanopowders, $(ZrO_2)_{1-x}(Al_2O_3)_x$ tie-line, phase-separated nanopowders.

Introduction

Zirconia is an important material for a wide range of applications [1, 2]. Besides its traditional uses in refractory ceramics and abrasion-resistant materials, high-surface area zirconia is used in applications ranging from catalysts [3] to oxygen sensors [4], to solid oxide fuel cells (oxygen electrolyte) [5] to gate dielectrics for MOSFET [6, 8]. Zirconia has a high dielectric constant (~25), a wide energy band gap (7.8 eV), and when alloyed with ceria as the oxygen storage media in three way auto exhaust catalytic converters, TWCs, it greatly improves sinter resistance [3-7]. Doping zirconia with yttria (YSZ) or alumina (ZTA) to stablize the tetragonal phase, provides unusual toughening for a wide variety of mechanical applications. ZTA materials combine high flexural strength (~910 MPa) and hardness (~15 GPa) with good fracture toughness (~7 MPa $m^{1/2}$) [8, 9]. Unfortunately ZTA's very useful high temperature properties also contribute to difficulties in its processing to dense, defect-free composite materials [10, 11].

We have developed a new approach to high surface area, micropore free, mixed-metal oxide nanopowders using liquid-feed flame spray pyrolysis (LF-FSP). LF-FSP offers the potential to make a wide variety of single and mixed-metal oxide nanopowders in a single step [12-18]. The LF-FSP process aerosolizes metallo-organic precursors dissolved in an alcohol solvent with O_2, combusts the aerosol within a quartz chamber at 1500-2000 °C, and then rapidly quenches the gaseous species to produce nanosize oxide "soot" with compositions identical to those in the starting metallo-organic precursors. See the experimental section below for details.

In previous studies we have used LF-FSP to make phase-pure nanopowders of single metal oxides including Al_2O_3, CeO_2, ZrO_2 and NiO [12-18]. These LF-FSP nanopowders are unaggregated and as-produced are without microporosity at surface areas of 30-50 m^2/g and average particle sizes (APSs) of 15-30 nm. We have also made binary metal oxide nanopowders along the $(MO_z)_{1-x}(Al_2O_3)_x$ tielines were M=Ni, Ti, Co, Mg, Cu, Zn and Ce by LF-FSP [15-18]. The majority of these nanopowders are solid solutions without microporosity with SSAs of 45-70 m^2/g and APSs of 15-35 nm.

LF-FSP provides easy access to many types of nanopowders with excellent control of phase purity and morphology. Furthermore, LF-FSP processing provides low-cost, easy and precise compositional (combinatorial) control to versatile nanomaterials in mixed-metal oxide systems using one-step processing. These nanopowders in turn offer potential access to a wide variety of materials for catalytic, mechanical, photonic and electrical applications.

The potential to make highly homogeneous ZTA nanopowders that offer relatively easy access to high strength monolithic ZTA components provides motivation

*Corresponding author:
Tel : 1-734-764-6203
Fax: 1-734-763-4788
E-mail: talsdad@umich.edu

for the work reported here. Additional motivation comes from the potential to create ZTA nanocomposites amenable to superplastic deformation [19]. Finally, the studies reported when combined with work on $[(CeO_2)_{1-x}$-$(ZrO_2)_x]_{1-y}(Al_2O_3)_y$ to be described elsewhere [20], suggest a potential for one step processing of the washcoats used in TWCs.

Unlike many of the nanopowders previously produced by LF-FSP processing by us and others [7-9, 24, 25], LF-FSP processing of materials along the $(ZrO_2)_x$-$(Al_2O_3)_{1-x}$ tieline does not produce solid solutions but nanocomposites of each composition. As with other LF-FSP products, the resulting unaggregated nanopowders offer specific surface areas (SSAs) ≥ 45 m^2/g without microporosity and although not yttria stabilized, the only zirconia phase observed is tetragonal over all compositions studied.

Experimental

Liquid-feed flame spray pyrolysis (LF-FSP)

LF-FSP, invented at the University of Michigan, has been described in more detail in published papers [12-18]. Briefly, alcohol (typically EtOH) solutions containing 1-10 wt % loading of ceramic as precursors, e.g. single-or mixed-metal alkoxides, carboxylates or β-diketonates are aerosolized with O_2 into a quartz chamber where it is ignited with methane pilot torches.

Initial combustion temperatures run 1500°-2000 °C, depending on the processing conditions, generating nanopowder "soot". Temperatures drop to 300-500 °C over 1.5 metre, equivalent to a 1000 °C quench in 100 ms leading to kinetic products and nanopowders that are largely unaggregated; although they are lightly agglomerated. "Shooting" rates can be 200 g/h when using wire-in-tube electrostatic precipitators operating at 10 kV. Typical powders are 15 to 100 nm APS with specific surface areas (SSAs) of 30 to 100 m^2/g. When combinations of elements are used, the resulting nanopowders will have compositions identical to those of the precursor solutions. Since compositions of chemical solutions can be changed intentionally, potentially even during mixing just before aerosolization, it becomes possible to combinatorially produce mixed-metal oxide materials. Hence it becomes possible to rapidly optimize materials for given properties or for ease of processing.

Materials

– Alumatrane

$N(CH_2CH_2O)_3Al$ prepared as described previously [21, 22] is used as the alumina source.

– Zirconium propionate

Zirconium carbonate $[2ZrO_2(CO_2)\cdot x(H_2O)$, 99%, 150 g, 0.34 mole] was reacted with excess propionic acid (500 ml, 6.80 mole) in a 1 l flask equipped with a still head and an addition funnel. N_2 was sparged directly through the solution (13.7 KPa pressure) as the solution was heated at 120 °C/2 h with magnetic stirring to distill off ~150 ml of liquid (water and propionic acid). The ceramic loading of the resulting precursor was 11 wt% as determined by TGA.

XRD studies

As-prepared samples were characterized using a Rigaku Rotating Anode Goniometer. Powder samples were prepared by placing ≈100 mg in XRD sample holders (amorphous silica slides) for data collection. CuKα (λ= 1.54 Å) radiation with a Ni filter was used with a working voltage and current of 40 kV and 100 mA, respectively. Scans were continuous from 5-90° 2θ with a step scan of 2° 2θ/minute in increments of 0.05° 2θ. Peak positions and relative intensities were characterized by comparison with PDF files of standard materials: ZrO_2 (PDF file 42-1164), δ-Al_2O_3 (PDF file 46-1131) Debye-Scherrer line broadening was used to calculate average particle sizes from the XRD powder patterns.

Thermal Gravimetric Analysis and Differential Thermal Analysis (TGA/DTA)

TGA-DTA was performed using a SDT 2960 Simultaneous Differential Thermal Analyzer (TA Instruments, Inc., New Castle, DE). The instrument was calibrated with gold supplied by Perkin-Elmer. Samples (70 mg) of as-prepared powders were hand pressed in a 3 mm dual action die and placed inside Pt sample cups and heated at ramp rates of 10 K/minute from ambient temperature to 1400 °C. The reference material was a pellet of α-alumina. A flow of synthetic air, 50 ml/minute, was maintained during all experiments.

Specific surface area (SSA).

SSA was measured on a Micromeritics ASAP 2000 sorption analyzer. Samples (200 mg) were degassed at 400 °C until the outgas rate was 5 mmHg/minute. Analyses was run at 77 K with N_2. SSAs were determined by the BET multipoint method using at least five data points. The average particle size was derived using the formula $\langle R \rangle = (3/\rho \times SSA)$ where $\langle R \rangle$ = average particle size, and ρ is the density of the material.

Scanning electron microscopy (SEM)

A field emission SEM (Phillips XL30FEG) was used to image powder morphologies. Powder samples were dispersed in distilled H_2O using an ultrasonic horn (Vibra-cell, Sonics and Materials, Inc., Newton, CT). A drop of the dispersed powder/water was placed on an aluminum SEM stub and allowed to dry for 4 h on a hot plate. Powders were sputter coated with 10-40 nm of Au-Pd to reduce charging effects. Operating voltage was between 15.0 and 30.0 kV.

Transmission electron microscopy (TEM)

An analytical high resolution TEM (Model 3011, JOEL, Osaka, Japan) was used to measure the particle

sizes and morphologies of as-prepared powders. Powder samples were prepared by dipping a holey carbon grid in a vial of emulsion with as-prepared powder. The specimen was held in a Gatan double tilt goniometer. An operating voltage of 300 kV was used.

FT-IR Spectra

Diffuse reflectance Fourier transform (DRIFT) spectra were recorded on a Mattson Galaxy Series FTIR 3000 spectrometer (Mattson Instruments, Inc., Madison, WI). Optical grade, random cuttings of KBr (International Crystal Laboratories, Garfield, NJ) were ground, with 1.0 wt % of the sample to be analyzed. For DRIFT analysis, samples were packed firmly and leveled off at the upper edge to provide a smooth surface. For transmission IR, 100 mg of each sample prepared for DRIFT analysis was pressed in a stainless steel double action die (12.75 mm diameter) at 100 MPa for 1 minute in a Carver Press (model 3912). Fresh backgrounds of pure KBr were done every 2 hour. The FTIR sample chamber was flushed continuously with N_2 prior to data acquisition in the range 4000-400 cm^{-1}. Each run consisted of 128 scans with a resolution of ± 8 cm^{-1}.

Results and Discussion

In the following sections we begin by characterizing the zirconia precursor developed for LF-FSP processing. Thereafter we follow with sections on the production of selected nanopowders along the $(ZrO_2)_{1-x}(Al_2O_3)_x$ tieline, their phase behavior, particle morphologies, surface chemistries and thermal properties.

Precursor and precursor formation

We previously reported the characterization of alumatrane [$N(CH_2CH_2O)_3Al$] and its use as a precursor in LF-FSP for the synthesis of δ-alumina nanopowders [12, 16, 21, 22]. Here we report on the zirconium precursor, $Zr(CH_3CH_2COO)_2(OH)_2$, synthesized as discussed in the experimental section. This precursor has a thermal decomposition pattern similar to other metal carboxylate precursors studied previously [12-18].

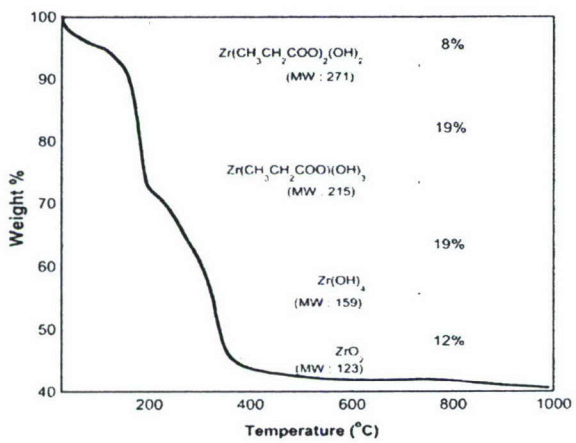

Fig. 1. TGA of $Zr(CH_3CH_2COO)_2(OH)_2$ ramped at 10 °C/min in synthetic air.

Figure 1 shows a TGA trace for $Zr(CH_3CH_2COO)_2(OH)_2$. Initial mass losses (8%) are due to propionic acid of recrystallization. Thereafter, mass loss events are attributed to the decomposition of the propionate ligands as suggested in reactions (1)-(3) [12-18, 21, 22].

$$Zr(CH_3CH_2COO)_2(OH)_2 \rightarrow Zr(CH_3CH_2COO)(OH)_3+CH_3CH=C=O \quad (1)$$

Calc. (Found) Mass Loss = 19.01% (19%)

$$Zr(CH_3CH_2COO)(OH)_3 \rightarrow Zr(OH)_4+CH_3CH=C=O \quad (2)$$

Calc. (Found) Mass Loss = 19.01% (19%)

$$Zr(OH)_4 \rightarrow ZrO_2+2H_2O \quad (3)$$

Calc. (Found) Mass Loss = 12.22% (12%)

Final ceramic yields [42% (ZrO_2)] are within experimental error of the calculated value (41.75%) from the decomposition of the precursor [$Zr(CH_3CH_2COO)_2(OH)_2$] to oxide (ZrO_2) and are as expected based on previous studies [12-18, 21, 22].

Compositions of as-processed nanopowders

Eight different precursor compositions in the $(ZrO_2)_x$-$(Al_2O_3)_{1-x}$ system were prepared by making simple mixtures of alumatrane and the propionate as detailed in the Experimental. Table 1 lists the compositions of the LF-FSP produced nanopowders. Compositions were confirmed by XRF. These nanopowders were analyzed by XRD, SEM, FT-IR and TGA-DTA as discussed in the following sections.

XRD powder pattern studies

Figure 2 provides XRD patterns for as-produced nanopowders along the $(ZrO_2)_x(Al_2O_3)_{1-x}$ tie-line (Table 1). In contrast to previous studies discussed above, we observe what appears to be complete phase separation as indicated by the presence of t-zirconia and δ-alumina in Samples 2-7, Table 1.

It is important to note that two excellent papers from

Table 1. Compositions of the $(ZrO_2)_x(Al_2O_3)_{1-x}$ nanopowders.

Sample	Mole % ZrO_2	Wt % ZrO_2	Mole % Al_2O_3
1	2.4	3.0	96.8
2	4.1	5.0	94.9
3	4.6	5.6	94.3
4	5.9	7.1	92.8
5	8.4	10.0	90.0
6	13.6	16.0	93.9
7	49.7	54.5	45.4
8	79.4	82.4	17.6

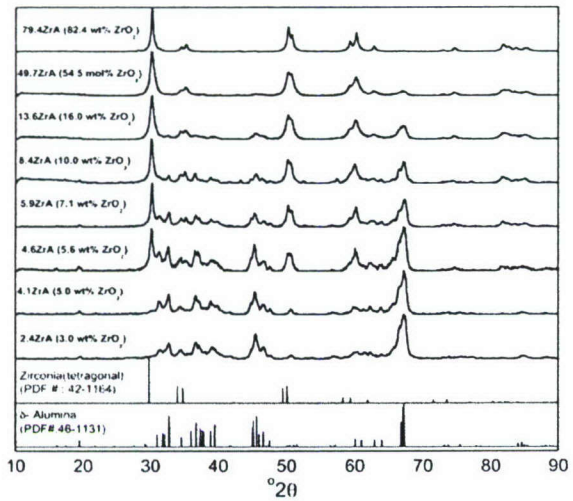

Fig. 2. XRD powder patterns of $(ZrO_2)_x(Al_2O_3)_{1-x}$. 2.4 ZrA denotes 2.4 mole % ZrO_2 included in ZrO_2-Al_2O_3 binary system.

the Hahn and Winterer groups on low alumina content zirconias [23, 24], made by a process similar to LF-FSP have recently been published that corroborate our observations in this region of the tieline. Thus, their XRD studies of zirconia rich samples in $(ZrO_2)_x(Al_2O_3)_{1-x}$ at x=0.5 - 1.0 indicate that the tetragonal phase is dominant in the zirconia-rich region as seen for 49.7 ZrA and 79.4 ZrA with the minor phase being δ-alumina. They also briefly mention the formation of a transition alumina phase but did not characterize it.

Average particle size (APSs) and specific surface area (SSAs) from BET

The APSs for these materials were estimated from Debye-scherrer line broadening and their SSAs (Table 2). Both methods give very similar results. The average SSAs for the samples are 52 ± 5 m^2/g, giving APS values of 15 ± 3 nm. Although the Hahn/Winterer studies [23, 24] show that particle sizes decrease with increasing alumina contents, in the zirconia-rich region, we do not observe any such changes. This may be a consequence of the differences in method of processing or precursors used. Note that LF-FSP production is at rates of 100-300 g/h vs 3 g/h for CVS (chemical vapor synthesis) by Hahn/Winterer.

Table 2. APSs and SSAs of as produced LF-FSP samples.

Sample	XRD line broadening Particle size (nm)	BET-derived Particle size (nm)	SSAs (m^2/g)
2.4ZrA	18 ± 1	14 ± 0.5	54 ± 0.5
4.1ZrA	18 ± 1	13 ± 0.5	57 ± 0.5
4.6ZrA	15 ± 1	13 ± 0.5	55 ± 0.5
5.9ZrA	15 ± 1	13 ± 0.5	57 ± 0.5
8.4ZrA	16 ± 1	14 ± 0.5	50 ± 0.5
13.6ZrA	13 ± 1	15 ± 0.5	47 ± 0.5
49.7ZrA	12 ± 1	11 ± 0.5	53 ± 0.5
79.4ZrA	12 ± 1	11 ± 0.5	51 ± 0.5

Scanning electron microscopy (SEM) studies

SEM was used to demonstrate powder uniformity. Figure 3 shows that SEM resolution is insufficient to reveal individual particles but does provide a view of the general particle population. These SEMs indicate that the particle populations produced here do not include any obvious micron size particles. Bell and Rodriguez [25] recently demonstrated that LF-FSP δ-Al_2O_3 nanopowders disperse perfectly in water without any apparent agglomeration or the presence of micron size particles [16, 25].

Transmission electron microscopy (TEM) studies of particle morphologies

TEM images were used to assess particle morphologies and sizes of as-prepared powders. Discussions of actual size/size distributions are not appropriate if based solely on TEM micrographs, unless combined with the XRD results. The Fig. 4 images are high-resolution

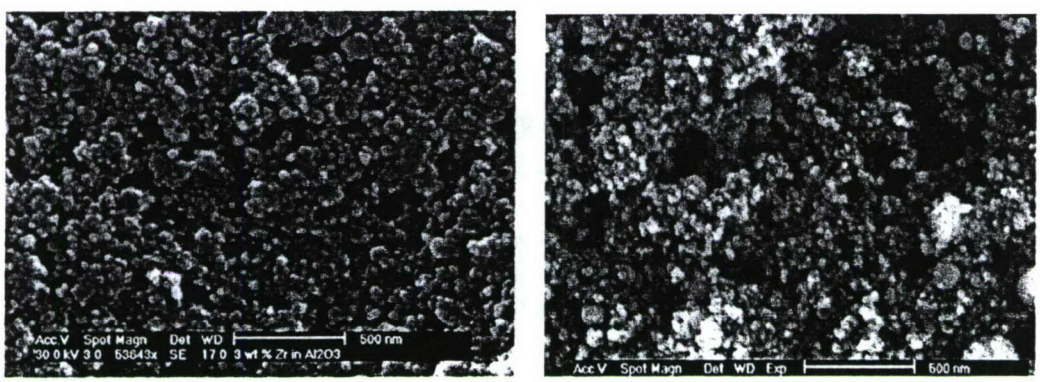

(a) (b)

Fig. 3. SEM images of (a) 2.4 mole% ZrO_2 in Al_2O_3. (b) 79.4 mole % ZrO_2 in Al_2O_3.

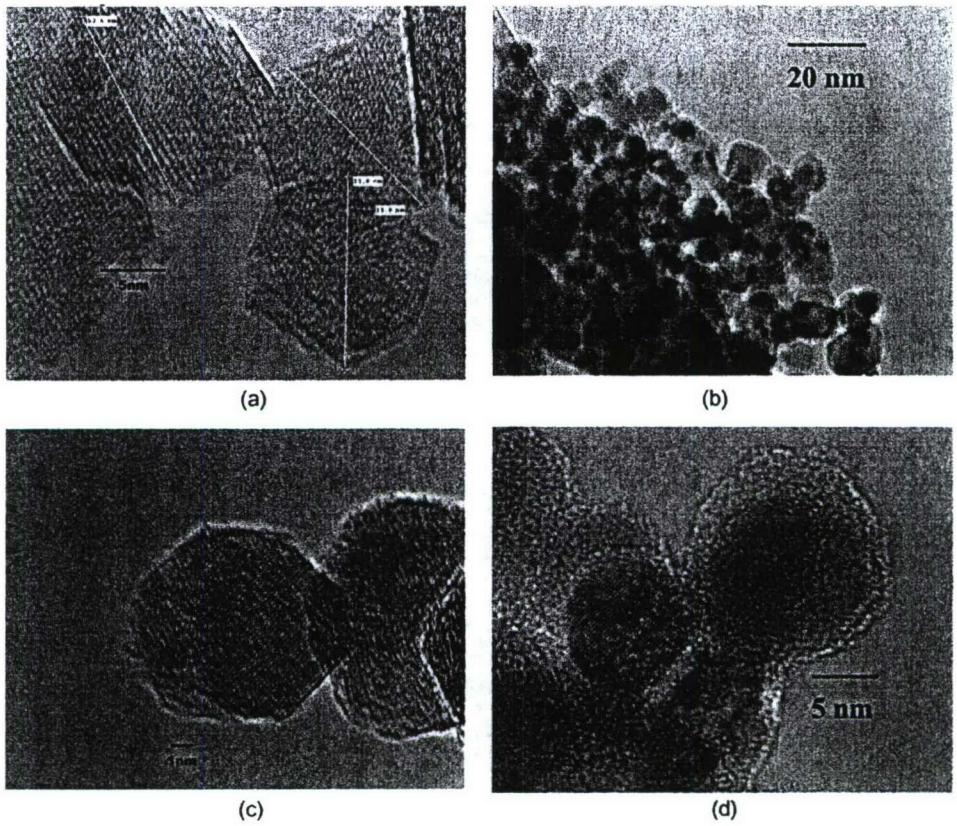

Fig. 4. TEM micrographs of (a) 4.1 mole% ZrO_2 in Al_2O_3. (b) 49.7 mole % ZrO_2 in Al_2O_3. (c), (d) 79.4 mole % ZrO_2 in Al_2O_3.

TEM micrographs of $(ZrO_2)_x(Al_2O_3)_{1-x}$ nanopowders. The particle sizes here are typically below 30 nm in diameter with the vast majority < 20 nm.

In Fig. 4, clear lattice fringes show a high degree of crystallinity and strain, especially in the high zirconia content sample (49.7 mole % ZrO_2 in Al_2O_3, 79.4 mole % ZrO_2 in Al_2O_3). The lattice fringes are multi-directional and strain directions are different and multi-faceted in single particles which is likely a consequence of particle formation during rapid quench from the gas phase.

The highest zirconia content sample (79.4 mole % ZrO_2 in Al_2O_3) images show the formation of core-shell materials. This corroborates the XRDs of Fig. 2 indicating phase segregation between t-zirconia and δ-alumina. Since Al_2O_3 has a lower vaporization temperature (3000 °C) than ZrO_2 (5155 °C) in LF-FSP, ZrO_2 should condense and nucleate first from the gas phase followed by Al_2O_3. We assume that t-zirconia nanoparticles form first during quenching, then alumina nucleates on the t-zirconia nanoparticles forming the observed core-shell nanopowders in single step.

In the low zirconia content sample (4.1 mole% ZrO_2 in Al_2O_3), the lattice fringes are uniform. Combined with XRD, the co-existence of t-zirconia and δ-alumina is easily observed in the high ZrO_2 content sample, while δ-alumina dominates the low ZrO_2 content samples.

FT-IR studies

Once particle morphologies were characterized, a detailed picture of particle surface chemistries and thermal behavior was developed. These studies began with FTIR examination of the particle surfaces per Fig. 5.

All of the materials exhibit weak OH absorptions in the 3700-3000 cm^{-1} region, attributable to surface hydroxyls arising from both physi- (3500-3000 cm^{-1}) and chemi-sorbed (3500-3700 cm^{-1}) water [26]. These bands are associated with the 1-4% mass losses seen at 400 °C in the TGA studies below.

From 1800 to 1400 cm^{-1}, peaks attributable to surface confined CO_2 and carbonates are observed as expected and in accord with those seen for pure δ-Al_2O_3 [27]. Bands in the 1000-400 cm^{-1} region correspond to tetrahedrally coordinated νAl-O at 810 cm^{-1} and octahedrally coordinated νAl-O at 610 cm^{-1} [28]. νZr-O stretching vibrations are found at 700 cm^{-1} [29].

TGA-DTA studies

Figure 6a shows mass loss events for as-processed $(ZrO_2)_x(Al_2O_3)_{1-x}$ composition nanopowders. All powders exhibit 1-4 wt% mass losses up to ≈400 °C. Much of this, up to ≈350 °C, is attributed to evolution of both

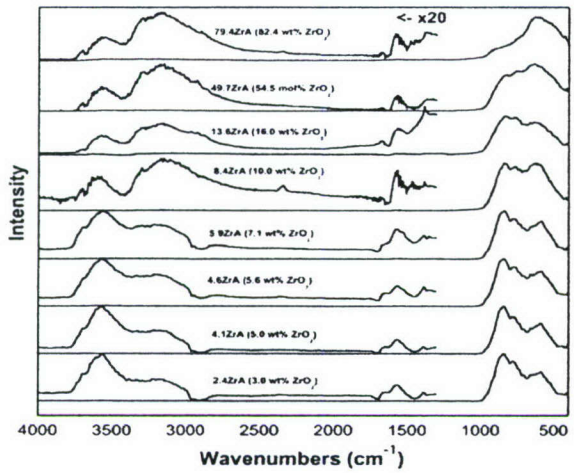

Fig. 5. FTIR spectra of $(ZrO_2)_x(Al_2O_3)_{1-x}$. 2.4ZrA denotes 2.4 mole % ZrO_2.

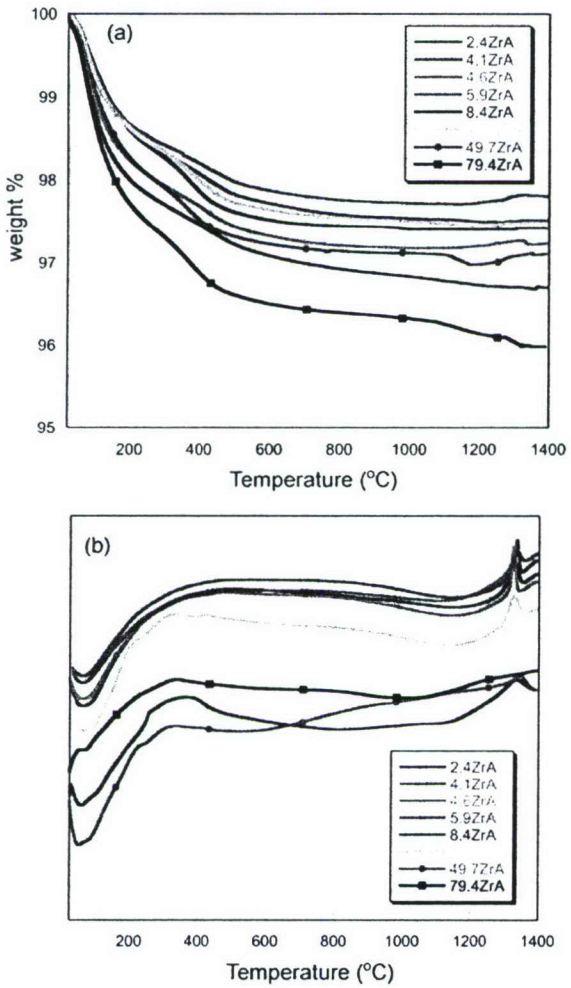

Fig. 6. (a) TGA of as-processed $(ZrO_2)_x(Al_2O_3)_{1-x}$ ramped at 10 °C/min/air. (b) DTA of as-processed $(ZrO_2)_x(Al_2O_3)_{1-x}$ ramped at 10 °C/min/air.

physi- and chemisorbed water from particle surfaces. Mass losses between 350° and 400 °C are attributed to decomposition of the carbonate species.

The δ to α alumina phase transformation is observed as exotherms above 1300 °C in the DTA (Fig. 6b). Coincidentally we also see slight mass gains in the TGA (Fig. 6a) simultaneously, except for the 79.4 mol % ZrO_2 sample. The most reasonable explanation for these mass gains is oxidation of some unknown $Zr^{2+/3+}$ species. However their appearance, especially at relatively low ZrO_2 contents, requires some discussion.

From the literature, the solubility of zirconia in δ-alumina is less than 0.03 wt% [30-34], and zirconia is essentially insoluble in α-alumina [33, 34]. We presume that some $Zr^{2+/3+}$ ions are produced during LF-FSP and form solid solutions perhaps as a spinel phase ($ZrAl_2O_4$) or some unknown form (e.g. $ZrAlO_3$). Similar observations were made for Ti aluminate in previous studies [35, 36]. We presume that these $Zr^{2+/3+}$ ions segregate out during the δ to α alumina transformation and oxidize to ZrO_2. The maximum mass gain of 0.2 wt% is assumed to be oxygen as these Zr ions oxidize to ZrO_2.

In Table 3, we estimate the possible maximum amounts of $Zr^{2+/3+}$ ions from the mass gains. Here we assume that the Zr species formed during LF-FSP are all either Zr^{2+} or Zr^{3+} ions without mixed states. We assume that the dissolved Zr^{3+} ions form coincident with oxygen vacancies. From this study, we find that the amount of dissolved zirconia (assuming ZrO/Zr_2O_3 stoichiometries) is greater than the solubility limit of zirconia in δ-alumina reported in the literature [30-34].

As with many of our previous studies, LF-FSP materials generated by rapid quenching lead to novel kinetic products not expected based on traditional processing methods that typically drive formation through thermodynamic assaults on particle mixtures. Since traditional processing methods lead to thermodynamically rather than kinetically defined phase compositions, these materials may offer unique opportunities for catalyst and fuel cell

Table 3. Possible maximum portions of dissolved $Zr^{2+/3+}$ ions in δ-alumina.

Sample	Mass gain	Possible maximum Zr^{2+} * (mol ± 0.1%)	Possible maximum Zr^{3+} † (mol ± 0.1%)
2.4 ZrA	0.07 wt %	0.4	0.6
4.1 ZrA	0.09 wt%	0.5	0.7
4.6 ZrA	0.14 wt%	0.9	1.4
5.9 ZrA	0.2 wt%	1.2	1.8
8.4 ZrA	0.2 wt%	1.2	1.8
13.6 ZrA	0.2 wt%	1.2	1.8
49.7 ZrA	0.2 wt%	1.3	2.0

*Assumes all reduced species are Zr^{2+} (ZrO). †Assumes all reduced species are Zr^{3+} (Zr_2O_3)

applications.

Zr^{3+} in Al_2O_3 may also offer utility in photonic applications. For example, Ti^{3+} in an α-alumina (Ti^{3+} doped sapphire) is widely-used as a laser material [37-39]. The amount of Ti^{3+} dissolved in sapphire (α-alumina) commercial lasers is usually 0.05~1.0 wt %. For a Ti^{3+} ion substitutionally incorporated in an Al^{3+} lattice site, the degenerate $3d^1$ electron energy level is split under the influence of the local crystal field [40]. As a result, an optical transition arises leading to strong electron-phonon coupling that broadens the optical transition vibronically. Excitation to upper levels is characterized by strong absorption in the blue-green, and a radiative relaxation to the lower level gives rise to the broad fluorescence band that extends from 600 to 1050 nm [40, 41].

Since we find similar amounts of Zr^{3+} (assumed) dissolved in δ-alumina from our TGA-DTA studies and Ti^{3+}/Zr^{3+} ions have same valence electron configuration ([Ar]$3d^1$ for Ti^{3+} and [Kr]$4d^1$ for Zr^{3+}), we may expect photonic properties for our Zr^{3+} in Al_2O_3.

Finally, the identification of a method of forming core-shell nanoparticles suggests multiple opportunities for novel processing of ZTA materials for forming duplex structures and for superplastic deformation [42, 43]. We plan to test this approach in the near future.

Conclusions

LF-FSP provides access to mixed-metal oxide nanopowders with exceptional control of stoichiometry and phase purity. Here we have succeeded in preparing nanopowders of any composition in ZrO_2-Al_2O_3 tieline with specific surface area of ≈50 m^2/g at rates of 100-300 g/h.

Furthermore we have demonstrated access to core-shell nanoparticles in the $(ZrO_2)_x(Al_2O_3)_{1-x}$ system that may offer novel potential for processing dense, defect free ZTA composite materials.

Since LF-FSP enables rapid quenching of the combustion species, it offers access to new, kinetic materials not accessible by other conventional processing method. Thus, we were able to observe what appears to be the presence of of $Zr^{2+/3+}$ ions in Zr-Al-O binary system. These nanopowders may offer utility in photonic applications anticipated based on Ti doped sapphire lasers.

Acknowledgments

This work was supported in part by the Air Force Office of Scientific Research on Contract F49620-03-1-0389.

References

1. M.W. Pitcher, S.V. Ushakov, A. Navrotsky, B.F. Woodfield, G. Li, and J. Boerio-Gooates, J. Am. Ceram. Soc. 88[1] (2005) 160-167.
2. R. Mueller, R. Jossen, S.E. Pratsinis, M. Watson, and M.K. Akhtar, J. Am. Ceram. Soc. 87[2] (2004) 197-202.
3. T. Klimova, M. L. Rojas, P. Catillo, R. Cuevas, and J. Ramirez, Microporous and Mesoporous Materials 20 (1998) 293-306.
4. H. Neumann, G. Hotzel, and G. Lindermann, SAE internatonal (1997) 970459.
5. S. Park, J.M. Vohs, and R.J. Gorte, Nature 404 (2000) 265-267.
6. Y. Kim, J. Koo, J. Han, S. Choi, H. Jeon, and C. Park, J. Appl. Phys. 92[9] (2002) 5443-5447.
7. M. Zhu, P. Chen, R. Fu, W. Liu, C. Lin, and P. Chu, Thin Solid Films 476 (2005) 312-316.
8. T. Aruna, and K.S. Rajam, MRS Bulletin 39 (2004) 157-167.
9. G. Magnani, and A. Brillante, J. Eur. Cer. Soc. 25 (2005) 3383-3392.
10. D. Casellas, M.M. Nagl, L. Llanes, and M. Anglada, J. Am. Ceram. Soc. 88[7] (2005) 1958-1963.
11. J.S. Moya, H.P. Steier, and J. Requena, Composites: Part A 30 (1999) 439-444.
12. A.C. Sutorik, S.S. Neo, T. Hinklin, R. Baranwal, D.R. Treadwell, R. Narayanan, and R.M. Laine, J. Am. Ceram. Soc. 81[6] (1998) 1477-1486.
13. R. Baranwal, M.P. Villar, R. Garcia, and R.M. Laine, J. Am. Ceram. Soc. 84[5] (2001) 951-961.
14. C.R. Bickmore, K.F. Waldner, R. Baranwal, T. Hinklin, D.R. Treadwell, and R.M. Laine, J. Eur. Ceram. Soc. 18 (1998) 287-97.
15. J. Marchal, T. Hinklin, R. Baranwal, T. Johns, and R.M. Laine, Chem. Mater. 16 (2004) 822-831.
16. T. Hinklin, B. Toury, C. Gervais, F. Babonneau, J.J. Gislason, R.W. Morton, and R.M. Laine, Chem. Mater. 16 (2004) 21-30.
17. S. Kim, J.J. Gislason, R.W. Morton, X. Pan, H. Sun, and R.M. Laine, Chem. Mater. 16 (2004) 2336-2343.
18. J.A. Azurdia, J. Marchal, P. Shea, H. Sun, X.Q. Pan, and R.M. Laine, Chem. Mater. 18 (2006) 731-739.
19. X. Zhou, D.M. Hulbert, J.D. Kuntz, R.K. Sadangi, V. Shukla, B.H. Kear, and A.K. Mukherjee, Mater. Sci. Eng. A 394 (2005) 353-359.
20. M. Kim, and R.M. Laine, Unpublished work.
21. T. Hinklin, B.L. Mueller, and R.M. Laine, U.S. Patent 5,418,298 (1995)
22. R.narayanan, and R.M. Laine, App. Org. Chem. 11 (1997) 919-927.
23. V.V. Srdic, and M. Winterer, Chem. Mater. 15 (2003) 2668-2674.
24. V.V. Srdic, M. Winterer, and H. Hahn, J. Am. Ceram. Soc. 83[8] (2000) 1853-1860.
25. N.S. Bell, and M.A. Rodriguez, J. Nanosci. Nanotech. 4[3] (2004) 283-290.
26. J.B. Peri, J. Phys. Chem. 69 (1965) 211
27. J.M. Saniger, Mater. Lett. 22 (1995) 109-113.
28. P. Tarte, Spectrochim. Acta 23A (1967) 2127-2143.
29. J. Chandradass, and M. Balasubramanian, Ceram. Int. 31[5] (2005) 743-748.
30. M.A. Stough, and J.R. Hellmann, J. Am. Ceram. Soc. 85[12] (2002) 2895-2902.
31. M.K. Loudjani, and R. Cortes, J. Eur. Ceram. Soc. 20 (2000) 1483-1491.
32. D.A. Jerebtsov, G.G. Mikhailov, and S.V. Sverdina, Ceram. Int. 26 (2000) 821-823.
33. B. Djuricic, S. Pickering, P. Glaude, D. Mcgarry, and P.

Tambuyser, J. Mater. Sci. 32 (1997) 589-601.
34. O. Fabrichnaya, and F. Aldinger, Zeitschrift Fur Metallkunde 95 (2004) 27-39.
35. M. Grinberg, A. Mandelis, and K. Fjeldsted, Phys. Rev. B 48[9] (1993) 5935-5944.
36. T. Mizoquchi, M. Sakurai, A. Nakamura. K. Matsunaga, I. Tanaka, T. Yamamoto, and Y. Ikuhara, Phys. Rev. B 70 (2004) 153101
37. T. Amthor, M. Sinther, and T. Walther, Laser Phys. Lett. 3 (2006) 75-78.
38. J. Philip, C. D'Amico, G. Chériaux, A. Couairon, B. Prade, and A. Mysyrowicz, Phys. Rev. Lett. 95 (2005) 163901.
39. A. Mandelis, J. Vanniasinkim, S. Budhudu, A. Othonos, and M. Kokta, Phys. Rev. B 48[10] (1993) 6808-6821.
40. L.M.B. Hickey, E. Martins, J.E. Román, W.S. Brocklesby, and J. S. Wilkinson, Opt. Lett. 21[8] (1996) 597-599.
41. K. Morinaga, H. Yoshida, and H. Takebe, J. Am. Ceram. Soc. 77[12] (1994) 3113-3118.
42. A.J.A. Winnubst, M.M.R. Boutz, Y.J. He, A.J. Burggraaf, and H. Verweij, Ceram. Int. 23 (1997) 215-221.
43. S. Ishihara, T. Tanizawa, K. Akashiro, N. Furushiro, and S. Hori, Mater. Trans. JIM 40[10] (1999) 1158-1165.

Transparent, polycrystalline upconverting nanoceramics. Towards 3-D displays**

*Thomas R. Hinklin, Stephen C. Rand and Richard M. Laine**

ABSTRACT

We describe here the concept of a 3-D display wherein arrays of transparent upconverting phosphor pixels are formed in a 3-D hollow shape are illuminated from within with a rastered IR source and upconvert IR to red, green and blue light in an "inverse planetarium" format to provide 3-D images. To realize such a display, one of the key steps must be the ability to produce transparent polycrystalline pixels. We report here the production of $(Y_{0.86}Yb_{0.11}Er_{0.03})_2O_3$ and $(Y_{0.929}Yb_{0.070}Tm_{0.001})_2O_3$ composition nanopowders, their characterization and processing to transparent, polycrystalline red and blue upconverting phosphors. The initial powders exhibit the cubic phase of yttria, and consist of unaggregated, single crystals with average particle sizes <50 nm that are readily compacted to green densities of 60-63 % of theory. Binder burnout on heating to 800°C in air, vacuum sintering to 1350°-1450°C and HIPping at similar temperatures at 140 MPa provides dense pellets with average grain sizes of ≈ 400 nm and up to 70 % transparency. These materials effectively unconvert 980 nm IR light to visible light (e.g. 662 nm for Er doped material) and offer the potential to serve as pixel materials for the proposed "inverted planetarium" 3-D display.

[*]Dr. Thomas R. Hinklin, Prof Richard M. Laine; Depts. of Materials Science and Engineering, and Professor Stephen C. Rand, Dept. of Electrical Engineering and Computer Science, University of Michigan, 2300 Hayward St. Ann Arbor, MI 48109-2136

[**] The authors thank AFOSR (F49620-99-1-0158) as well as NSF DMR-0502715 and CISE-0531086 for support of this work. We also thank one reviewer for important contributions.

Although the concept of transparent, polycrystalline ceramics is now 40 years old, only recently has control of processing parameters been sufficient to produce photonic quality materials, Nd:YAG and Yb:Yttria lasers in particular.[1-7] In all instances, average grain sizes (AGSs) in these fully dense materials are in the range 10-50 μm. Furthermore, photonic quality transparency has only been achieved for materials with cubic crystal structures thereby avoiding scattering due to birefringence.

Recent work by Krell et al points to the possibility of also obtaining photonic transparency in materials with submicron AGSs, in α-Al_2O_3 in particular.[8-10] In principle, the smaller the final AGS and average defect size, the higher the expected transparency even for non-cubic crystal systems such as titanium doped sapphire (0.5 at % Ti^{3+} in α-Al_2O_3) or ruby (0.5-3.0 at % Cr^{3+} in α-Al_2O_3). Access to such materials is best served by sources of high quality nano-oxides that permit low-temperature densification without coincident grain growth.

If transparency can indeed be achieved with very fine-grained ceramics, the potential exists to create three-dimensional emissive displays[11] using the "inverted planetarium" concept described below. Transparent, upconverting phosphor pixels uniformly arrayed in thin walled spherical, cylindrical or even box shapes could provide 3-D displays in which color would be achieved by computer controlled rastoring of an IR laser (or lasers) in the interior of the display across the pixels at rates fast enough to generate 3-D images. Upconverting phosphors typically capture two IR photons (e.g. 960 nm) and subsequently emit visible red, green and blue light depending on the phosphor, thus no visible beam is observed from a rastored IR source. [12-14] Quantum efficiencies can be upwards of 5%.[14-16]

There is a significant body of work associated with upconversion in glass-ceramics and powders especially those made by sol-gel methods;[17-19] however, there are no examples of upconversion from transparent polycrystalline ceramics in the literature. The approach described here complements recent work, in particular by the Downing group,[20] to produce 3-D upconversion displays in solid transparent non-oxide glasses by direct impingement of two lasers of different wavelengths at a "voxel" to produce a specific color (RGB) dependent on the wavelengths of the lasers used and the rare-earth dopants using for upconversion. This technique was recently demonstrated for laminates of glasses each with a different phosphor (RGB).[20]

To realize inverted planetarium 3-D displays, several key processing methods must be brought to bear simultaneously. First, methods are needed to process uniformly arrayed pixels in thin green bodies. Each pixel should offer resolution of at least 50 μm but preferably < 20 μm. Pixels must be separated from each other by 1-10 μm by a non-emitting phase.[20] Second, the pixels must be made transparent so they can be irradiated from the interior of the display with an IR laser. Third, a sufficiently powerful IR laser (or lasers) is (are) required whose light can be rastored at rates sufficient to illuminate the pixels for saturated output at the required refresh rate. We believe these processing and excitation issues are readily resolvable with current technology.

For example, uniformly arrayed matrices with sub 10 μm resolution are now accessible through extrusion methods developed by Halloran et al.[21-24] Furthermore, current back lit, large screen displays use micro-mirrors to raster light sources across pixels on display surfaces.[11,22,26-27] It appears that the greatest barrier to realizing such 3-D displays may be in creating small, transparent pixels of upconverting phosphors. Because pixel sizes should be as small as possible for optimal resolution, it seems that only transparent nanostructured pixels and matrices would provide the appropriate sizes, the required separation between pixels and sufficient mechanical strength to provide robust 3-D thin, hollow structures. The intent of this paper is to demonstrate process-

ing of transparent polycrystalline upconverting phosphors that can serve as pixel materials for the proposed displays.

We have previously demonstrated that liquid-feed flame spray pyrolysis (LF-FSP) provides combinatorial access to a wide variety of single and mixed-metal oxide nanopowders[28,29] including a novel hexagonal $Y_3Al_5O_{12}$,[31] nano-α-Al_2O_3,[32] abnormal spinel phases,[33] and sets of upconverting phosphors.[34] We have further reported novel laser action in doped versions of these nanopowders.[35] We report here a method of processing selected RE:Yb^{3+}:Y_2O_3 upconverting phosphors to produce dense nanostructured materials that emit red and blue light, and are transparent suggesting that it may indeed be possible to develop a new form of 3-D display.

Figure **1** shows typical as-produced Er^{3+} doped nanopowders with average particle sizes of < 50 nm. As with the majority of the powders produced by LF-FSP, these materials are single crystals that are primarily (>90%) the cubic phase. These powders are readily processed (see below) using traditional dispersion techniques and consolidated using cold isostatic pressing to form green bodies with average densities of 60-63 % of theoretical. Thereafter the powders are debindered by heating to 800°C, vacuum sintered at 1350° or 1400°C for 5 h to densities > 95% and then HIPped at 1350° or 1400°C at 140 MPa for 3 h. Subsequently, the pellets were air annealed for 3 h at 1250°C producing the pellets shown in Figure **2** with typical microstructures as exemplified

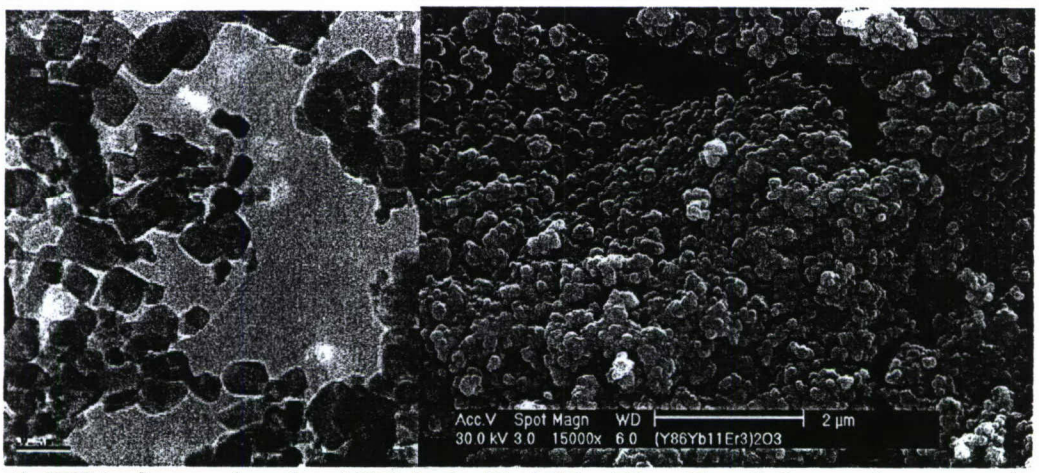

Figure 1. TEM of as produced and SEM of milled $(Y_{0.86}Yb_{0.11}Er_{0.03})_2O_3$ powder suspension.

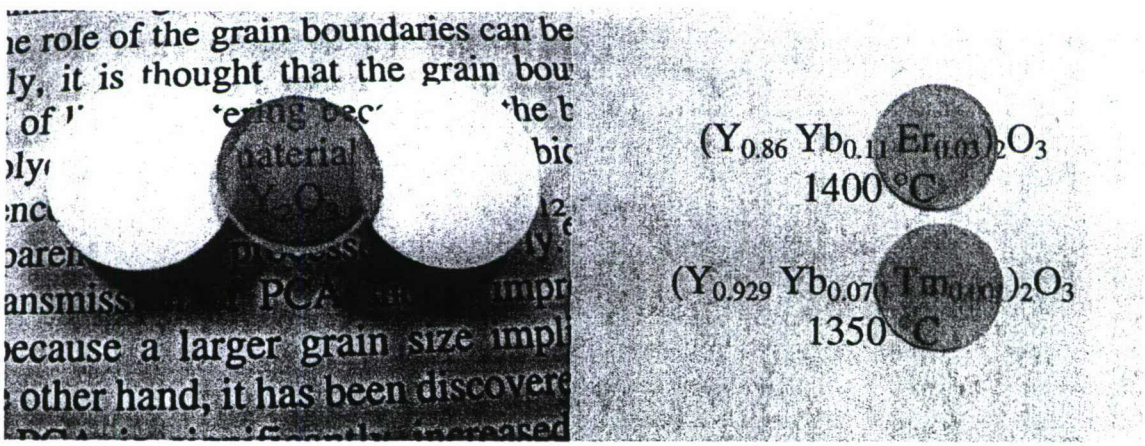

Figure 2. OM of 12.7x1 mm red and blue upconverting transparent polycrystalline phosphors.

for the Er doped pellet in Figure **3a**. The resulting pellets offer transparencies of up to 70% depending on the wavelength, Figure **4**. Furthermore, as seen in Figure **3b**, on illumination with 980 nm light, through a mask, they upconvert this light to 662 nm emission in the form of an M. Full emission spectra are presented in Figure **5**.

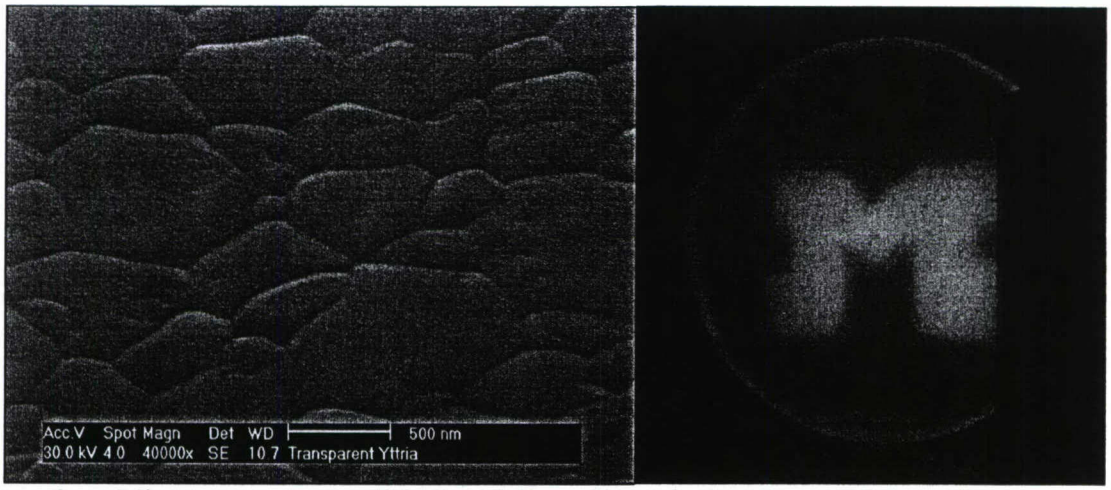

Figure 3. a. Microstructure of polished and thermally etched surface of HIPped Er doped material, > 98% dense showing average grain sizes of 400 nm. **b**. Red emission (662 nm) on exposure to 980 nm light (ϕ = 1 cm, thickness = 1 mm).

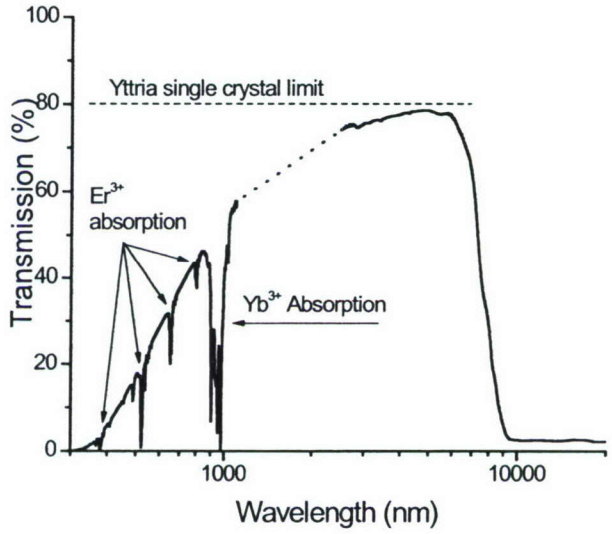

Figure 4. Transmission of polished, HIPped Er doped material, 1 mm thick.[36]

The transmission behavior, although not perfect in the visible, is more than sufficient for our purposes given that we desired high absorption in the IR at ≈ 980 nm on the $^4F_{7/2}$ - $^4F_{5/2}$ transitions of Yb^{3+} to optimize emission efficiencies. It is important to note that the IR transmission rivals that reported for large grained and single crystal materials such as yttria, sapphire, etc as

shown in Figure **4**.[36] In Figure **4** additional (unused) absorption features are seen near 810, 660 and 540 nm resulting from transitions of Er^{3+} ions.[37,38]

The corresponding emission lines in Figure 5 resemble the narrow, Stark-split transitions of traditionally Er^{3+} and Yb^{3+} doped crystalline yttria.[34,37-40]

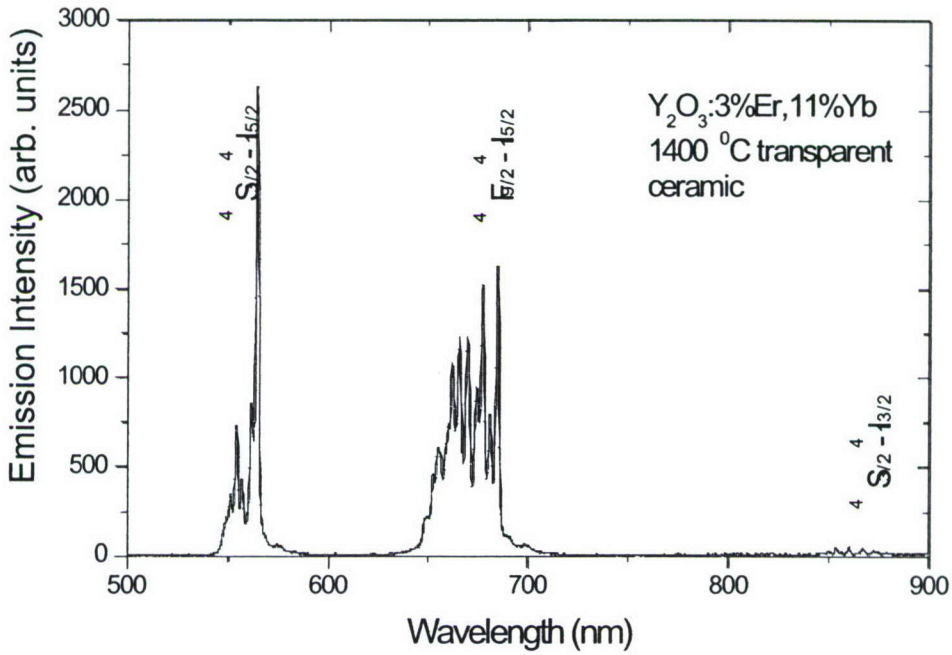

Figure 5. Emission behavior of polished, HIPped Er doped material, 1 mm thick.[38]

The use of crystalline rare earth oxides in display materials has been studied extensively over the past 20 years.[37-45] Efficiencies are a key concern in emissive displays in rare earth materials, where multiple relaxation channels often exist. Not all channels result in light emission. Moreover there is abundant evidence in the literature that upconversion efficiency drops dramatically in rare earth nanophosphors compared to bulk solids. However recently[44] it was convincingly demonstrated that loss of efficiency in nanoparticles should be attributed predominantly to the incorporation of impurities such as OH during particle synthesis and to the use of hosts with high phonon frequencies. If present, impurities at the surfaces of particles are particularly effective at providing non-radiative relaxation channels for the emissive species. Fortunately, using LF-FSP powder synthesis and the processing approaches adopted here, it is feasible to prepare transparent ceramics where the transgrannular interfaces contain minimal amounts of -OH, eliminating this loss channel. Additionally, if grain sizes can be maintained below 30 nm, the increased density of low frequency phonon states known to arise purely from small particle sizes can be expected to reduce non-radiative losses further, obviating the need to select special hosts specifically for their low bulk phonon frequencies.[45] In contrast, sol-gel derived materials will retain significant concentrations of –OH and any efforts to reduce their content by heating will likely lead to crystallization and loss of transparency.

This first step in realizing an appropriate pixel material; while successful, requires multiple additional steps before a true 3-D display system could be realized. First, the quality of the materials must be improved both in terms of transparency, grain sizes and emission wavelengths. Second, the extrusion process to generate pixilated structures must be explored and refined. Third, quantum efficiencies of these two photon processes must be optimized for both materials and a green upconverting phosphor, most likely one replacing Er^{3+} with Tb^{3+} must be developed.[39,40] Fourth, although it is possible to produce RGB upconverting phosphors, as yet there are no indications that it is possible to access chromaticities that would have CIE coordinates that allow the production of true full color displays. Rather it may only be possible to create one or two color 3-D displays. Lastly, optimal performance can only be expected if it is possible to match the emission efficiencies for each phosphor component.

Finally, in the inverted planetarium approach, which will use thin pixels, transmission efficiencies are likely to be much less of a problem than in a system, as discussed above, that requires two lasers of complementary wavelengths to focus on a voxel. In the latter case, very high quality transparency is needed for laser light to traverse some significant fraction of a bulk solid to illuminate a particular voxel, without experiencing significant scattering. In addition, the resolution for this type of system may be limited by the ability to focus the laser beam. In contrast, in the inverted planetarium approach, each pixel is defined by its diameter if it is assembled within an undoped surrounding matrix unresponsive to laser light. The ultimate thickness of the pixel will be defined by the efficiency with which the laser light is absorbed.

Experimental Section

Materials. Samples of upconverting phosphors were produced as described earlier.[30,34]

Liquid-feed FSP.

The apparatus used for LF-FSP consists of an aerosol generator, a combustion chamber and an electrostatic powder collection system described elsewhere in greater detail.[24-29] The precursor solution is pumped through the aerosol generator at a rate adjusted to the ceramic yield of the solution: more concentrated (5 wt% ceramic yield) solutions were pumped at 100 mL/min to avoid obtaining large particles (200-1000 nm).[24,25] Solutions with lower ceramic yields were pumped at 400 mL/min. The precursor solution was atomized with oxygen to form an aerosol and ignited by two methane/oxygen pilot torches, while the pressure in the system was kept at 20 psi. Combustion produces temperatures >1500°C[24] and nanosized oxide powders are collected in electrostatic precipitators (ESP). The production rate was typically ~50 g/h.

Annealing studies.

Heat treatments were conducted in a Lindberg/Blue box furnace (Model No. 58114, Watertown WI, controlled by a Eurotherm microprocessor, model No. 818P, Northing, England). Samples (500 mg) of nanopowders were placed in alumina boats and heated to various temperatures from 850° to 1650 °C at 20°C/min in air and maintained at temperature up to 12 d. The resulting powders were cooled and analyzed as described below.

Powder treatment and compact formation. The as produced LF-FSP powders (10 g) were dispersed in EtOH (100 mL) using a 1/2" ultrasonic horn (Sonics and Materials 600 VCX, Newtown, CT) at 40% power for 10 min in a Teflon beaker. The dispersion was allowed to settle for 48 h and the supernatant was extracted using a syringe without disturbing the sediment (≈ 200 mg). The suspended powder in the syringe was further processed by adding bicene (50 mg) and roll milled (24 h) using 3mm zirconia media (Union Process, Akron, OH) followed by the addi-

tion of 1000 D (75 mg) and 8000 D (75 mg) polyethylene glycol (Aldrich) and milled for an additional 24 h.

After removal of the media, the dispersion was dried in a rotary evaporator at 150°C. The dried powders were lightly ground in an alumina mortar and pestle and sieved to –325 mesh using nylon mesh in an acrylic holder. The granulated powder (500 mg) was pressed (20 MPa) in a dual action 12 mm WC die followed by cold isostatic pressing (CIP) (200 MPa) (Autoclave Engineers, Erie, PA). The pressed pellets were subjected to a stepped binder burn out (2°C/min to 800°C in air with 30 min holds every 100°C).

Hot Isostatic Pressing. The binderless pellets were sintered in a $MoSi_2$ tube furnace (Thermolyne 54500) in an alumina process tube (99.9% Vesuvius McDanel, Beaver Falls, PA) under a mild vacuum (-25" H_2O) to 1350° or 1400°C for 5 h to achieve pore closure. The closed porosity pellets were then hot isostaticaly pressed (HIP) at 1350° or 1400°C with 20 ksi Ar for 3 h. The HIPped pellets were then returned to stoichiometry by annealing in air (1250°C, 3h).

UV-VIS transmission spectra were acquired using a Varian Cary 50 Bio UV-VIS spectrometer (Australia) from 1100 to 200 nm. Background calibrations were performed by collecting the raw and blocked beam spectrum continuously in the range of 1100-200 nm with a scan resolution of 0.2 nm and rate of 1 nm/s. Sample spectra were collected placing polished samples in the beam, held at the top and bottom edge with scotch tape.

Scanning electron microscopy (SEM). Micrographs were taken using a Phillips XL30 SEM. The powders were dispersed in distilled water using an ultrasonic horn (Vibra-cell, Sonics and Materials Inc.). Drops of the dispersed materials were deposited on an aluminum SEM stub and dried for 3 h on a hot plate. Samples were coated with a gold/palladium coating by sputtering for 2 min, using a Technics Hummer VI sputtering system (Anatech Ltd.).

Transmission electron microscopy. Micrographs were taken on a JEOL 2100 XL. Samples were prepared using a carbon coated copper TEM grid (300 mesh). The powder was dispersed in distilled water using an ultrasonic horn, as above, and then a drop of the dispersed powder/water mixture was deposited on the grid. The grid was then dried for 4 h at 80°C. The JEOL 2100 XL was used with an accelerating voltage of 200 kV.

References

1. C. Greskovich, J.P. Cernoch, J. Appl. Phys., **44**, 4599-4606 (1973).
2. A. Ikesue, T. Kinoshita, J. Am Ceram. Soc. **78**, 1033-40 (1995).
3. I. Shoji, S. Kurimura, Y. Sato, T. Taira, A. Ikesue, K. Yoshida, Appl. Phys. Lett. **77**, 939-41 (2000).
4. A. Ikesue, Y.L. Aung, T. Taira, G. L. Messing, Annu. Rev. Mater. Res. **36**, 397-429 (2006).
5. A. Ikesue, Y.L. Aung, J. Am. Ceram. Soc. **89**, 1936-44 (2006).
6. J-G. Li, T. Ikegami, J-H. Lee, T. Mori, J. Am. Ceram. Soc. **83**, 961-63 (2000).
7. J. Lu, M. Prabhu, J. Song, C. Li, J. Xu, K. Ueda, A.A. Kaminskii, H. Yagi, T. Yanagitani, Appl. Phys. B 71, 469-73 (2000).
8. A. Krell, P. Blank, H. Ma, T. Hutzler, R. Apetz, M.P.B. van Bruggen, J. Am. Ceram. Soc. **86**, 12-8 (2003).
9. R. Apetz, M.P.B. van Bruggen, J. Am. Ceram. Soc. **86**, 480-6 (2003).
10. A. Krell, J. Klimke, J. Am. Ceram. Soc., **89**, 1985-92 (2006).
11. A. Sullivan, IEEE Spectrum, **42**, 4, 30-5 (2005).
12. F. Auzel, Chem. Rev. **104** 139-174 (2004).
13. A.M. Pires, S. Heer, H.U. Güdel, O. A. Serra, J. Fluorescence, **16** 461-8 (2006).

14. K. Kuningas, T. Rantanen, T. Ukonaho, T. Lövgren, T. Soukka, Anal. Chem. 77, 7348-55 (2005).
15. R.H. Page, K.I. Schaffers, P.A. Waide, J.B. Tassano, S.A. Payne, W.F. Krupke, J. Opt. Soc. Am. B, **15** 996-70 (1998).
16. S. Redmond and S.C. Rand, Opt. Lett. 28, 173 (2003).
17. A. Biswas, G. S. Maciel, C. S. Friend, P. N. Prasad, J. Noncryst. Solids, **316**, 393-397 (2003).
18. F. Vetrone, J. C. Boyer, J.A. Capobianco, A. Speghini, M. Bettinelli, J. Phys. Chem. B, **107**, 1107 (2003).
19. P. Y. Jia, J. Lin, M. Yu, Mater. Res. Bull., 42, 1556-64 (2007).
20. a. E.A. Downing, "Method and system for three-dimensional display of information based on two-photon upconversion," U.S. Patent 5684621 Nov 4, 1997. b. E.A. Downing, L. Hesselink, J. Ralston, R.A. Macfarlane, Science, **273**, 1185-1189 (1996).
21. L. Arbuthnot, J. Mendes, W. Sproull, M. Aguilera, B. Aitchison, C. King, G.Dolny, A. Ipri, F-L Hsueh, R. Steward, A. Ahmed, R. Solanki, T. Keyser, S. Schlesinger, G. Becker, D. Kagey, M. Spitzer, SID '96 Digest, 374 (1996).
22. S. Baskaran, J.W. Halloran, J. Am. Ceram. Soc., **76**, 2217-4 (1993).
23. D. Kovar , B.H. King , R.W. Trice , J.W. Halloran, J. Am. Ceram. Soc., **80**, 2471-7 (1997).
24. C.V. Hoy, A. Barda, M. Griffith, J.W. Halloran, J. Am. Ceram. Soc., **81**, 152-8 (1998).
25. A.T. Crumm, J.W. Halloran, J. Am. Ceram. Soc., **81**, 1053-7 (1998).
26. L.J. Hornbeck, "Spatial light modulator and method," U.S. Patent 4,596,992 Jun 24, 1986.
27. L.J. Hornbeck, "Linear spatial light modulator and printer," U.S. Patent 4,662,746 May, 1987.
28. T. Hinklin, B. Toury, C. Gervais, F. Babonneau, J.J. Gislason, R.W. Morton, R.M. Laine Chem. Mater. **16**, 21-30 (2004).
29. J. Marchal, T. Hinklin, R. Baranwal, T. Johns, R. M. Laine, Chem. Mater. **16**, 822-831 (2004).
30. R.M. Laine, J. Marchal, S. Kim, J. Azurdia, M. Kim, in Ceramic Nanomaterials and Nanotechnology III, S. Lu, M.Z. Hu, Y. Gogotsi eds, Ceramic Transactions Vol. **159**, 2004, pp 18-24.
31. R.M. Laine, J. Marchal, H.J. Sun, X.Q. Pan, Adv. Mater. **17**, 830-33 (2005).
32. R.M. Laine, J.C. Marchal, H.P. Sun, X.Q. Pan, Nature Materials **5**, 710-2 (2006).
33. J.A. Azurdia, J.C. Marchal, P. Shea, H. Sun, X. Q. Pan, R.M. Laine, Chem. Mater. **18**, 731-9 (2006).
34. S. Li, H. Feindt, A.C. Sutorik, M.S. Baliat, R.M. Laine, R.S. Niedbala, in Nanoscience and Nanotechnology in Perspective, Tsinghua Press, June, **2002**, pp 221-33.
35. G. Williams, S.C. Rand, T. Hinklin, R.M. Laine, Phys. Rev. A. **65**, 013807 (2002).
36. R.L. Gentilman, "Current and Emerging Materials for 3-5 Micron IR Transmission," Proc. SPIE **683**, 2-11 (1986).
37. G. H. Dieke and H.M. Crosswhite, Appl. Opt. **2**, 675 (1963).
38. P.A. Tanner, X. Zhou, and F. Liu, J. Phys. Chem. **108**, 11521 (2004).
39. B. Li, G. Williams, S.C. Rand, T. Hinklin and R.M. Laine, Optics Lett. **27**, 394-6 (2002).
40. J. McKittrick, L.E. Shea, C.F. Bacalski, E.J. Bosze, Displays **19**, 169-72 (1999).
41. a. M.V.D. Vermelho, P.V. dos Santos, M.T. de Araújo, A.S. Gouveia-Neto, F.C. Cassanjes, S.J.L. Ribeiro, Y. Messaddeq, J. Luminscence **102-3** 762-7 (2003). b. L.D. Livanova, I.G. Saitkulov, and A.L. Stolov, Sov. Phys. Solid State **11**, 750 (1969).
42. R. P. Rao, J. Electrochem. Soc. **143**, 189-197 (1996).

43. JH, Zeng, J. Su, Z. H. Li, R. X. Yan, Y. D. Li, Adv. Mater. **17** 2119-23 (2005).
44. S. Heer, K. Kompe, H. U. Gudel, M. Haase, Adv. Mater. 16 2102-05 (2004).
45. X.L. Ruan and M. Kaviany, Phys. Rev. B73, 155422 (2006).

Table of contents graphical

Text: Transparent, polycrystalline $(Y_{0.86}Yb_{0.11}Er_{0.03})_2O_3$ with an average grain size of 400 nm on irradiation with 980 nm laser light through a mask upconverts the IR photons emitting red light at 662 nm. Model for a red pixel in a 3-D inverted planetarium display.

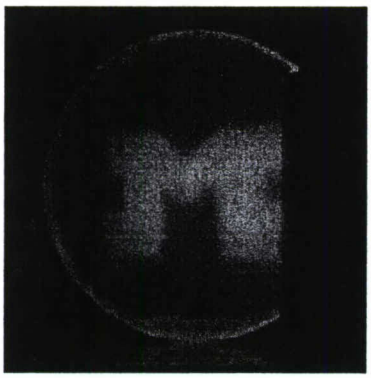

Available online at www.sciencedirect.com
ScienceDirect
Journal of Luminescence 122–123 (2007) 345–347
JOURNAL OF LUMINESCENCE
www.elsevier.com/locate/jlumin

Ultraviolet nanophosphors

Bin Li[a], Tom Hinklin[b], Richard Laine[b], Stephen Rand[a,*]

[a]*Department of Electrical Engineering & Computer Science, USA*
[b]*Department of Materials Science, University of Michigan, Ann Arbor, MI, USA*

Available online 15 March 2006

Abstract

Dopant-stabilized defect centers in alumina nanopowders are shown to be well-suited to efficient generation of ultraviolet cathodoluminescence.

Keywords: Rare earth oxides; Alumina; UV luminescence; Point defects

1. Introduction

Phosphors are widely available for display applications in the visible spectral region. This is the result of a century of active research on optical properties of semi conductors and dielectrics containing rare-earth impurities, transition metals, alkalis, and other dopants. Research on light emission in the range 250–290 nm on the other hand has been far more limited, because the radiation is invisible and very few solids either generate or transmit light efficiently at such short wavelengths, including scintillators.

The spectral range from 250–290 nm overlaps key protein absorption bands. So efficient UV phosphors in this range can be useful for decontamination and medical applications. Protein and DNA absorption bands in the ultraviolet extend from 250 to 290 nm. Radiation in this range causes damage to amino acid linkages and when combined with X-ray radiation can effectively decontaminate/sterilize contaminated surfaces. Sources in this range are also potentially important for replacing Hg discharge sources in water purification systems.

There are only a few reasonable candidates for ultraviolet-emitting solids that could replace Hg sources for applications requiring high flux. Here we consider rare-earth-doped solids, wide band gap semiconductors, and point defects.

2. Experimental methods

Flame spray pyrolysis (FSP) was used to prepare two kinds of sample for this study [1]. The first was δ-Al_2O_3 doped with 1000 ppm Ce^{3+}. The second was δ-Al_2O_3 doped with MgO to provide twenty concentrations between 0.2 and 50 mol%.

The composition and phase of these samples were determined using X-ray diffraction (XRD) and as-grown powders mounted in ultrahigh vacuum for electron beam irradiation and cathodoluminescence studies. Representative XRD traces are given in Fig. 1, to illustrate the production of different phases by FSP through variation of the Mg concentration in the Mg-doped series. The X-ray curves illustrate the significant degree of phase control that is possible through synthesis of oxide nanopowders by flame spray pyrolysis. At low Mg concentration the indexed patterns revealed a mixture of orthorhombic, tetragonal and monoclinic phases. At intermediate Mg concentration, the nanopowders were predominantly of the tetragonal phase. At high concentration only $MgAl_2O_4$ (spinel) was found.

As-grown samples were loaded into an ultrahigh vacuum chamber and subjected to a 6 keV electron beam at currents ranging from 5 to 50 μA in a 1 mm spot.

*Corresponding author. Tel.: +1 734 763 6810; fax: +1 734 647 2718.
E-mail address: scr@umich.edu (S. Rand).

0022-2313/$ - see front matter © 2006 Elsevier B.V. All rights reserved.
doi:10.1016/j.jlumin.2006.01.174

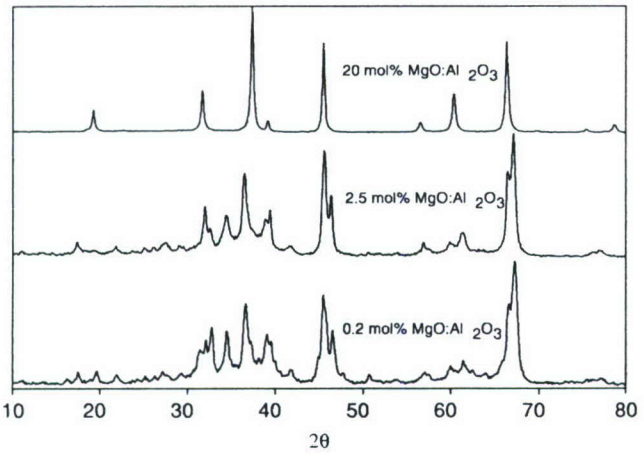

Fig. 1. X-ray diffraction patterns of selected LF-FSP $MgO:Al_2O_3$ powders. The 0.2 mol% MgO sample is a mixture of orthorhombic, tetragonal and monoclinic phases. The 2.5 mol% MgO sample is nearly pure tetragonal. The 20 mol% MgO sample is purely cubic spinel.

Cathodoluminescence was collected and analyzed with 0.25 and 1.0 m grating spectrometers using a photomultiplier and photon counting electronics.

3. Results

3.1. Rare-earth-doped phosphors

Trivalent rare-earth ions have relatively low oscillator strengths on 4f–4f transitions because these transitions are forbidden by Laporte's rule. Consequently, unless stimulated emission can be achieved in the phosphor material, ions like Nd^{3+} whose high-lying ^2F levels have a ground state transition near 260 nm are not useful for decontamination applications. Inter-configurational transitions on the other hand (for example 5d–4f transitions) are fully allowed. Emission from Ce^{3+}-doped solids on the allowed 5d–4f transition is potentially useful for this reason.

Stimulated emission can be obtained from inverted Ce ions on the ultraviolet 5d–4f transition in very fine powders pumped by an electron beam. The way in which multiple scattering mediates this process has been discussed previously [2]. In this work the potential importance of Cerium for solid state ultraviolet emission sources was confirmed by new experiments and reconsidered for this high flux application. Unfortunately, the Cerium emission spectrum does not extend below 310 nm in alumina, and not below 280 nm in fluoride hosts [3]. So while it was confirmed to provide efficient ultraviolet "laser phosphor" operation close to the protein absorption band, it must be concluded that Ce^{3+}-doped oxide phosphors per se are unsuitable for operation at 265 nm.

3.2. Wide band gap semiconductors

Wide band gap ternary alloys like $Al_xGa_{1-x}N$ offer additional possibilities for UV source technology in the range 240–280 nm. While emission properties of $Al_xGa_{1-x}N$ are not reported here, the band gap of this material can clearly be adjusted with appropriate compositions to yield band-to-band emission at 265 nm. Unfortunately surface states often lead to undesired absorption in powdered semiconductors, and this generally necessitates the use of high-quality growth techniques and passivation of particle surfaces. While $Al_xGa_{1-x}N$ thin films prepared by molecular beam epitaxy (MBE) or chemical vapor deposition (CVD) have high quantum efficiency, these approaches are relatively expensive. There are currently no high yield methods available for the production of $Al_xGa_{1-x}N$ phosphors with high radiant efficiency. Direct deposition of thin $Al_xGa_{1-x}N$ films on suitable electrode structures may nevertheless furnish high brightness and efficient emission at 265 nm. Even polycrystalline films might support random laser action similar to previous results in ZnO films [4].

3.3. Point defect centers

Of main interest in this paper for short wavelength generation are point defects created in FSP powders during the rapid thermal quench step following combustive synthesis (Figs. 2 and 3). In the spectra to follow, these consist of single oxygen vacancies and their aggregates, in various states of ionization and association with divalent Mg impurities. Single electrons occupying anion vacancies in crystalline solids have intrinsically high quantum efficiencies [5]. Even two-electron centers have quantum efficiencies approaching unity when inter-system crossing is avoided. For example the F^+ center in MgO has an oscillator strength of 0.8 [6] and the F^+ center in Al_2O_3 has a decay time of 50 ns at a wavelength of 325 nm [7], indicating a similar high radiative efficiency.

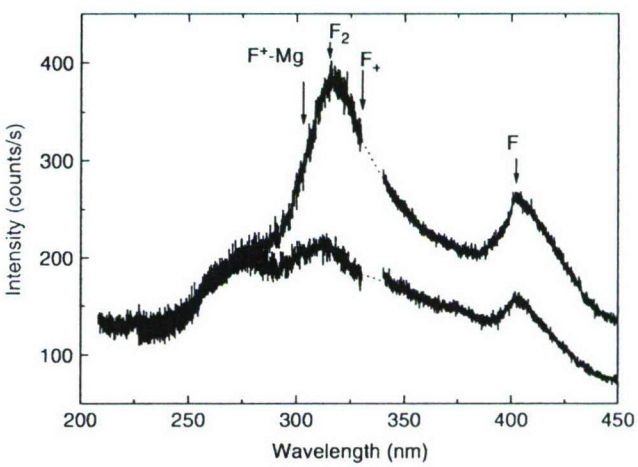

Fig. 2. Ultraviolet cathodoluminescence from 2.5%Mg-doped Al_2O_3 nanopowder. Acceleration voltage was 6 kV. The two traces correspond to beam currents of 10 (upper) and 30 (lower) microamps and reveal dramatic changes in the relative concentration of F-centers at room temperature. The spectral gap near 330 nm resulted from changing spectral orders to cover the range 200–450 with the 1 m grating spectrometer.

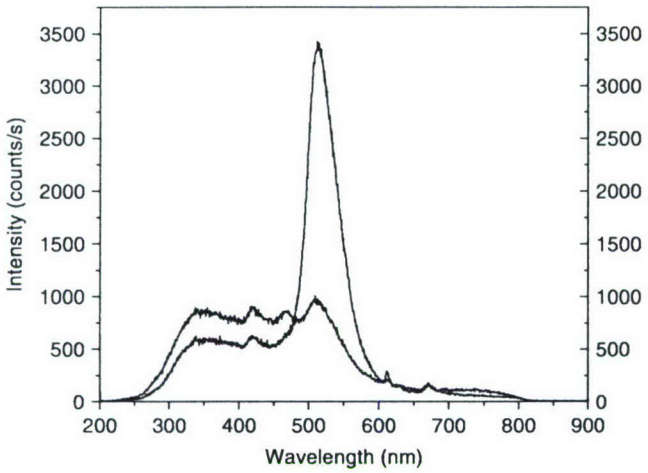

Fig. 3. Cathodoluminescence of 20%Mg:Al_2O_3 nanopowders at 6 kV. Two curves are shown, one at 10 (upper trace at 520 nm) and one at 30 (lower trace at 520 nm) microamps. Data was acquired with a 0.25 m grating spectrometer. Resolution was 1 nm.

Table 1
Absorption and emission of point defects in sapphire (references are given in parentheses)

Material	Defect	Abs. peak (nm)	Em. peak (nm)
Al_2O_3	F	205	420 [7]
Mg:Al_2O_3	F^+–Mg	255	310 [8]
Al_2O_3	F^+	258	325 [7]
Al_2O_3	F_2	300	322 [7]
Al_2O_3	F_2^+	355	379 [7]
Al_2O_3	F_2^{2+}	455	550 [7]

In Mg-doped sapphire, the presence of Mg on a site neighboring an F^+ center shifts the emission wavelength to a shorter value [8]. Since divalent cations can stabilize and shorten the emission wavelength of ionized F-centers, mixed oxides of MgO and Al_2O_3 are intriguing candidates for UV generation. Some of the basic characteristics of the primary F-centers in alumina are listed in Table 1. F^+-centers with Mg^{2+} substituting for Al^{3+} on neighboring sites (designated as F^+–Mg centers in this paper) also give rise to even shorter wavelength emission that arises from recombination of holes with F^+–Mg centers. F^+–Mg centers have a high cross section for hole recombination, higher in fact than that of isolated F^+-centers [8]. Recombination of ionized oxygen vacancy centers therefore decreases the density of F^+–Mg and F^+-centers during electron irradiation. Taken together with changes in the number of electrons residing in aggregate F-centers (like the divacancy center F_2), this accounts for the reduced emission intensity of many spectral features at high currents (Figs. 2 and 3).

For reasons not entirely understood, there is an ultraviolet emission band between 250 and 290 nm that shows anomalous "bleaching" behavior. At 20 mol% Mg concentration the intensity of this band is higher at 30 μA than it is at 10 μA (Fig. 3). At 2.5 mol% Mg concentration the intensity of this band is slightly lower at 30 μA than that at 10 μA. At 0.2 mol% Mg concentration the intensity of this band is once again considerably higher at 30 μA than it is at 10 μA. Hence the capability of generating light in the short wavelength band at high current levels improves as the Mg concentration is increased. At the highest Mg concentrations, spectral features in the range 300–500 nm also appear to be stabilized, although the large F_2 emission peak seen at low current near 520 nm clearly exhibits a strong bleaching effect similar to the reduction of emission seen in Fig. 2 at elevated current levels. The spectrum of the 20% sample does not extend far into the visible and near infrared. A greater proportion of the emission emerges in the ultraviolet and was most intense at the highest doping level synthesized, namely 50%Mg.

4. Conclusions

Optical measurements with over twenty different Mg concentrations have shown that pyrolytic synthesis can produce high densities of point defects in alumina. This unusual finding is a by-product of kinetic synthesis. Mg:Al_2O_3 has good potential for ultraviolet emission in the range 250–290 nm. Emission intensities in this spectral range show systematic variations that reflect changes in the crystal phases of alumina as well as variations in Mg concentration. The stability of ultraviolet emission features in the range 250–290 nm is best in alumina samples with high Mg concentrations (>20%).

While no results have been published as yet on stimulated emission of color centers in alumina nanopowders, preliminary results in our laboratory indicate that just as in Ce-doped samples, random lasing can be achieved with point defects in oxide powders. Hence the combination of an enhanced stimulated emission rate with the natural characteristics of F^+–Mg defect emission may provide superior performance in the future. Ce-doped fluorides (Ce:$LiSrAlF_6$ and CeF_3) and nitride semiconductors may also provide useful sources.

References

[1] R.M. Laine, T. Hinklin, G. Williams, S.C. Rand, J. Metastable Nanocryst. Mater. 8 (2000) 500.
[2] G.R. Williams, B. Bayram, S.C. Rand, T. Hinklin, R.M. Laine, Phys. Rev. A 65 (2001) 013807.
[3] V.V. Semashko, M.A. Dubinskii, R.Y. Abdulsabirov, A.K. Naumov, S.L. Korableva, N.K. Scherbakova, A.E. Klimovitskii, Laser Phys. 5 (1) (1995) 69.
[4] H. Cao, Y.G. Zhao, S.T. Ho, E.W. Seelig, Q.H. Wang, R.P.H. Chang, Phys. Rev. Lett. 82 (1999) 2278.
[5] W.B. Fowler, Physics of Color Centers, Academic Press, New York, 1968.
[6] B. Henderson, R.D. King, Philos. Mag. 13 (1966) 1149.
[7] Y. Chen, M.M. Abraham, Nucl. Instrum. Methods B 59–60 (1991) 1163.
[8] P.A. Kulis, M.J. Springis, I.A. Tale, V.S. Vainer, J.A. Valbis, Phys. Status Solidi. B 104 (1981) 719.